THE UNIVERSITY OF CHICAGO

COMBINING NANOPHOTONIC CAVITY-ARRAYS WITH ATOMIC ARRAYS: SCALING QUANTUM COMPUTERS AND NETWORKS

A DISSERTATION SUBMITTED TO

THE FACULTY OF THE PRITZKER SCHOOL OF MOLECULAR ENGINEERING

IN CANDIDACY FOR THE DEGREE OF

DOCTOR OF PHILOSOPHY

BY

SHANKAR GIRIJAVALLABHAN MENON

CHICAGO, ILLINOIS

JUNE 2025

ABSTRACT

Neutral atom arrays have emerged as one of the leading platforms for quantum computation and simulation. Integrating these arrays with photonic interfaces, such as optical cavities, enables high-speed qubit readout, efficient atom-photon entanglement, and novel quantum simulation capabilities through long-range interactions. However, achieving scalable and efficient integration of atom arrays with photonic structures remains a significant challenge.

In this work, we present an atom-array cavity-array platform that integrates cesium atom arrays with a photonic chip containing over 100 nanophotonic cavities. This platform inherently supports multiplexing by allowing simultaneous interactions between multiple atoms and multiple cavities, a crucial capability for scaling up quantum information processing and networking. To enable this integration, we develop three key techniques: (1) a background-free imaging scheme utilizing excited-state transitions in cesium with fidelity exceeding 99%, (2) a photonic chip design optimized for efficient atom loading, and (3) a free-space coupling scheme achieving over 65% waveguide-to-fiber coupling efficiency.

We demonstrate collisional blockade-limited loading of atom arrays near the photonic chip, parallel transport of atoms to multiple cavities, a key capability that enables the multiplexing required in quantum networks and distributed quantum computing. Finally, we show an array of resonant telecom cavities, and multiple theoretical architectures to make use of these to distribute entanglement across hundreds of kilometers. These results address critical challenges in atom-photon integration and pave the way for scalable quantum information processing.

TABLE OF CONTENTS

LIST OF FIGURES

LIST OF TABLES

ACKNOWLEDGMENTS

This thesis, and the journey it represents, would not have been possible without the support, guidance, and camaraderie of many individuals. I am deeply grateful to everyone who has been a part of this experience. First and foremost, I extend my sincerest gratitude to my advisor, Hannes Bernien. Thank you for being an incredible researcher, mentor, and guide throughout my PhD. Your unwavering passion for science is truly infectious, and your boundless energy to push projects forward has been inspiring. More than anything, thank you for instilling in me a deep passion for this field and for showing what it means to be a dedicated scientist. I also would like to thank Professor David Awschalom and Professor Liang Jiang for their valuable guidance and support over the years, and for serving on the thesis committee

I specifically want to extend my gratitude to Noah Glachman. We spent five years side-by-side in the lab, and your help was crucial in getting the experimental setup built and operational. Your laser skills, coding skills, and puns have been instrumental in its success. Building an experiment inevitably brings countless setbacks alongside the hard-won successes, I appreciate having shared that five-year journey together. As the experiment moves forward, I want to thank the newer members who are taking the reins, Nayana Tiwari and Dahlia Ghoshal. Their energy has been infectious, and the steady stream of memes certainly helped lighten the mood during long days. I truly enjoyed the time spent with Noah, Nayana, and Dahlia in the lab – the mix of intense scientific discussions and random non-science conversations made the environment truly special. I am quite excited and look

forward to the next steps they have planned for the setup.

I was fortunate to overlap for a year with Matteo Pompili, whose programming expertise was nothing short of masterful. He provided a significant boost to our control capabilities at a critical time. I must admit, before Matteo, I had no idea "decorators" were even a programming concept – just one of the many things I learned! My thanks go to Alan Dibos for his help with parts of the early fabrication work and for all the useful scientific discussions we've had over the years. I also want to specifically acknowledge other Red lab members whose work this thesis has directly benefited from. I would like to thank Yuzhou Chai for all the fun conversations about movies, atoms, and the fascinating world of rare earth ions. To Timo Dolne, thank you for countless science talks and all the random banter – I still hope I managed to convince you that atoms are indeed the best things since sliced bread! I am incredibly thankful for Kevin Singh, who was both a mentor and a great friend from my earlier years here. I cherish the memories of the early days spent together in the small lab, talking about everything under the sun. Your discipline and focus were truly amazing and remain something I look up to. I also deeply appreciate Yu-Hao Deng; you are a fantastic researcher, and I genuinely enjoyed our detailed discussions about scientific concepts and intricacies. I'm excited to see what amazing things you are cooking up with atom arrays.

I would also like to thank all the members of the blue and purple labs for creating such a vibrant and supportive environment: Shraddha Anand, Connor Bradley, Ryan White, Vikram Ramesh, Bob Bao, Nikhil Harle, and Jeffrey Yao. You have all been amazing col-

leagues, and the countless conversations, suggestions, and friendly banter have enriched my PhD experience immensely. A special thanks to the amazing undergraduate students I had the privilege of working with: Haley Nguyen, Roberto Cohen, Cody N Googin, and Hongyi Meng. Your enthusiasm and contributions were invaluable, and I learned a great deal from working alongside you. Reflecting on my time here, some of the best moments were the long hours spent in discussion, whether focused on the immediate scientific problem or diving down random intellectual rabbit holes. I have loved and enjoyed every moment of that collaborative exploration and have learned immensely from everyone mentioned here, and indeed the entire group. Thank you all.

Beyond the lab and academics, I was incredibly fortunate to have an amazing set of friends who made this journey so much richer. To Abhirup Guha, Poojya Ravishankar, Kavya Pillai, Anchita Addhya, Vinay Shirhatti, Kruthika Maheshwar, Krithika Mohan, Aritrajit Gupta, Jordan Kemp, and Andrew Pocklington: Thank you for everything. You guys were truly family away from home, and your friendship and support meant the world to me through the ups and downs of grad school. My gratitude also extends to Jonathan Hernandez, Anil Bilgin, Evan Villafranca, Andrew Ye, Jacob Feder, Cyrus Zeledon, Ian Hammock, Elena Glen, Manish Singh, and Leigh Fall. Big thanks for being great friends, for all the fun conversations, and experiences we shared during my time here.

Finally, my deepest gratitude goes to my family. To my parents, Prasanna Vallabhan and Girijavallabhan, thank you for always supporting my decisions and for instilling a scientific

temper in me from the start. You truly are the best parents anyone could ask for. I also want to thank my sister, Kavitha Menon, and brother-in-law, Unnikrishnan Sasikumar, for always having my back and being there for me all through my PhD. Finally, to my fiancé, Devanshi Verma – thank you. You've been my best friend, closest confidant, and my rock these past few years. I truly cherish that.

CITATIONS TO PREVIOUSLY PUBLISHED WORK

Parts of this dissertation cover research reported in the following articles:

Chapters 3, 4, and 5 are based on research published as

"An integrated atom array-nanophotonic chip platform with background-free imaging", S. G. Menon*, N. Glachman*, M. Pompii, A. Dibos, H. Bernien, Nature Communications, 15, 6156 (2024).

Chapter 6 is based on research published as

"Nanophotonic quantum network node with neutral atoms and an integrated telecom interface", S. G. Menon, K. Singh, J. Borregaard, H. Bernien, New Journal of Physics, 22 (7), 073033 (2020).

Chapter 8 includes research reported in the following publications:

"Multiplexed telecommunication-band quantum networking with atom arrays in optical cavities", W. Huie, S. G. Menon, H. Bernien, J. P. Covey, Physical Review Research, 3, 4, 043154 (2021).

"Hybrid quantum repeaters with ensemble-based quantum memories and single-spin photon transducers", F. Gu, S. G. Menon, D. Maier, A. Das, T. Chakraborty, W. Tittel, H. Bernien, J. Borregaard arXiv:2401.12395 (2024).

CHAPTER 1

INTRODUCTION

The ability to precisely control individual qubits is a key requirement for realizing the potential of quantum computing, communication, and simulation. For practical applications, qubits should maintain coherence long enough to allow deep-circuit computations and long-distance entanglement. They must also enable high-fidelity state preparation and measurement, ensuring accurate initialization and readout of quantum information. Furthermore, they should support reliable gate operations with minimal error rates. These qualities are essential for running quantum algorithms that can tackle problems intractable for classical computers, and for exploring complex quantum phenomena such as quantum phase transitions and topological states of matter [1].

The level of control becomes even more critical when scaling up quantum systems to achieve fault-tolerant quantum computation. For a quantum computer to generate results that surpass the capabilities of current classical computers, the individual qubits must retain coherence in the presence of increasing system size and environmental noise. They must also interact in a predictable and tunable way, allowing for the generation of complex entangled states and the implementation of target quantum operations with high precision. This challenge has led to the development of various hardware platforms, each with its unique strengths and challenges, including superconducting circuits leveraging Josephson junctions [2–10], artificial and defect-based qubits in solid state system [11–14], trapped ions confined by electromagnetic fields [15–21], and neutral atom arrays held in optical lattices or tweezers

[22–26]. Among these, neutral atom arrays offer a compelling approach, leveraging optical tweezers and dynamic reconfiguration to enable scalable architectures.

1.1 Atoms arrays

Neutral atom qubits are confined using optical tweezers, which are tightly focused laser beams that create spatially localized trapping potentials. Tweezers exploit the AC Stark shift effect, where atomic levels experience an energy shift proportional to the intensity of the laser light, to trap and confine the atoms [27]. The ability to trap atoms in two-dimensional (2D) [28] and three-dimensional (3D) [29] geometries has been demonstrated. Furthermore, the reconfigurability of optical tweezers enables defect-free array formation by dynamically rearranging atoms [30, 31].

Neutral atom arrays have recently emerged as one of the leading platforms for quantum computing [32, 33], simulation [34, 35], metrology [36, 37], and networking experiments [38, 39]. The technology leverages fundamental atomic physics, including the identical nature of atoms, long coherence times of atomic states, and optical control to create a scalable and highly coherent qubit architecture. Recent advancements have demonstrated the ability to trap and manipulate thousands of neutral atoms in optical tweezers, with the state-of-the-art system reaching over 6,000 qubits in a single experiment [40]. The combination of scalability, flexible reconfigurability, and fast Rydberg-based interactions makes neutral atom arrays a leading candidate for large-scale quantum technologies.

For qubit manipulations, hyperfine states of alkali atoms (rubidium-87, cesium-133) [33, 41], and nuclear [42] and clock spin states of alkaline-earth like atoms (strontium-

87, ytterbium-171) [43–46] are commonly used. These qubits have routinely demonstrated long coherence times on the order of seconds. Further, the nuclear spin qubits are highly resilient to magnetic field fluctuations and can serve as robust memory qubits [43, 44]. Single qubit gates for atoms are implemented through resonant microwave or Raman transitions between hyperfine states [47]. Entangling and gate operations are enabled through highly excited Rydberg states, where atoms exhibit strong dipolar and Van der Waals interactions [48]. These Rydberg-mediated interactions have been used to achieve controlled-Z (CZ) and controlled-X (CX) gates with fidelities exceeding 99.5% [49–51]. Rydberg interaction beyond the Rydberg blockade regime has also been demonstrated using ultrafast pulses [52]. Dual-species arrays (Rb-Cs) further enable tunable interaction regimes, including resonant dipole-dipole coupling, via interspecies Förster resonances [53]. The ability to address individual atoms with spatially resolved laser beams further enhances the control capabilities of these systems [33, 54].

Readout of neutral atom qubits is typically performed via fluorescence imaging, where state-dependent scattering of light allows for high-fidelity state discrimination. Mid-circuit readout and feedback based on a second species [55], shelving [56, 57], rearrangement [41], and through cavities [58] has been shown. These capabilities are important for quantum error correction, as they allow for real-time feedback and syndrome extraction without collapsing the full quantum state [59, 60].

A major advantage of neutral atom arrays is their scalability, with current platforms supporting hundreds to thousands of qubits in a compact footprint [40]. The ability to trap atoms in programmable geometries, dynamically rearrange them, and implement any-to-

any connectivity via tweezer transport or Rydberg interactions makes these systems highly adaptable [32]. Unlike fixed hardware platforms such as superconducting circuits, neutral atom arrays can be reconfigured on demand to optimize performance for different quantum algorithms or error correction schemes. Additionally, the combination of long-lived qubit states and strong, tunable interactions makes neutral atom arrays an attractive system for quantum information processing.

With these capabilities, neutral atom systems also offer unique opportunities for quantum networking. The integration of atoms with optical cavities enhances light-matter interactions, enabling efficient photon-mediated entanglement generation. New protocols, compatible atoms, and frequency conversion techniques further allow for compatibility with telecom wavelengths, facilitating long-distance quantum communication. These features position neutral atom arrays not only as a contender for quantum computing but also as a key player in distributed quantum networks.

1.2 Quantum networks

Unlike classical networks that transmit bits, quantum networks rely on the transmission and entanglement of qubits. Sharing quantum information across distances unlocks various applications in computation, networking & security, and sensing. Specifically, it enables distributed quantum and classical computing [61–65], secure and blind computation [66–69], and quantum fingerprinting [70]. In the realm of networking and security, quantum information sharing facilitates secure communication [71–75], anonymous key agreement [76], Byzantine fault tolerance [77–79], and secure electronic voting [80, 81]. Further, quantum networks

can facilitate quantum-enhanced sensing capabilities such as long baseline telescopes [82], clock networks [83], and spacetime curvature measurements using quantum systems [84, 85]. Finally, quantum networks also offer an advantage and speedup over classical protocols in specific games [86, 87], communication scenarios [88], and in high-frequency trading [89].

A fundamental challenge in building large-scale quantum networks is the loss of quantum information over long distances due to photon absorption and decoherence. Current optical fibers suffer from wavelength-dependent attenuation. This loss is minimized for telecom wavelengths ranging from $\sim$1260 nm - $\sim$1625 nm due to fundamental limitations. At shorter wavelengths outside this window, the losses are limited by Rayleigh scattering, and at higher wavelengths, photon energy is close to the vibrational energy levels, leading to absorptive losses. While satellite-based architectures overcome the fiber photon loss challenges, atmospheric photon losses currently limit the windows of operation [90, 91]. The photon loss problem is further exacerbated by the low entanglement generation rate currently possible across different platforms. Unlike classical signals that can be amplified, quantum states cannot be directly copied due to the no-cloning theorem. However, this photon loss challenge can be mitigated with quantum repeaters [92, 93]. Repeaters extend entanglement distribution via entanglement swapping and enable quantum correlations over thousands of kilometers.

Recent advances in quantum networks have demonstrated critical milestones toward scalable quantum communication. A three-node quantum network, and teleportation of states within it have been demonstrated in nitrogen-vacancy (NV) centers [94, 95]. The experiment achieved entanglement swapping and storage across distances, demonstrating the fundamen-

tal building blocks for a quantum repeater. Metropolitan-scale entanglement distributions also have been demonstrated in atomic ensembles [96], silicon-vacancy (SiV) centers [97], and NV centers [98]. At the individual node level, there have been experiments on increasing the number of qubits on the nodes [99–102]. Logical qubit-photon entanglement using multiple qubits has also been demonstrated in NV centers [103].

Another exciting avenue of progress is hybrid quantum systems, where different quantum systems are interfaced with each other. In future quantum networks, the advantages of individual quantum systems can be brought together to enhance the network capabilities [104]. Towards this, atomic systems have been coupled to multimode solid-state memory [105] and trapped ions [106]. Ions have also been coupled to molecules [107], and quantum dots [108]. There are also proposals to couple rare earth ensemble memories with trapped ions [109], and atomic ensembles [110], and also to couple atomic ensembles with superconducting qubits [111].

On the application side, distributed quantum computing has been demonstrated in trapped ion systems [112]. Blind quantum computation has been demonstrated in trapped ions [113], and SiV centers [114]. Quantum advantage has been demonstrated in the Odd-Cycle game [115]. Demonstration of enhanced sensitivity from entangled network nodes has been demonstrated in an atomic system [116, 117].

The primary challenges faced by current quantum networks are the low entanglement rate and short quantum memory coherence times, which limit the scalability. Entanglement distribution rates are often constrained by photon loss in optical fibers, inefficient quantum sources, and the probabilistic nature of entanglement swapping. Additionally, quantum

memories, which are crucial for storing and synchronizing entangled states across a network, currently suffer from coherence times that are too short to maintain high-fidelity entanglement over distances. Together, these factors create a bottleneck, preventing quantum networks from operating at practical speeds for large-scale applications.

One promising strategy to overcome low entanglement rates is multiplexing, which enables simultaneous entanglement attempts across multiple frequencies [102, 118, 119], spatial [120, 121], or temporal modes [39, 122]. Current approaches often require two-way communication between nodes to confirm successful entanglement, leading to significant time delays, especially in long-distance networks [93]. These delays reduce the overall entanglement distribution rate and make real-time quantum communication impractical. Multiplexing addresses this issue by allowing multiple entanglement generation attempts in parallel, increasing the probability of success and dramatically improving network throughput. Implementing efficient multiplexing schemes will be necessary for scaling quantum networks to practical levels.

As noted earlier, fiber loss presents another major challenge for quantum networks, as most qubit platforms operate at wavelengths that experience significant attenuation in standard telecom fibers. To mitigate this, quantum frequency conversion techniques can shift qubit emission to telecom wavelengths where fiber losses are much lower [105]. However, this conversion process is noisy, introducing a trade-off between conversion efficiency and added noise that can degrade entanglement fidelity [96, 105, 123–125]. An alternative approach is to develop qubits that naturally operate at telecom wavelengths, eliminating the need for conversion [126–128]. Both methods are active fields of development, and achieving efficient

telecom compatibility is essential for long-distance quantum communication over existing fiber infrastructure. However, there are alternative ideas of combining vacuum beam lines along with the fiber infrastructure, which might reduce the telecom operation requirements [129].

For quantum networks to function reliably at scale, quantum processing capabilities have to be incorporated for the purpose of entanglement purification [121] and deterministic swapping [95]. Without these processes, entanglement fidelity and rates deteriorate over long distances due to accumulated errors and photon loss. Entanglement purification allows noisy entangled states to be refined into higher-fidelity ones, while deterministic swapping enables long-range entanglement without relying on probabilistic measurements. Implementing these capabilities requires processing capability at network nodes, capable of real-time error correction and adaptive operations. Developing such quantum processing nodes will be essential for building a fault-tolerant and scalable quantum internet.

Another important requirement for high efficiency quantum networks is the efficient extraction of entangled photons. In general, emission from emitters are isotropic and its collection is inefficient. Optical cavities can overcome this by enhancing the emission into the cavity photonic mode [130]. However, integrating cavities into practical qubit architectures poses significant engineering challenges in many platforms. Recently, cavities have been integrated with atom arrays [39] and trapped ion arrays [122], showing that large-scale emitter cavity systems are possible. Overcoming the cavity integration challenge without sacrificing scalability and computational capability is a necessity for scalable quantum networks.

To illustrate fundamental requirements for a practical quantum network, we calculate entanglement distribution rates for a specific scenario, depicted in Fig. 1.1. This scenario involves distributing entangled qubits between Chicago (USA) and Thrissur (India) over a $14,000\,\text{km}$ optical fiber link. We assume a maximum qubit-photon entanglement generation rate of $1\,\text{GHz}$ per source and utilize a two-way communication protocol [93]. We analyze four distinct cases:

1. **Case 1 (Baseline):** With only a single qubit at each endpoint, the achievable rate is severely limited. The long wait time imposed by photon propagation and subsequent classical signaling inherent in the two-way protocol [93] reduces the effective rate far below the $1\,\text{GHz}$ system capability, resulting in a negligible rate ($< 10^{-300}\,\text{s}^{-1}$), which is omitted from the graph.

2. **Case 2 (Repeaters):** Introducing 100 quantum repeaters between the locations significantly mitigates photon loss. Assuming a realistic propagation loss of $4.5\,\text{dB/km}$ (common in current qubit systems [131–133]), repeaters improve the rate compared to Case 1 by effectively shortening the transmission segments.

3. **Case 3 (Low Loss):** Building on Case 2, we consider operating at telecom wavelengths, reducing the fiber loss dramatically to $0.2\,\text{dB/km}$. This enhancement further boosts the achievable entanglement rate to $0.6\,\text{Hz}$.

4. **Case 4 (Multiplexing):** Finally, we incorporate multiplexing by employing ten thousand additional qubits alongside the setup of Case 3. This high degree of parallelism effectively offsets the protocol's wait time, yielding a significantly higher entanglement

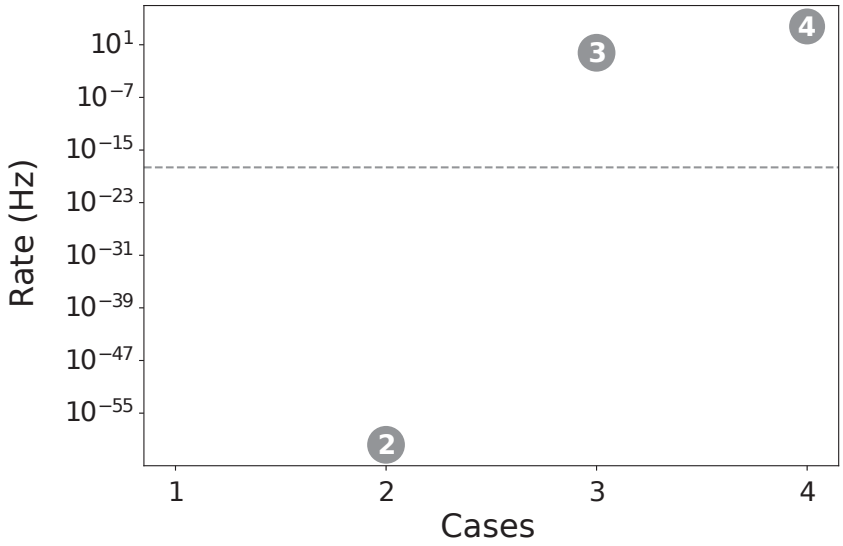

Figure 1.1: Comparison of entanglement generation rates over a 14,000 km link between Chicago and Kerala. Four scenarios are shown: Case 1 uses a single qubit pair (with NIR photons), yielding a rate too low to be displayed ($< 10^{-300}\,\mathrm{s}^{-1}$). Case 2 introduces 100 quantum repeaters. Case 3 assumes the Case 2 repeater setup but operates at lower-loss telecom wavelengths. Case 4 enhances Case 3 by incorporating multiplexing with 10,000 additional qubits per node. The dashed line represents the minimum rate required to enable an event within the universe's age.

rate of 6 kHz.

For perspective, the dashed line in Fig. 1.1 represents the minimum rate required to enable an event within the current age of the universe. This comparison highlights that achieving practical intercontinental quantum communication necessitates the combined advancements of quantum repeaters, telecom transmission, and multiplexing.

In summary, a practical quantum network would require 1) multiplexing capability, 2) telecom operation, 3) processing capability, and 4) efficient photon extraction through cavities. While these capabilities are yet to be combined in a single system, there is active work on this across different platforms, including the work described in this thesis.

1.3 Cavity-mediated atom-photon interactions

Coupling atoms to cavities is one of the key ways that increase the photon collection efficiency from atoms. For a two-level system coupled to the cavity, the coherent interaction is given by the Jaynes-Cummings Hamiltonian:

$$\hat{H}_0 = \hbar\omega_c a^\dagger a + \hbar\omega_a \sigma_z + \hbar g(a^\dagger \sigma_- + a\sigma_+). \tag{1.1}$$

where ω_c (ω_a) is the resonance frequency of the cavity (atom) and $a^\dagger$ (σ_+) is the excitation operator for the cavity (atom). Here g is the single photon Rabi frequency [130]:

$$g = \frac{\hat{\mu}\cdot\hat{E}}{\hbar} = \sqrt{\frac{\mu^2\omega_c}{2\hbar\epsilon_0 V}}, \tag{1.2}$$

where $\hat{\mu}$ is the atomic dipole moment, $\hat{E}$ is the vacuum field strength, ϵ_0 is the vacuum permittivity, and V is the mode volume of the cavity. The system is then further characterized by the incoherent losses given by atomic decay (γ) and the cavity photon decay (κ). In the presence of these losses, the atom's state evolution is given by the master equation:

$$\dot{\rho} = -\frac{i}{\hbar}[\hat{H}_0, \rho] + \frac{\gamma}{2}(2\hat{\sigma}^-\rho\hat{\sigma}^+ - \hat{\sigma}^+\hat{\sigma}^-\rho - \rho\hat{\sigma}^+\hat{\sigma}^-) + \frac{\kappa}{2}(2\hat{a}\rho\hat{a}^\dagger - \hat{a}^\dagger\hat{a}\rho - \rho\hat{a}^\dagger\hat{a}), \tag{1.3}$$

where $\dot{\rho}$ represents the time derivative of the density operator ρ that characterizes the combined atom and cavity state. The relative strength of coherent coupling to dissipative processes is characterized by cooperativity (C), given by

$$C = \frac{g^2}{\kappa\gamma} \tag{1.4}$$

For a conventional Fabry-Perot cavity, more intuition can be built on cooperativity. As noted previously [134, 135], C can be rewritten as $C \propto \frac{2\lambda^2}{\pi}\frac{F}{\omega_o^2}$, where F is the cavity finesse and ω_o is the waist of the cavity mode. This implies that the rate of coherent dynamics to incoherent dynamics is geometrical, and also independent of the separation between the cavity mirrors. Interestingly, this opens up the possibility of long cavities with mirrors outside the vacuum chamber.

The different cavity coupling regimes can be classified based on the relation between the coherent atom-cavity coupling strength and the incoherent losses κ and γ. [136] (Note: In reference [136], derivations assume that the atoms do not decay, here I modify the definitions to include it.)

- Strong coupling regime: $2g > \kappa + \gamma$

  An alternate commonly specified requirement for strong coupling is $C \gg 1$. In both cases, the coherent dynamics are stronger than any incoherent dynamics in the system. However, the definition here is based on the damped oscillation of atom-photon states, which is possible as long as $2g > \kappa$, and $2g > \gamma$. In this case, the cavity-mediated Rabi oscillation frequency 2g is fast compared to the photon decay from the cavity or the atomic decay from the excited state. This makes it possible for atoms in the excited state to emit a photon into the cavity, and get re-excited with the same emitted photon before the photon decays from the cavity, or the atom decays from the excited state

[136]. Given this case, it is also natural to define C = $\frac{(2g)^2}{\kappa\gamma} = \frac{4g^2}{\kappa\gamma}$. However, note that C>1 does not imply strong coupling in both cases as $\frac{4g^2}{\kappa\gamma}$ can be greater than 1 given g$\gg \gamma$.

In this regime, the coherent exchange of excitations between an atom and the cavity mode dominates over dissipation. This results in energy exchange between the atom cavity states at a rate faster than the rate at which it leaks out of the system. A key signature of this regime is Vacuum Rabi Splitting, where the system's spectrum exhibits two distinct peaks separated by 2g, indicating the strong atom-cavity interaction.

Strong coupling enables several important applications. Cavity-based readout allows for high-fidelity quantum non-demolition (QND) measurements, where the vacuum Rabi splitting modifies the transmission and reflection properties. An example of this is shown in Fig. 1.2 a), where the cavity does not transmit at its resonance frequency when coupled to an atom. Strong coupling also allows ascertaining the center of mass motion of atoms in the cavity field [137]. Additionally, this regime allows dark state-mediated protocols, allowing high-fidelity gates [138]. Furthermore, strong coupling also facilitates deterministic entanglement generation between atoms through the shared cavity mode [139].

- Purcell regime $\kappa > 2g > \gamma$

  The Purcell regime, also referred to as the bad cavity regime, occurs when the cavity decay rate κ is the dominant rate, typically exceeding both the coherent coupling strength ($\kappa > 2g$ or $\kappa \gg g$) and often the free-space atomic decay rate ($\kappa \gg \gamma$). In

this scenario, the interaction between the atom and the cavity mode is overdamped and not strong enough to sustain coherent Rabi oscillations [136]. Any excitation emitted by the atom into the cavity mode tends to decay irreversibly out of the cavity via photon loss much faster than it can be reabsorbed by the atom. The figure of merit here is not the coherent coupling itself, but rather the enhancement of spontaneous emission into the cavity mode. Even in this scenario, C$\gg$1 is possible based on the ratio of $\frac{2g}{\gamma}$. The key parameter quantifying the effect is the Purcell factor. When an atom is coupled to a cavity, and $\kappa >$ g, the atomic decay into the cavity decay is given by [140]:

$$\gamma_c = \frac{4g^2}{\kappa} \tag{1.5}$$

$$\gamma_c = \frac{2\hat{\mu}^2 Q}{\varepsilon_0 \hbar V}, \tag{1.6}$$

$$\gamma_c = \eta\gamma, \tag{1.7}$$

Here Q is the cavity quality-factor given by ω_c/κ, the spontaneous decay rate $\gamma = \frac{\mu^2\omega_a^2}{3\pi\epsilon_0\hbar c^2}$, and η is the Purcell factor, and is given by

$$\eta = \frac{3}{4\pi^2}\frac{Q\lambda_c^3}{V}. \tag{1.8}$$

The Purcell factor is related to cooperativity by $\eta = 4C = 4g^2/(\kappa\gamma)$, representing the enhancement factor of the emission rate into the cavity mode compared to the

free-space rate γ.

This enhanced emission occurs because the cavity modifies the local density of electromagnetic states available to the emitter at its transition frequency. Compared to the uniform density of modes in free space, the cavity provides a significantly higher density of states concentrated around its resonance (proportional to Q/V), thus funneling the emission preferentially into this single mode. Unlike the spectral splitting seen in strong coupling, the main observable is the modified decay dynamics and the highly directional emission into the cavity output. This makes the Purcell regime ideal for experiments that involve the collection of photons from emitters, entanglement distribution, or readout-based experiments.

The enhancement of spontaneous emission is particularly exciting for applications that involve outcoupling of the emitted photon. The overdamped condition of the Purcell regime implies that a photon emitted by the atom into the cavity mode will decay from the cavity before it can be reabsorbed, thereby avoiding potential decoherence from re-absorption. Purcell enhancement is critical for reducing the threshold power needed for lasing, especially in micro- and nanolasers [141], and can be used to increase the transition rates of otherwise weak or slow emitters, making them more accessible for experiments or applications [142].

The difference between the strong coupling regime and the Purcell regime can also be seen in the cavity reflection/transmission spectra. If a cavity is probed with an external laser, the modified Hamiltonian $\hat{H}_0$ in the interaction picture of the problem laser is given

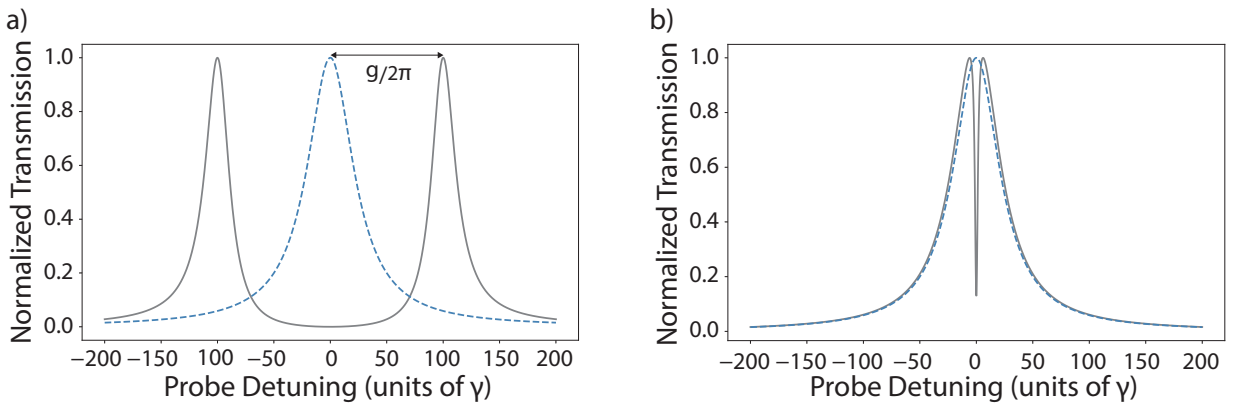

Figure 1.2: a) A cavity transmission (dashed blue line) modified by the presence of a strongly coupled atom. The cavity spectrum is split into two peaks separated by $2g/2\pi$. Here g= 100γ, $\kappa = 50\gamma$. b) A cavity transmission (dashed blue line) modified by the presence of an atom in the Purcell regime. Here g= 5γ, $\kappa = 50\gamma$.

by:

$$\hat{H}_0 = \hbar\Delta_{cp}\hat{a}^\dagger\hat{a} + \hbar\Delta_{ap}\hat{\sigma}_+\hat{\sigma}_- + \hbar g[\hat{a}\hat{\sigma}_+ + \hat{a}^\dagger\hat{\sigma}_-] + \hbar\epsilon(\hat{a} + \hat{a}^\dagger). \tag{1.9}$$

The driving or the probing field amplitude is ϵ, and ω_p is the probe laser frequency. The detuning between the cavity resonance and the probe field is $\Delta_{cp} = \omega_c - \omega_p$, and the detuning between the atomic resonance and the probe field is $\Delta_{ap} = \omega_a - \omega_p$. An analytical solution to the above equation can be derived under a weak probe [143] or using input-output theory [144–146]. Fig. 1.2 a) shows an atom strongly coupled to the cavity with g=2κ, satisfying the strong coupling condition. However, when g<κ (Fig. 1.2 b), the cavity spectrum remains more or less the same with a modified transmission feature close to the resonance.

As shown above, when an atom is coupled to a cavity, the emission into the cavity is given by γ_c. Then the ratio of photons emitted into the cavity compared to that emitted into the vacuum is given by

$$\frac{\gamma_c}{\gamma_c + \gamma} = \frac{4C\gamma}{4C\gamma + \gamma} = \frac{4C}{4C + 1} \tag{1.10}$$

Note that for a cooperativity definition of $C = \frac{4g^2}{\kappa\gamma}$, this would be $\frac{C}{C+1}$ instead. For large values of C, it can be easily seen that close to 100% photon emission can be collected into the cavity. This makes large cooperativity a highly desirable capability for future quantum network operations. However, photons emitted into the cavity can be lost to vacuum through scattering (κ_{sc}) or can be out-coupled through the cavity mirrors (κ_{wg}). Finally, the emitted photon has to be coupled into a fiber through mode matching (F_{ce}). This gives:

Probability of collecting photon in the fiber = probability of emitting into the cavity mode × out-coupling from the cavity × coupling into the fiber mode.

$$P_{fiber} = \frac{4C}{4C + 1} * \frac{\kappa_{wg}}{\kappa_{wg} + \kappa_{sc}} * F_{ce} \tag{1.11}$$

For experiments involving photon collection, this overall probability of collecting an emitted photon into the fiber has to be maximized.

1.4 Different atom-cavity platforms

Many pioneering cavity QED experiments have been performed in the last few decades. The first vacuum Rabi splitting was observed in 1992 in Fabry-Perot cavities [143]. Since then, many experiments have utilized atoms coupled to cavities and waveguides, including using different cavity architectures.

1.4.1 Macroscopic Fabry-Perot Cavities

Macroscopic Fabry-Perot cavities consist of two highly reflective mirrors separated by millimeter to centimeter-scale distances. These cavity systems are known for their exceptionally high quality factors (Q) and long photon storage times, resulting in minimal cavity decay rates (κ). Although these cavities offer high finesse and strong light confinement, their relatively large mode volumes (V) limit the coupling strength, as g scales inversely with $\sqrt{V}$. Typical mirror-based Fabry-Perot cavities have g on the order of MHz, and κ on the order of 100's of KHz to a few MHz, making both g and κ comparable to the atomic decay rate for atoms like rubidium (Rb), and cesium (Cs).

These cavities played a crucial role in the early demonstrations of cavity quantum electrodynamics (QED), enabling fundamental studies of strong coupling [143]. Single atoms trapped in Fabry-Perot cavities have been used to entangle atoms across a network [132], to perform cavity-mediated atom-atom entanglement [147], and to perform atom-photon gates [148]. Arrays of atoms have been coupled to Fabry-Perot cavities to demonstrate mid-circuit measurements [58], super and sub-radiance [149, 150], defect-free loading with strong coupling [151], and error detection [152].

1.4.2 Fiber Fabry-Perot Cavities

Fiber-based Fabry-Perot (FFP) cavities employ microscopic mirrors fabricated directly onto the end facets of optical fibers with cavity lengths ranging from micrometers to millimeters. Compared to macroscopic cavities, FFPs significantly reduce mode volume while maintaining high finesse, leading to enhanced coupling strengths g for ground-state atoms [153]. Typical

g values for these cavities are in 30-100 MHz, with κ in tens of MHz [139, 154].

FFPs have been used for coupling a single atom to two different cavities [155], deterministic entanglement of two atoms [139], Purcell enhanced emission [156] along with state preparation [157], and photonic bell state generation based on inelastic scattering [158].

1.4.3 Nanophotonic devices

Nanophotonic cavities encompass a range of solid-state structures, including photonic crystal defect cavities, microring resonators, microtoroids, and evanescently coupled systems such as tapered nanofibers. These platforms feature extremely small mode volumes, often approaching the cubic wavelength scale, leading to significantly enhanced coupling strengths g [159]. Even moderate Q-factors can enable strong coupling or Purcell-enhanced emission [160].

A key advantage of nanophotonic cavities is their potential for chip-scale integration, making them promising candidates for experiments that involve scaling. However, precise atomic positioning near surfaces is a challenge, and surface interactions can introduce decoherence and atom loss [161]. Despite these challenges, individual atoms have been successfully integrated with nanophotonic platforms such as cavities [162], waveguides [163], and nanofibers [164–166]. For nanophotonic cavities, the cavity coupling is of the order 800 MHz, and κ is of the order of a few GHz [167].

Single atoms have been deterministically coupled to nanophotonic cavities with cooperativities of 70 [162, 167]. Two atoms have also been coupled to a single nanophotonic cavity

mode and entangled using probabilistic schemes [168]. Collective emission and superradiance have also been demonstrated by coupling atoms to photonic waveguides [169, 170] and cavities [171]. Apart from the scalability, nanophotonic devices also offer a wide range of long-range interaction Hamiltonians that can enhance the atom-based simulation [172–183] and photon emission capabilities [184–186].

1.5 Approach in this thesis

In this work, we want to combine the capabilities of atom arrays with those of cavities. In particular, we want a processing-capable atom array next to cavities that could be used for atomic state readout and atom-photon entanglement generation. In addition, to maximize the potential for future quantum applications, a desirable capability is to have an array of cavities to which atoms can deterministically couple, as shown in Fig. 1.3. This enables a system that possesses both temporal and spatial multiplexing. For the purpose of photon collection from the cavity, the system should ideally operate in the Purcell regime.

While macroscopic Fabry-Perot cavities have been successfully integrated with atom arrays, their cavity coupling strength g is on the lower end, and scalability in the number of cavities is very limited. Fiber Fabry-Perot cavities are an exciting platform as they can work in both Purcell as well as strong coupling regimes. However, the small modes of the FFPs come with the additional overhead of fiber mounts and piezo actuators close to the atom trap region. Further, they require precise assembly and alignment of individual fiber components, making an array of such cavities a challenge.

In contrast, nanophotonic cavities can be fabricated in large numbers and directly onto

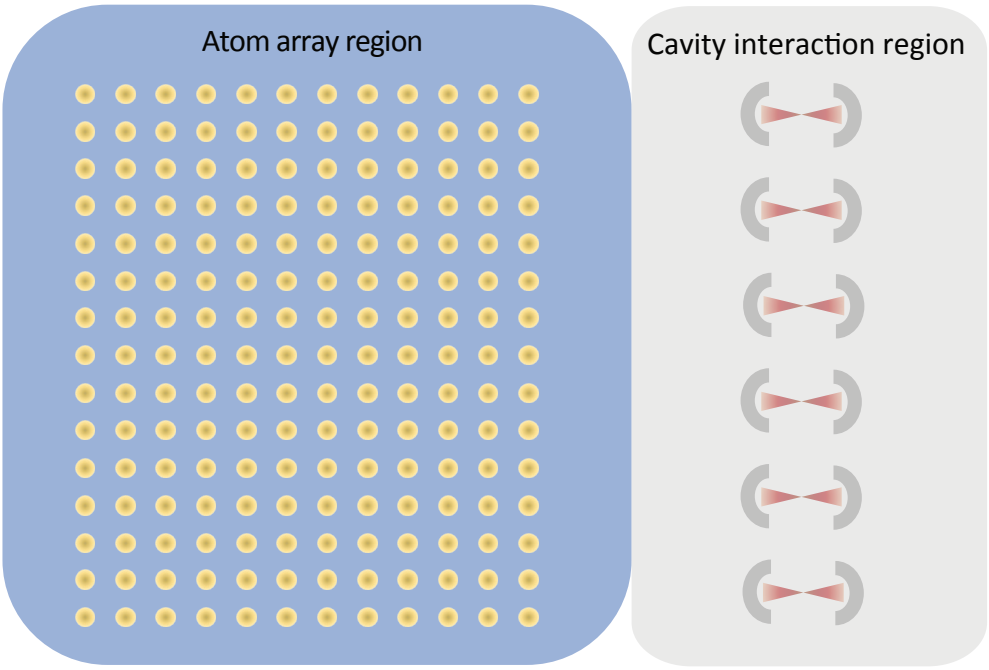

Figure 1.3: Illustration of a setup with a region for atom array operations. A second region for cavity-based interaction is close to the atom array region and can be accessed by reconfigurable tweezers.

chips using established semiconductor manufacturing techniques. This process enables a level of scalability not possible in other cavity systems, allowing for the reproducible creation of large numbers of identical, densely packed cavities on a single photonic chip. Additionally, since the chips are a standalone structure, they can be supported by mounts millimeters to centimeters away from atom-trap region. Furthermore, nanophotonic cavities offer the smallest mode volumes (V), leading to large Purcell enhancements.

Another key capability of a photonic chip is its versatility. It has the ability to host an array of cavities that could be resonant with multiple species, or more than one transition of the same atoms. Furthermore, photonic chips also allow for the co-existence of cavities and waveguides operating at different coupling regimes. Cavities designed for atom-atom entanglement, cavities designed for atom-photon entanglement, or waveguides for long-range

Hamiltonian mediated simulations can all be combined into one chip. This makes photonic chips an ideal platform for the scalable integration of atom arrays and cavities.

However, incorporating scalable photonic interfaces and atom array capabilities is a challenging task. The presence of a dielectric structure can significantly impact the process of loading atoms into traps. While atoms have been cooled and loaded directly into traps in the vicinity of a single nanophotonic cavity [162] or waveguide [164, 169, 187–190], the viability of directly loading traps near a chip-scale structure has been undermined by unbalanced scattering and reflections from the dielectric surface. Techniques such as loading from an atomic fountain [191, 192] or a cascaded magneto-optical trap (MOT) [163] have been implemented to overcome this challenge near larger dielectric structures. Additionally, methods such as stage-based transport of a tweezer array, an optical conveyor belt, and an optical funnel formed through a transparent dielectric structure have been employed to increase the trap filling fraction near chip-scale structures [193–197].

Additionally, fluorescence imaging of atoms in the vicinity and on top of nanophotonic devices presents another key challenge due to scattering of the imaging beams from the device. Transmission and reflection measurements have been explored to estimate the number of atoms coupled to a device [163, 164, 169, 187–192], enabling fast readout. However, these methods only provide global system information rather than site-resolved atomic state information. To achieve the site-resolved single-shot readout necessary for quantum information processing and networking, methods such as confocal microscopy [167], exciting atoms through propagating waveguide modes [198], and polarization filtering combined with spatial filtering [196] have been implemented. However, these techniques have been limited to

either a few atoms, single devices, or specific device geometries. Demonstrating atom array techniques such as rearrangement and single-shot readout of large atom arrays near arbitrary nanophotonic devices remains an outstanding challenge.

Through the work presented in this thesis, we overcome some of these challenges to integrate atom arrays with resonant cavity arrays. First, we introduce an experimental platform combining an atom array with a silicon nitride on silicon chip hosting around 150 nanophotonic devices, along with a background-free imaging scheme to overcome scattering from the nearby chip. A semi-open chip geometry, where devices are suspended from the edge of the chip, provides sufficient laser cooling access to enable MOT formation near the chip structure. A free-space atom array can be loaded in the open space to the side of the chip. We find that the presence of the chip has minimal effect on the atom loading characteristics into the tweezers with loading probabilities and temperatures similar to conventional atom array experiments [31]. Furthermore, light can be coupled in or out of the nanophotonic devices via efficient free-space coupling, enabling fiber-free photon coupling to any devices inside the chamber [193, 199].

A multichromatic imaging technique [200–203] suppresses the device scattering, enabling single-shot readout of the entire atom array close to, or even on top of, the devices using an electron-multiplying charge-coupled device (EMCCD) camera similar to the standard read-out method for free-space atom arrays. Combining the above capabilities, we demonstrate that we can rearrange atoms and load them onto multiple devices at the same time or to a single device, where they can be imaged in a single shot with our imaging technique.

We then make use of this platform to combine atom arrays with cavity arrays that are

resonant with the telecom transitions present from the excited state of cesium atoms. We discuss our experimental progress in attaining telecom single photon sources on this platform. We also present a theoretical scheme for generating atom-telecom-photon entanglement, making use of the cavities presented above. Finally, we discuss a few approaches on scaling quantum networks with atoms coupled to cavities.

The techniques and methods presented here represent a general recipe for integrating arrays of atoms with a wide range of nanophotonic structures, including alligator waveguides [163], corrugated cavities [204], or a more complex combination of 1D cavities [104]. The key ingredients here are the semi-open chip geometry, multichromatic fluorescence imaging, and a method of coupling light in and out of the nanophotonics. This platform combines the measurement and rearrangement capabilities of atom arrays with the ability to engineer the photonic environment via integrated cavities and waveguides. This represents an enabling step towards multiplexed telecom quantum networking with resonant cavities [205, 206], fault-tolerant distributed quantum computing with Rydberg integration [207], and demonstrations of novel many-body phenomena in atom-waveguide systems including self-organization of atoms and the generation of arbitrary photonic states [172, 208].

CHAPTER 2

EXPERIMENTAL SETUP

2.1 Introduction

In the last decade, many pioneering quantum computation and simulation experiments have been carried out on atom array platforms. There have been experiments taking advantage of the rearrangement capabilities of the atom [32, 33, 41], high-fidelity gates through Rydberg interactions [50, 51, 54], and the scalability to a large number of qubits [40].

The above capabilities of trapping, rearrangement, scaling, and gates in atom-arrays are achieved in a fundamentally different manner as compared to other platforms, including trapped ions, a similar cold-atom platform. While atoms and ions are both laser-cooled, their trapping mechanisms are fundamentally different as ions are trapped using DC/RF electric and magnetic fields, while neutral atoms are trapped using individual focused laser beams. In addition, interactions between ions are done using the phononic modes of the trapping potential, allowing potentially arbitrary connectivity [15, 209–211]. In contrast, neutral atom gates are predominantly carried out through Rydberg interactions [24, 212–215]. In neutral atom-array based experiments, atoms are trapped in separate harmonic oscillators, making any phononic gates challenging. Similarly, Rydberg-based experiments have been proposed in ionic systems [216]; however, they are particularly challenging due to the sensitivity of Rydberg gates to charges.

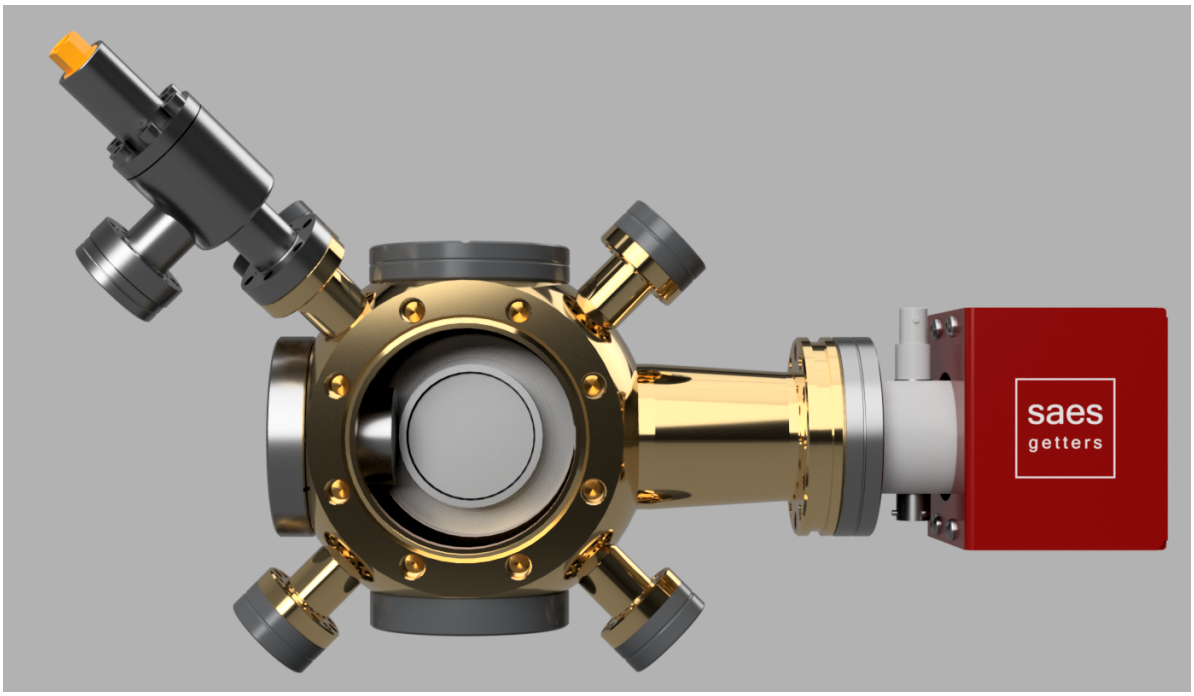

Figure 2.1: Rendering of the chamber design modeled in Fusion 360. One of the 4.5 CF conflat is removed to see the insides of the chamber. The coupling re-entrant on the left and the tweezer re-entrant (coming out of the plane) can be seen inside.

In our experiment, we want to combine an array of atoms with a photonic chip that is millimeters in dimension. Our setup has similarities with trapped ion systems by having large structures near atom traps. This results in charge accumulation on dielectrics, causing potential Rydberg integration and optical access challenges. Further, while we do not have RF or magnetic trapping mechanisms inside our chamber, atoms can be trapped on an optical potential generated through photonic devices [163], and can have gates mediated by spin motion coupling [174]. In this chapter, we will discuss our experimental setup and how we incorporate the capabilities required for atom array - photonic chip along with their integration.

2.2 Chamber

One of the key differences between the early AMO experiments and current generations of atom-array experiments is the common use of compact glass cells as opposed to bulky metallic chambers. This change allows for enhanced optical access while maintaining a small overall volume. In addition, it also facilitates large scaling of the number of atoms in the array, while maintaining all the control capabilities. However, the integration of photonic chips within such compact glass cell environments presents notable challenges. Normally, glass cells themselves do not have any internal mounting capabilities. This necessitates either modifying the glass cell itself or having long levers protruding into the glass cell from a nearby metallic chamber that can be used for chip mounting. This resulted in the early photonic chip experiments relying on large metallic chambers. However, in the last decade, experiments have been carried out using photonic devices in glass cells. In one approach an extended lever was established for device mounting in the glass cell [217], while in another experiment, a chip mount was glass-bonded onto the glass cell [218].

In our experiment, we want large atom arrays, which necessitate compactness. While a glass cell is desirable for its compactness and optical access, we decided to go with a metallic chamber. Our approach was to make the smallest possible stainless steel chamber that can house a photonic chip, while maintaining a reasonable optical access. The main chamber part is a custom Kimball semi-rectangular box with 4.5-inch conflats (4.5" CF) on two opposite sides and 2.75" conflats on all other sides as shown in Fig. 2.1. The chamber is made

out of 316 L stainless steel to avoid magnetic effects and to reduce eddy currents. One of the 2.75" CF is modified to a tube to accommodate a combination ion-getter pump (NextTorr Z200) sticking directly into the science region. This design already limits the overall volume of the chamber. Further, we use two custom re-entrants on the 4.5-inch conflats for high NA imaging (MPF viewports). The re-entrants are designed to have the largest diameter inside the chamber while maintaining enough space for a groove grabber to attach to the chamber. Another re-entrant conflat is added on the opposite side of the pump tube for coupling light into the photonic devices. Overall, this design allows 0.7 NA objectives for imaging the atoms inside the chamber along with a 0.4 NA objective for coupling light in and out of the photonic devices. Five protruding 1.33" conflats are added to the chamber for the magneto-optical-trap (MOT) and to connect to the roughing pump.

The re-entrant glass was specifically made to be 3.5 millimeters thick, to be compatible with the commercially available glass corrected objective (Mitutoyo G Plan App 50x). The glass material was chosen to be fused silica for better thermal load capacity. Later, custom objectives were designed and purchased (Special Optics) to sit snugly inside our re-entrant windows and to correct for the 3.5 mm glass thickness while giving a high NA of 0.6. Under vacuum, the glass has a slight bend as shown in Fig. 2.2. At the point of maximum deflection, up to 2.6 microns of bending is observed. This contrasts with current atom array experiments [219], which tend to use 5 millimeter thick rectangular glass-cell. Simulation of a 5-millimeter rectangular glass piece made of fused silica (30 mm *150 mm) shows only up to 0.17 microns of bending at the maximum deflection point. This additional glass bending

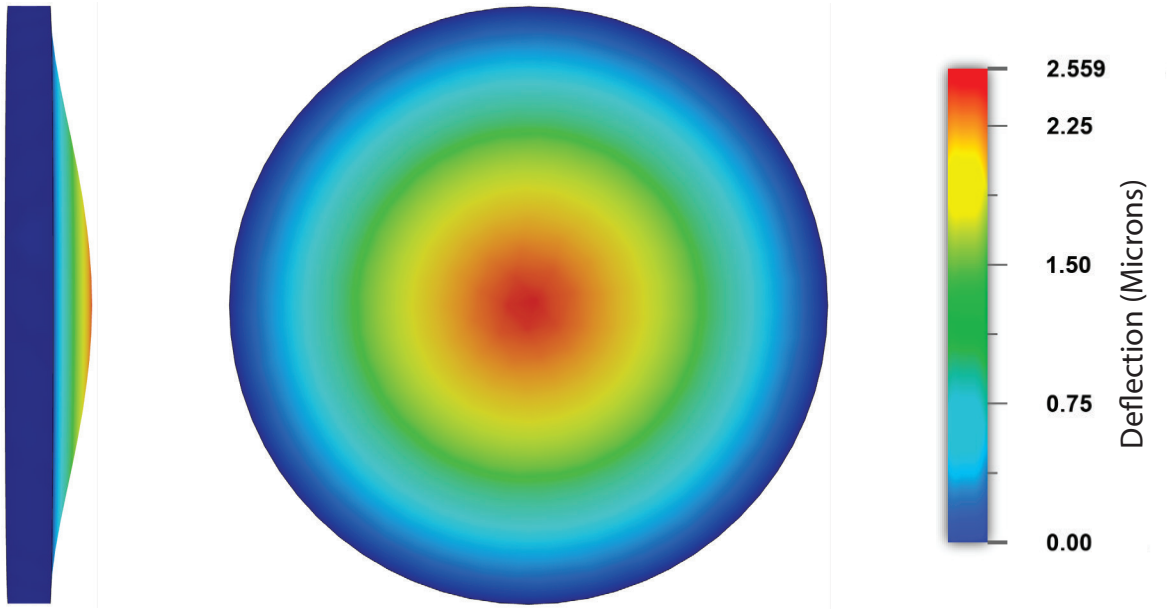

Figure 2.2: Simulated glass bending of the re-entrant window with a diameter of 50.8 millimeters and thickness of 3.5 millimeters. The left image shows the side profile with visible bending, while the right image is the bending profile across the diameter of the glass. The center of the glass bends up to 2.6 microns under UHV conditions.

in our system can introduce position-dependent spherical aberrations on the tweezer. However, limitations arising from this have not been observed.

For sourcing cesium atoms, we use alkali dispenser wires from SAES. The dispensers are attached directly to a feedthrough using in-barrel connectors. We added two dispensers during our first bake in 2021 and continuously used one of them at a 3-4 amp current before replacing it in our 2025 bake. While the atoms were still being dispensed, we noticed some fluctuations in the dispenser current which led to its replacement. The feedthrough is connected directly to the bottom 2.75" conflat on the chamber. Many current-generation atom array experiments use a 2D MOT setup for increasing atom-array lifetime, as this allows for differential pumping and targeted delivery of atoms to the 3D MOT region. This

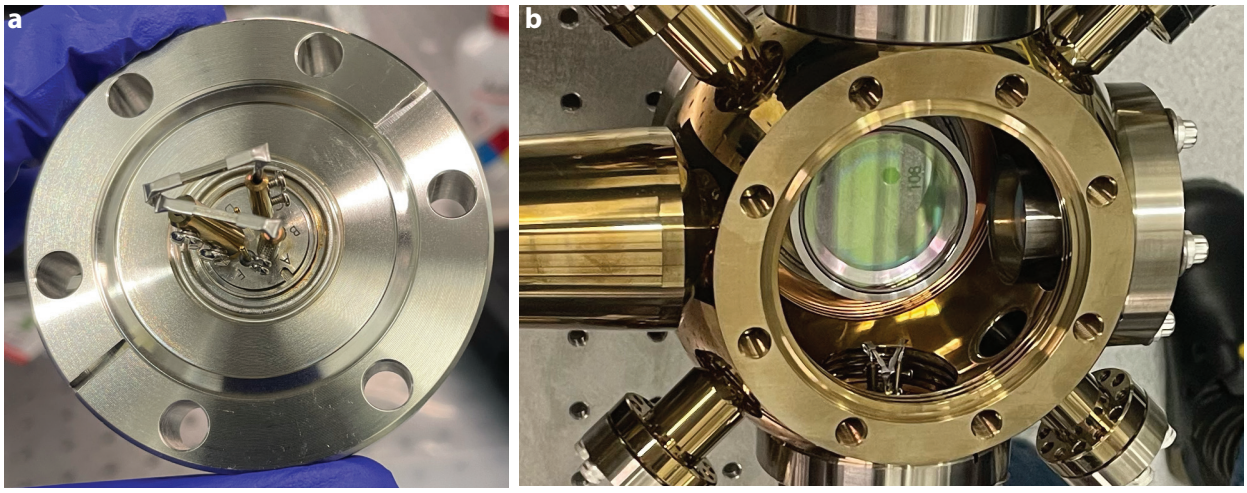

Figure 2.3: Cesium dispenser wires are mounted directly to the feed-throughs using in-barrel connectors. The feed-through is then attached directly to the science region where MOT and atom arrays are made.

strategy provides a low atom density in the science region, allowing longer background gas collision-limited lifetimes of atoms in tweezers. Instead of the 2D MOT, we are using a small chamber with hot atoms dispensed directly at the trapping region. Although this could seem counterintuitive, our main objective is to make sure we have enough atomic flux inside the chamber to form a MOT despite having the large chip structure blocking the MOT overlap region. At the same time, we also keep the combination ion-getter pump with its getter sticking into the chamber region to reduce pressure buildup. A pleasant outcome of this resulting architecture was atom-arrays with background-collision-limited lifetimes close to a minute, as shown in Fig. 2.4, before the placement of the chip or the chip mounts. This indicates that this chamber design can support large atom arrays comparable to the state of the art computation simulation experiments without the requirement of any 2D MOT [34, 220].

Finally, the 2.75" flange on the top side of the chamber (opposite to the feedthrough

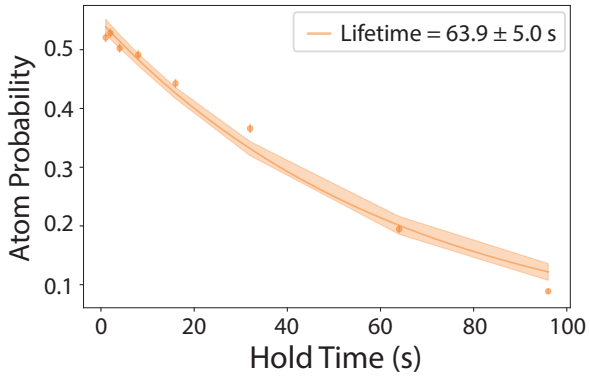

Figure 2.4: Atom lifetime measurements before the chip and chip mount were placed inside the chamber. The probability for an atom to survive in the tweezer trap was measured with varying hold times, indicating close to a minute-long lifetime. At time zero, the atom probability is around 0.5, and is limited by the stochastic loading of atoms into the tweezers.

) was left as a viewport for observation. One of the reasons for the long atom lifetimes observed in our chamber is the small overall volume (and surface area). The overall volume of the chamber is approximately 1.1 liters. However, ~ 0.08 liters is occupied by the pump and another ~ 0.1 liters by the re-entrants, bringing the overall volume of the chamber less than a liter, making the pumping easier.

2.3 Chip mount

The chip was mounted inside the chamber using a modified SEM (Scanning Electron Microscope) mount that was machined down to 4 mm in width. This reduction in width was to have minimal overlap with the MOT beams. The SEM mount was then mounted to an aluminum plate with set-screws tightening them in place. During this process, there are two degrees of freedom; to rotate the SEM mount in its axis and how deep it sits in the aluminum plate when it is screwed down. We fix both these degrees of freedom while imaging the chip inside the chamber with our tweezer objectives. This is possible in our system as the cham-

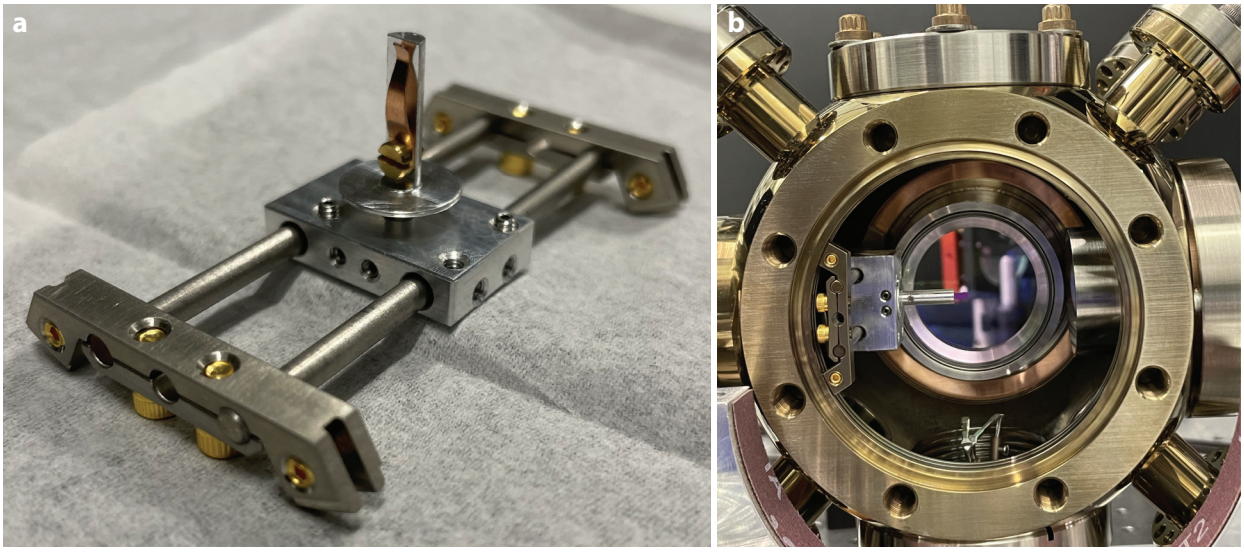

Figure 2.5: a) The mount for placing the photonic chip close to the MOT/atom array. A modified SEM mount serves to clamp the chip down. The required degrees of freedom to get the chip at the right angle and distance from the objective are enabled by this design. b) The chip is placed in the chamber using groove grabbers. The re-entrant in this image can be seen to be different from Fig. 2.3, as it was replaced to achieve the use of a higher numerical aperture lens for coupling into the photonic devices.

ber is all metallic and allows us to open one side of the chamber and make adjustments to the chip mount while still keeping the imaging system through the other re-entrant viewport intact. The plate is attached to the chamber using a pair of aluminum rods using set screws which in turn are attached to the chamber using grove grabbers on the 4.5" conflat as shown in Fig. 2.5. The aluminum plate is slidable and can be used to coarsely keep the chip at the center of the chamber. This was done the first time the chip was mounted inside the chamber using a set of alignment lasers and later verified by closing one re-entrant and making sure the chip was within the working distance of the objectives.

Each time, for chip replacement, only the modified SEM mount has to be taken out. The chip is mounted onto the SEM mount outside the chamber and positioned back in the chamber while being imaged using an objective to fix the two degrees of freedom of the SEM

mount.

The chip and the mount structure are designed to have as minimal overlap with the MOT beams as possible while still maintaining the required flexibility. However, the presence of the chip and chip mount have effects on the MOT loading and atom arrays. Both the chip and the mount overlap with the MOT beams leading to their clipping, and a slit shadow formation on our MOT beams. As two of our MOT beams are retroreflected, the overlap region can be further limited, leading to a lack of MOT formation or having a leaky MOT. However, we are still able to have a visible MOT of size ranging in a few millimeters. A typical MOT optimized for loading tweezers onto the devices is shown in Fig. 2.6. Before the chip mount is placed inside the chamber, the MOT is large as shown in Fig. 2.6 a). After the placement of the chip and the mount, the MOT beams are scattered by them, reducing the MOT size as well as increasing the scattering in the chamber as shown in Fig. 2.6 b). The white glow on the chip mount corresponds to the scattered MOT beams.

To generate the magnetic field gradient needed to trap atoms in the MOT and to offset the background magnetic field (or establish the quantization axis), one option is to keep the coils inside the chamber. However, since our chamber size is small, the mounting inside is challenging. Furthermore, this could add more outgassing inside the chamber, offsetting any benefit coming from the small volume of the chamber. To avoid these challenges, the MOT coils (a pair of coils in anti-Helmholtz conditions) and the three magnetic field offset coils (three pairs of coils in Helmholtz configurations) are made to sit around the chamber. As the distance between a pair of coils increases, the requirements of their size and the number of turns in the coils also increase. This stems from the fact that to maintain Helmholtz or

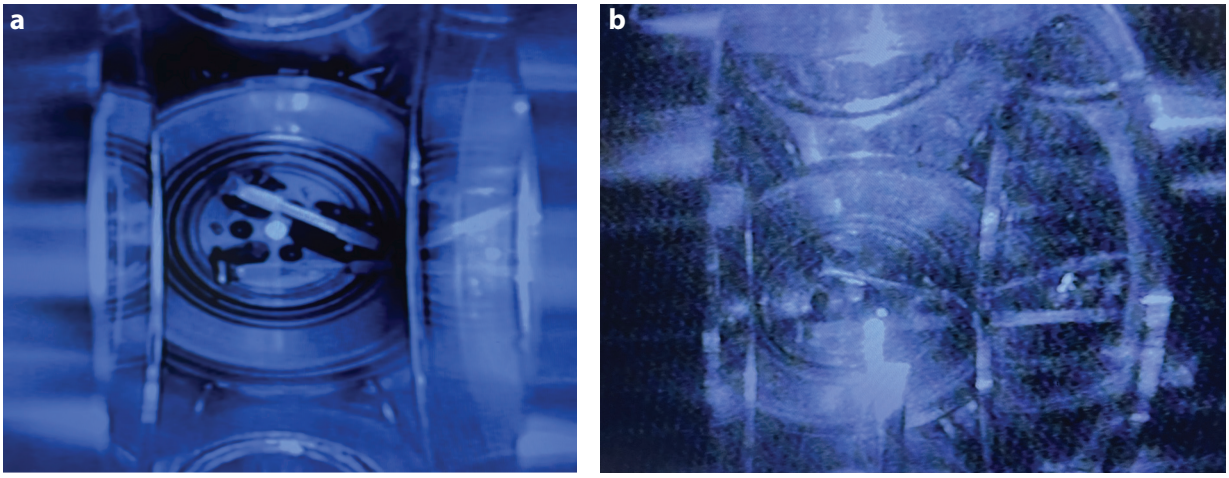

Figure 2.6: a) Atoms trapped in MOT before the placement of the photonic chip or the chip mount. b) Atoms trapped in a MOT after the placement of the photonic chip. Scattering of the MOT beams on the chip and the mount can be noticed. The MOT sizes are limited by the reduction in the overlap of beams that form the MOT. The MOT beams are clipped by the device and the mount, increasing the overall scattering inside the chamber.

anti-Helmholtz conditions, there is a fixed ratio of separation between the coils and their radius. The number of turns requirements for the coils is based on the amplitude needs of the fields. For our systems, the separation between a pair of coils is limited by the size of the chamber. We design anti-Helmholtz coils for our MOT generation and Helmholtz coils for offsetting magnetic fields in the x and z directions. For offsetting magnetic fields in the y direction, we use an imperfect anti-Helmholtz coil. Although imperfect (from simulations and later from direct measurements), we confirmed that the coils can provide a uniform magnetic field in a centimeter-long region where atoms are trapped. This design results in a unique system in which the chamber size is smaller than the coil size as shown in Fig. 2.7.

Experiments that require repeated opening of the vacuum chamber tend to use a load-lock system to avoid repeated baking of the whole chamber. Although our chamber does not have a load-lock, it is small enough that it can be baked directly in a custom home-built

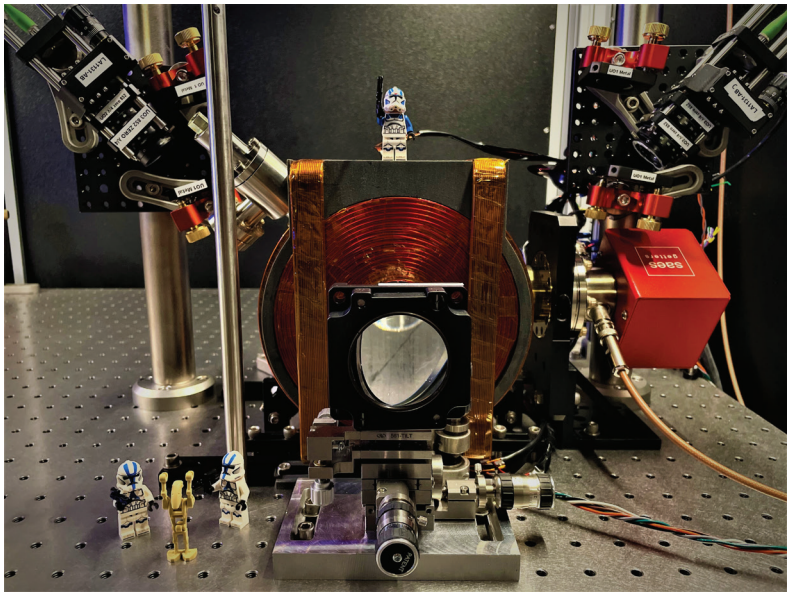

Figure 2.7: The chamber with the MOT coils and the objective mount attached to it. The optics for diagonal MOT beams can also be seen in the picture (top-left and top-right corners), along with the objective mount.

oven. This allows us to move away from heating tapes, glass fiber insulations, and variable auto-transformers (variacs) for voltage regulation during our bake procedure. Instead, the oven is digitally controlled and can be remotely operated, automatically executing the entire baking profile with minimal or no supervision. For each round of the bake, we take the chamber out and place it in the oven. Since we use re-entrant windows for high NA imaging, the objectives have to be pulled out of the re-entrants before the chamber is taken out. Further, in the current orientation, the MOT coils also have to be removed from their location for the chamber to be taken out. For repeatability in magnetic field values, the coils are mounted either on the chamber mount or referenced to the chamber itself.

2.4 Optical layout

The size of our chamber was made small by limiting most degrees of freedom. This necessarily means that we have little flexibility in possible excitation beam paths and the total optically addressable volume inside the chamber. In this section, I will cover how we combine all the required capabilities in our system, given our experimental geometry. We have eight viewports in the chamber, out of which two 4.5" re-entrant viewports are occupied by objectives used for imaging and tweezer formation. A 2.75" re-entrant viewport is occupied by another objective for coupling into the devices. Out of the remaining five viewports, four are protruding out of the chamber in the plane orthogonal to the tweezer viewport. They are designed to provide the two orthogonal (diagonal) MOT beams (The optics for this is seen in Fig. 2.7). To facilitate three orthogonal MOT beams, the third MOT beam direction has to coincide with the tweezer objective direction and lacks additional viewports to achieve this. Instead, we send the MOT beams through the objectives. MOT beams are focused at the back focal plane of each of the objectives to obtain collimated counter-propagating MOT beams inside the chamber. The lens used to focus the MOT beam to the back focal plane of the objective can be seen in Fig. 2.7. Each of the MOT beams includes a repump laser, locked to ($6S_{1/2}$ F=3 $\rightarrow$ $6P_{3/2}$ F' = 3-4 crossover) atomic transition using saturation absorption spectroscopy and a tunable cycler laser that is offset locked to the repump laser. Both the cycler and the repump beams are generated from DBR lasers (Vescent).

In conventional cold atom experiments with high NA imaging, MOT beams are not sent through the objectives as fluorescence imaging is done at the same wavelength as the MOT.

This makes the separation of MOT beams from the fluorescence challenging. In some experimental geometries, this has been overcome by having a hole through the objective (through which the MOT beams are sent), by having a tiny mirror close to the back focal plane of the objective where MOT beam is focused [42], or by polarization filters.

In our work, this challenge is naturally overcome as our imaging is not at the MOT frequency. For imaging atoms in the MOT and in the atom-array, we use our two-color imaging scheme described in the following chapters. This background-free scheme uses 852 nm and 1470 nm excitations, whereas the fluorescence is collected at 895 nm to image the atoms. Since the excitation wavelengths are sufficiently far away from the fluorescence wavelength, they can be easily separated using commercially available dichroics. For the 852 nm excitation, we use the same beams as the MOT generation. For the 1470 nm excitation, we use a dichroic to add the path to one of the diagonal MOT beams. The 1470 nm beam is generated from an external cavity diode laser (Toptical DL Pro) and is locked to the atomic transition using a double resonant optical pumping (DROP) lock.

For the optical tweezers, we use a home-built External Cavity Diode Laser (ECDL) at 935 nm and amplify the power using a tapered amplifier (MOGLabs MOA). The tweezers are combined with the imaging path using another dichroic before being sent to the chamber through the objective. The RF frequencies that drive the Acousto Optic Deflectors (AOD) (AA Opto-Electronic) are generated using an Arbitrary Wave Generator (AWG) for an 8 $\times$ 8 array of tweezers and a Field Programmable Gate-Array (FPGA) for the 1D arrays

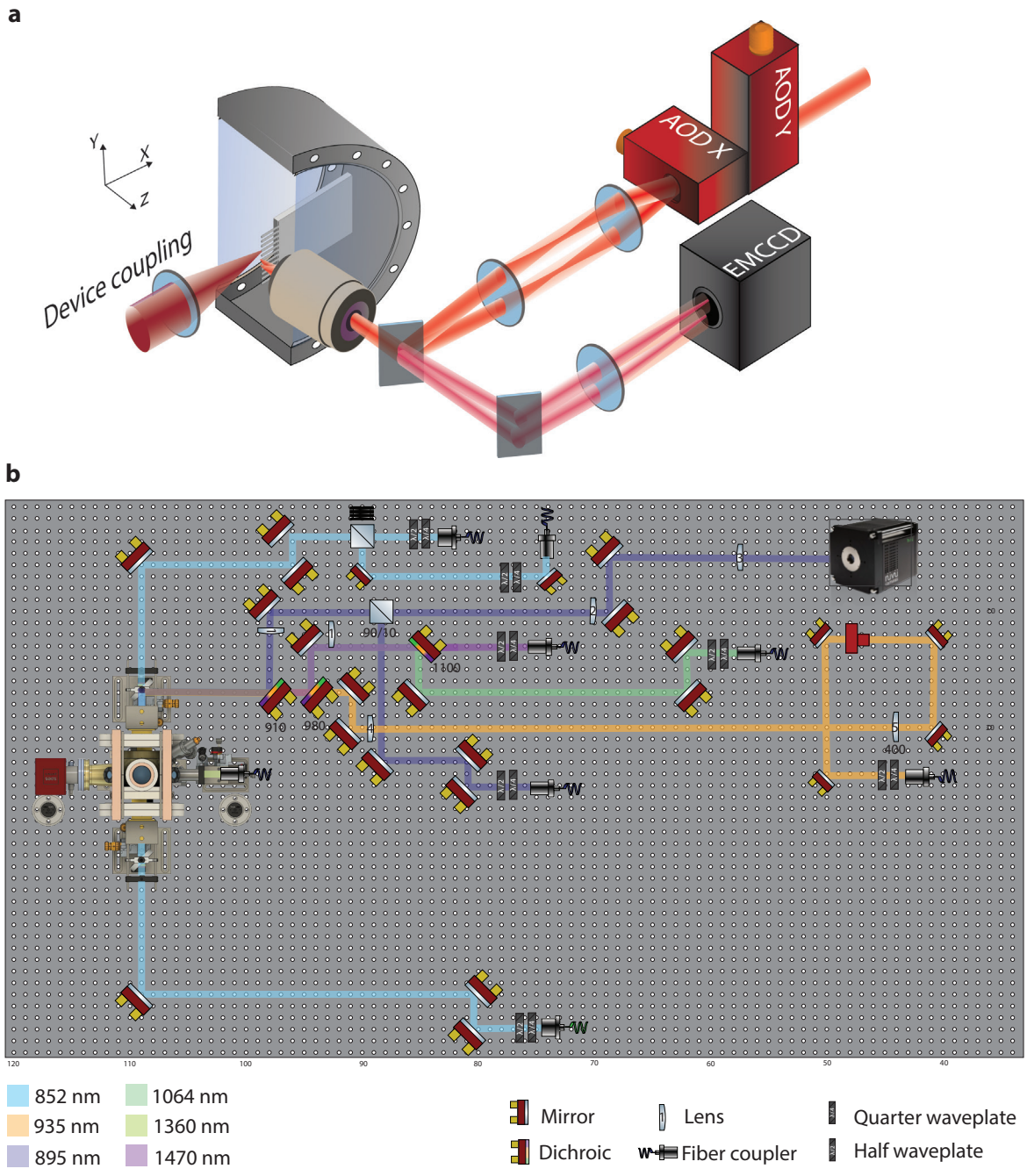

Figure 2.8: a) A cartoon of the basic setup. A nanophtonic chip is placed inside the vacuum chamber and is characterized by an objective/lens sitting outside the vacuum chamber. Tweezers are used to manipulate the atomic positions inside the chamber (made possible due to our imaging scheme), and the atoms are imaged using an EMCCD camera. b) A schematic of how different wavelengths are combined in our system. Details of different beams are given in the text. All the beams shown here are combined into the chamber through the objective.

(Quantum Machines, OPX).

For locking the cavities used in the single-photon source chapter, we use a 1060 nm laser (AeroDiode) which is combined to the tweezer path with another dichroic before being sent to the chamber. For generating single photons, we pulse an 852 nm laser that is separate from the MOT beams. This laser (Topica DL Pro) also goes through the objective and is focused on the atomic position on top of the cavities. We combine this beam with the MOT beams through the objective using a 70 - 30 beam splitter. The 1470 nm laser used for high Rabi frequency excitation also goes through the objective and is focused onto the atoms trapped on top of the cavity. We use a fiber switch to move the 1470 laser to either go through the objective for high Rabi frequency excitation or mix it with the diagonal MOT beam for wide-field imaging of the atom array. The schematic in Fig. 2.8 shows how the different beams explained here are combined into the setup. For implementing the entangled photon generation based on the theoretical scheme described in Chapter 5, an additional pulsed 895 nm laser is also required. For this, we use a 90 - 10 beam splitter on the atom array imaging path to combine it with the 895 nm fluorescence collected using the background-free imaging scheme.

2.5 Conclusions and future improvements

The chamber presented in this chapter combines atom arrays with a photonic chip containing an array of cavities in a small UHV chamber. The chamber allows the ability to cool atoms and image them in 20-40 ms while keeping a photonic chip next to it. We note that almost all capabilities of normal cold atom experiments are retained in this setup while having the

additional capability of having a photonic chip.

Given these, there are a few additional capabilities that would be beneficial to have in our system. Currently, the background-free imaging technique allows us to image our atoms through our high NA objective in spite of one of our MOT beams going through it. While this satisfies our requirement, the ability to image in the cycling transition can have its own benefits. During the building stage of the experiment, we had to compensate for the Stark shift from the tweezer on the upper imaging transition, while also compensating for the power of both the imaging transitions to image tweezer atoms in the MOT. This makes it difficult to separate the loading and the imaging issues. With the use of magic wavelength tweezers, the ground-state imaging capability would readily allow us to image atoms in tweezers, given that they are sufficiently far away from the photonic chips. Further, having this ability would allow for a better understanding of the limitations of the scattering as a function of distance from the photonic chip and would allow for a hybrid approach where atoms far away from the devices are selectively imaged using a ground-state cycling transition. The ground-state imaging capability can be added to our system by not having the MOT go through the objective. To achieve this capability, an 8-beam MOT can be used with a slight modification to the current chamber by having seven additional protruding 1.33" CF flanges. This design was considered in between, however was not pursued.

Another design change that could be beneficial is the design/mounting of the MOT and the offset coils. In the current setup, one of the offset coils is smaller than the diameter of the chamber around the protruding 1.33" conflats, and the removal of the chamber for baking purposes requires the coils to be removed. Modifications to the coil sizes can allow

the chamber to be pulled out while keeping the MOT coils intact. However, this necessarily requires larger coils, demanding either more current or additional coil turns, which could increase thermal and inductive effects near the chamber. Additionally, for the chamber to be pulled out without the removal of the coil, the position of the gate valve has to be moved from its current position to close to the pump. Further, the requirement of fixing the photonic chip inside the chamber while referencing the existing optics requires the chamber to be opened in its normal experimental position, which necessitates the removal of the coils. Due to these reasons, this design was not pursued.

Finally, going to higher glass thickness can reduce the aberrations originating from the glass bending. We estimate a deviation of less than one micron for 5 mm thick glass (approximately 160 nm), compared to the current 3.5 mm thickness. This can mitigate some of the aberrations and can lead to better tweezer homogenization and more identical behavior across different atoms in the array. These aberrations can also cause variations in the loading behavior to the photonic devices based on the tweezer positions. These issues can be reduced by this increase in glass thickness.

CHAPTER 3

PHOTONIC-CHIP DESIGN AND FREE-SPACE COUPLING

3.1 Introduction

Atoms have been coupled to nanophotonic waveguides [163] and cavities [162]. For the nanophotonic cavity experiment, an individual nanophotonic cavity was attached to the end of a tapered fiber, reducing the potential effects from the clipping of the MOT beams. However, in the nanophotonic waveguide experiment, the waveguides were attached to a chip, and this resulting geometry had a significant effect on the MOT loading, making deterministic loading of atoms challenging. In our experiment, combining atom-arrays with cavity arrays is one of the central goals and this requires the presence of a chip close to the atom region. In this chapter, I will cover the design of the chip we use for the cavity arrays that enable a MOT, as well as the deterministic loading of atoms in tweezers in the vicinity of the cavities. Furthermore, I will also demonstrate a new way of coupling light into photonic devices using long focal length lenses, which could be an enabling technology for future atom array experiments.

3.1.1 Design considerations

The presence of large dielectrics can have a significant impact on atom loading. To reduce the effect coming from the dielectric it is necessary to make the chip in a way that minimizes scattering of the MOT, cooling, and the imaging beam near the atom array region. Finally, we want the atom array region as close to the chip as possible. The design that we came up

with is illustrated below.

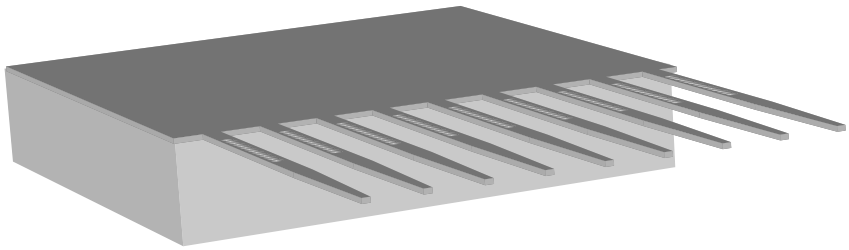

Figure 3.1: An array of waveguides with embedded cavities made in SiN are suspended throughout the thickness of the silicon substrate. The devices are 70 μm long and 1.1 μm wide. The chip is 2 mm wide, 7 mm long and the substrate is 500 μm thick. Waveguides are suspended through this entire 500 μm thickness.

Here, an array of waveguides, with cavities embedded in them, is suspended at the end of a photonic chip as shown in Fig. 3.1. The substrate beneath the waveguides is etched throughout the thickness of the chip to suspend the devices and to have optical access from both directions. For the chip, the dimensions are chosen to be 2 mm wide and 7 mm long to minimize the volume occupied by the chip in the MOT region. Here, the MOT region is defined by the overlap of beams that are 10 mm, 10 mm, and 1 mm in diameter, where the 1 mm MOT beam is generated by a beam focused on the back focal plane of the tweezer objective. The advantage of this design is two-fold:

- As the target devices are at the edge of the devices, the chip can be placed with minimal overlap with the MOT ($\sim$100s of microns). This allows a large unobstructed MOT

region, where atoms are able to be trapped and cooled right next to the semiconductor chips. This alleviates requirements of cascaded MOT's [163] or lattice-based transport that involves cooling atoms far away and moving the cooled atoms to the photonic chips.

- While getting cold atoms close to a photonic chip itself is a challenge, the chips themselves can be much larger than a typical MOT. This brings a second problem of transporting atoms from the vicinity of the chips to the actual photonic devices themselves. In our design, as the waveguides and cavities are at the end of the chip, atoms from the MOT can be directly transported to the photonic devices using optical tweezers.

Each chip is designed with 150 cavities; all facing the MOT with 11 microns separation between each of them. This includes 50 cavities with three, four, and five mirror holes on the coupling side respectively. The different mirror numbers are added to get different levels of quality factors in the same batch.

3.2 Photonic crystal cavities

Photonic crystals are periodic dielectric structures that control the propagation of light in a manner analogous to how semiconductor crystals control electron flow [221]. Unlike homogeneous materials, photonic crystals possess a spatially varying refractive index that is periodic, creating discrete translational symmetry rather than the continuous translational symmetry found in free space or homogeneous dielectrics.

Traditional crystals, composed of atoms or molecules, exhibit a periodic arrangement with discrete translational symmetry. This means they are invariant under translations by specific distances corresponding to integer multiples of a fundamental lattice vector. Similarly, photonic crystals do not have continuous translational symmetry, and are only invariant under translations that are multiples of a fixed step length. Consider a simple one-dimensional photonic crystal structure, which is repetitive along one direction (say x direction). While it maintains continuous translational symmetry in the y direction, its symmetry becomes discrete in the x direction. Let a be the lattice constant, representing the basic step length along the x-axis. The primitive lattice vector, similar to conventional solid-state physics, is then given by $\hat{a} = a\hat{x}$. The dielectric function $\epsilon(\hat{r})$ characterizing this system satisfies the condition:

$$\epsilon(\hat{r}) = \epsilon(\hat{r} + \hat{a})$$

This means that the dielectric function remains unchanged when translated by the primitive lattice vector $\hat{a}$. By iteratively applying this translation, it satisfies $\epsilon(\hat{r}) = \epsilon(\hat{r} + n\hat{a})$ where n is an integer. This discrete translational symmetry forms the foundation for the unique optical properties of photonic crystals. Given these symmetry requirements, the solutions to the Maxwell equations in these periodic structures need to commute with the translation operators, giving rise to optical Bloch equations similar to those in solid state physics [221].

$$\mathbf{H}(., x, .) \propto e^{ik_x x} \cdot \mathbf{u}_{k_x}(., x, .) \tag{3.1}$$

Here, (.) represents other degrees of freedom, including 'y' and 'z' dimensions, k_x is the wavevector in the $\hat{x}$ direction, and H/u are the solutions to Maxwell's equations for the structure. The basic repeating structural unit of the photonic crystal is called the *unit cell*. This is the dielectric arrangement which is repeated over space by the translation of the primitive lattice vectors. Similar to the solid-state Bloch equations, restricting the Hermitian eigenvalue problem derived from Maxwell's equations to the unit cell leads to a discrete spectrum of eigenvalues [221]. For each value of the wavevector $\mathbf{k}$, we can expect to find an infinite set of modes with discretely spaced frequencies, each labeled by a band index n. This leads to the characterization of photonic crystal modes as a set of continuous functions, $\omega_n(k)$, ordered by increasing frequency and indexed by the band number. The collective information represented by these functions defines the band structure of the photonic crystal. Regions in the band structure where $\omega > ck_{||}$ (with $\omega = c|\mathbf{k}| = c\sqrt{k_{||}^2 + k_{\perp}^2}$) form the light cone, which represents modes that can freely propagate in the surrounding medium. The solutions to Maxwell equations in this region obey Snell's law. Conversely, localized electromagnetic solutions within the photonic crystal exist below the light line ($\omega < ck_{||}$), where light remains confined within the high-refractive-index material, forming index-guided modes described above. These modes have solutions in free space with imaginary $k_{\perp} = \pm i\sqrt{k_{||}^2 - \omega^2/c^2}$ (as $k_{\perp}^2$ has to be < 0 for $\omega < ck_{||}$), corresponding to fields that decay exponentially away from the dielectric (evanescent waves). The unit cell's geometry and material composition determine the overall band structure.

A photonic crystal cavity is created by introducing a defect into the periodic structure of

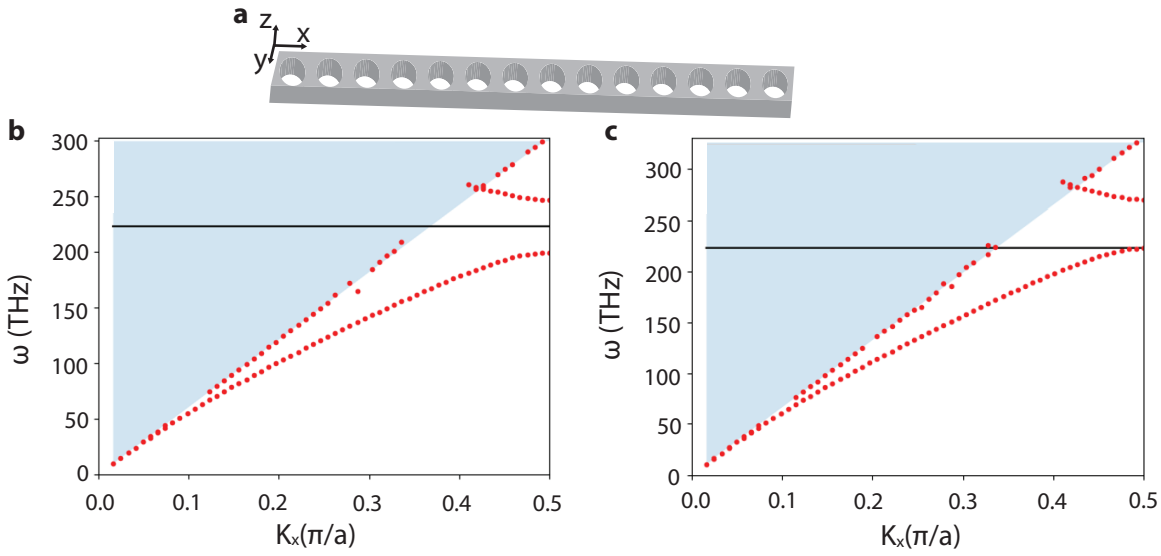

Figure 3.2: a) Cartoon of a waveguide with periodic holes in the x direction. b) Band diagram calculated using the MEEP FDTD program for a waveguide with periodic elliptical holes with a filling fraction of 0.47, showing a bandgap at the target frequency of 220 THz (solid black line). c) Band diagram of the same waveguide with a modified filling fraction of 0.52, showing that the 220 THz has allowed propagation under this band structure. The region above the light line is shaded in blue.

a photonic crystal. Within the band gap of a photonic crystal, no modes are allowed, and the density of states (the number of possible modes per unit frequency) is zero. By deliberately perturbing a single lattice site within the photonic crystal, we can create a single localized mode or a set of closely spaced modes that have frequencies within the band gap. These localized modes effectively trap light within the engineered defect, creating the foundation for a cavity resonator. The defect can be a variation in the size or shape of a hole, or an intentional modification of the refractive index within the lattice. Fig. 3.2 b) shows the band diagram of a waveguide with periodic holes in the x direction. The dimensions are chosen so that the resultant bandgap is centered around our target frequency of 220 THz. In the bandgap region, the index modes cannot propagate, and form the mirrors as discussed in the following sections. We introduce a defect of the form Fig. 3.2 c) in the middle of the

cavity where there is an allowed propagation mode at the target frequency. In this chapter we will make use of these ideas to generate a photonic crystal cavity with a resonant mode close to the atomic transitions in the Cesium atom.

3.3 Waveguide and cavity design

The cavities were embedded in a waveguide with a width of 1.1 microns. For a good external photon coupling into fibers, these 1.1 micrometer waveguides were tapered down to 200 nanometer with a taper length of 40 microns. The choice of 200 nanometer wide coupling edge is described in the free-space coupling section. The spacing between each waveguide device is fixed at 11 microns. This choice is motivated from the requirement of having enough space for defocused tweezers to move between the devices and also to facilitate the free-space coupling introduced later.

To design the cavity we first fix our cavity thickness (z direction) to be 330 nm. This choice is made based on atom trapping considerations. As shown in Fig. 3.3, our tweezer trap position, where atoms will be trapped, on top of the photonic cavity follows a sawtooth pattern with the device thickness.

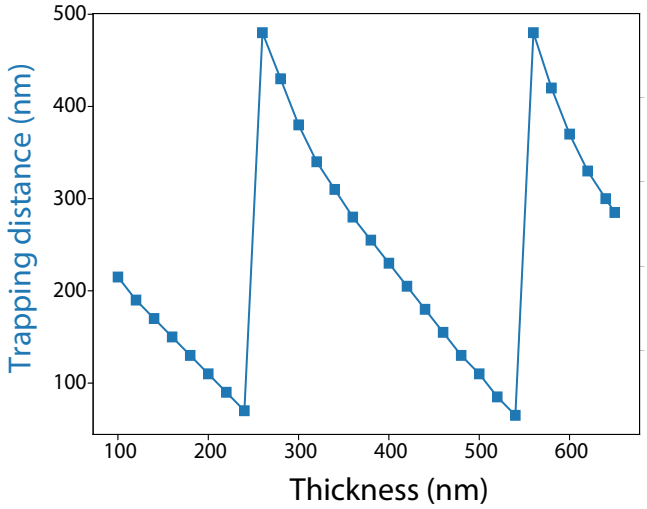

Figure 3.3: The trap position variation with respect to the thickness of the photonic device. Around 250nm thickness, the trap closest to the waveguide is ∼500nm away, making thickness close to 250 non-ideal for strong coupling.

This modification of the trap position also modifies the corresponding atom-cavity coupling experienced at each of those points. Ideally, a thickness with the largest atom-cavity coupling would be ideal for us. At a thickness of ∼200 nm, the atoms can be trapped on these devices with high atom-cavity coupling. However, we found that it is hard to get a good mode confinement, and thereby good quality factors at these thicknesses. At thicknesses close to 250 nm, the atomic trap shifts farther from the device as shown in Fig. 3.3, making the next device thickness region where the atomic trap is closest to the cavity to be around ∼500nm. However, at these thicknesses, the mode is mostly confined within the dielectric, and the atom-cavity coupling would again be minimal. The thickness choice of 330nm is made as a compromise with reasonable coupling strength, good polarization purity, and mode confinement.

Having the thickness fixed, we have the following parameters to optimize: device width

(w), hole size in x direction (hx), hole size in y direction (hy), hole-spacing (a), to control the quality factor as well as the resonance frequency of the cavity. An approach inspired by [222] and [223] was used to design the cavity.

- The value of initial hole spacing was taken to be a=$\lambda/2n_{eff}$, where n_{eff} is the effective refractive index of the slab, and λ is the target wavelength.

- For this value of a, the values of w, hy, and hx, are chosen to make a strong bandgap at the target frequency (a_m). This is done by simulating waveguides made up of these holes in Finite Difference Time Domain (FDTD) simulation and looking at their frequency-dependent reflection profiles. This can also be done by bandgap simulations as shown in Fig. 3.2 a)

- Having fixed the values of w, hy, and hx, the value of a for the cavity region (a_c) is optimized by finding the value of a that provides the low energy band edge at the target frequency. This is done by FDTD simulation of frequency-dependent reflection profiles, and can also be done by direct bandgap simulations as shown in Fig. 3.2 b).

- The cavity mirror strength is then obtained by quadratic tapering of the hole spacing. If the number of holes that makes up a single side of the cavity is N, and x=(hole index)/N; the hole spacing of one side of the cavity is tapered with the equation:

$$a(x) = \begin{cases} 1 - d\left(\frac{1}{4}(2x)^{3\eta} - \frac{3}{4}(2x)^{2\eta} + 1\right), & \text{if } x \leq 0.5 \\ 1 - d\left(2\left(1 - \frac{1}{2}(2(1-x))^{\eta}\right)^3 - 3\left(1 - \frac{1}{2}(2(1-x))^{\eta}\right)^2 + 1\right). & \text{if } x > 0.5 \end{cases}$$

Here d is the defect depth and can be calculated from $a_c = a_m(1-d)$, and η is a free parameter.

- In our case, we fixed the number of total cavity holes to be 20 (2N), making gaussian mirrors on each side to be made of 10 holes (n) each.

- Additional bandgap mirrors were padded on each side, with extra bandgap mirrors on the non-coupling side.

- Simulation using the above approach give quality factors in the few hundred thousands. This was followed by one-dimensional sweeps of η, d, number of bandgap mirrors, hy/hx, etc.

- Finally, five linearly tapered holes are added to the coupling side of the device to reduce losses during propagation from waveguide mode to block mode [224]. Fig. 3.4 shows the final dimensions and spacing between the holes.

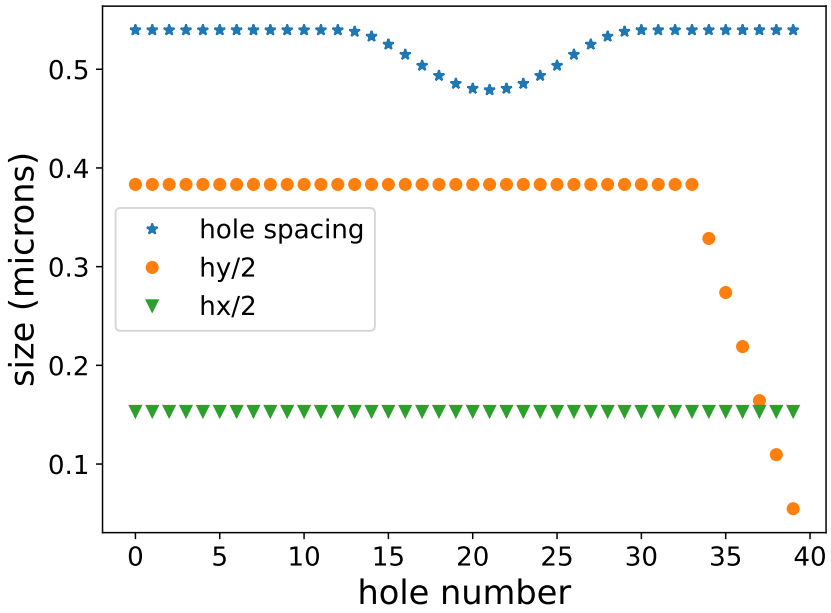

Figure 3.4: The hole spacing, hole size in y direction and x direction with corresponding mirror index.

Note that contrary to the approaches in [222] and [223], our hole sizes are fixed in order to reduce the size dependent variation from Ebeam process. The FDTD simulations above were done using Lumerical-FDTD software. After a few rounds of one-dimensional sweeps, the simulated cavity had a quality factor around 2.5 million.

3.4 Free space coupling

Since we are interested in distributing entanglement across networks, it is necessary for us to be able to efficiently extract photons from these devices. There are multiple approaches that can be used to collect photons from a cavity. The most common being a tapered fiber attached to the waveguide [225, 226]. In this approach, both the fiber and the waveguide are tapered down for mode matching. In a typical fiber, the mode is well contained inside

the fiber. However, as the fiber is tapered down, the dominant propagation mode will have a significant portion outside the fiber. By choosing the right end width for the tapered fiber and the waveguide, very low coupling losses can be achieved in this system [227]. Another popular approach for coupling light into and out of a cavity is using lens fiber [228, 229]. In this approach, a fiber with a focusing lens at its end is used to couple light into and out of a tapered waveguide. Typically these fiber edges are kept microns away from the target waveguides, and coupling efficiencies upto $\sim 85\%$ have been obtained using this approach [228].

While the above methods are well established and can result in high efficiency coupling of light into and out of the waveguides, they pose multiple challenges for integration into our system. 1) We have $\sim$150 cavities in our system, requiring 150 different fiber connections. As we work in UHV conditions in an unconventionally small chamber, routing these many fibers into the chamber itself becomes a challenge. 2) Having this many fibers going into the UHV system can affect the vacuum inside the chamber. 3) In both the above approaches, fibers have to be either touching the waveguide or have to be close enough to be able to couple with high NA lens fiber. In our current setup, this requirement necessitates that the fibers block the atoms in the MOT/atom loading/cooling region. This can significantly affect our ability to load atoms near these structures. An alternate option would be to keep the tapered edge facing the chip, so that the fibers can be on the other side of the MOT and will have minimal effect on atom loading and cooling. In this approach, the chances of devices breaking are higher as the entire device structure will have to be supported by the tapered ends. Adding tethers to support the structure can potentially overcome this

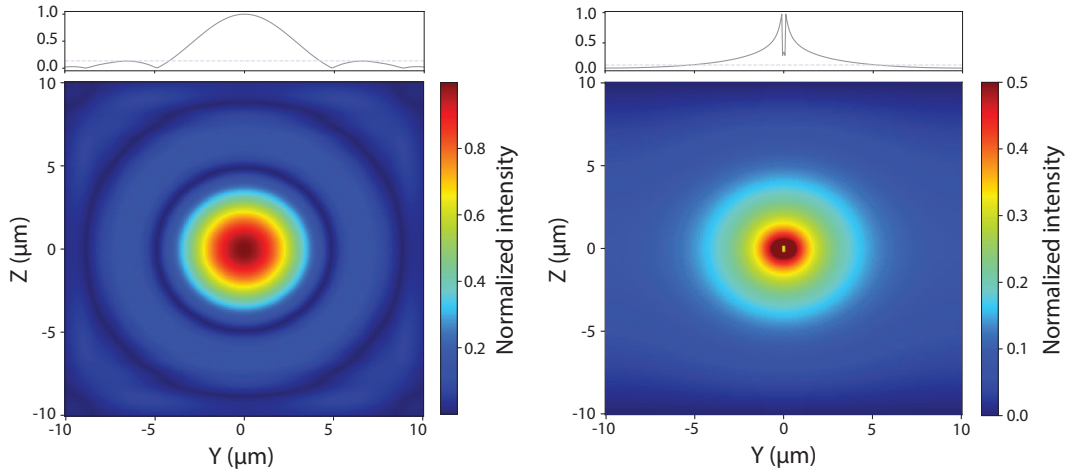

Figure 3.5: Normalized 2D intensity profile of the diffraction-limited mode generated by a 0.17 NA lens. Line-cut along the Y axis at Z=0 is shown above. The dashed horizontal line shows the 1/e2 amplitude. b, Second TE mode supported by the waveguide taper end. The corresponding line cut along the Y axis at Z=0 is shown above. The dashed horizontal line shows the 1/e2 amplitude.

challenge and help support the waveguide. In lens fiber coupling, additional thin film layers might be required between silicon nitride and silicon to make the entire coupling structure to work. To overcome these challenges, we came up with an approach that can enable coupling from outside the vacuum chamber to any target device of interest. The key idea behind our approach is that the mode supported by the tapered end of a waveguide is similar to that of a focused Gaussian. (A similar idea was also pursued in the Kimble group to couple light from outside the vacuum chamber to silicon nitride waveguides [199, 218].) To demonstrate this, in Fig. 3.5, we show an image of the mode supported by a silicon nitride waveguide with a width of 200 nanometers and that of a diffraction-limited Gaussian generated by a lens with a numerical aperture of 0.17. While the mode is Gaussian for a focused laser beam (Fig. 3.5 left), and exponential for the taper end width (Fig. 3.5 right), the fields have significant overlap as calculated by equation 3.2.

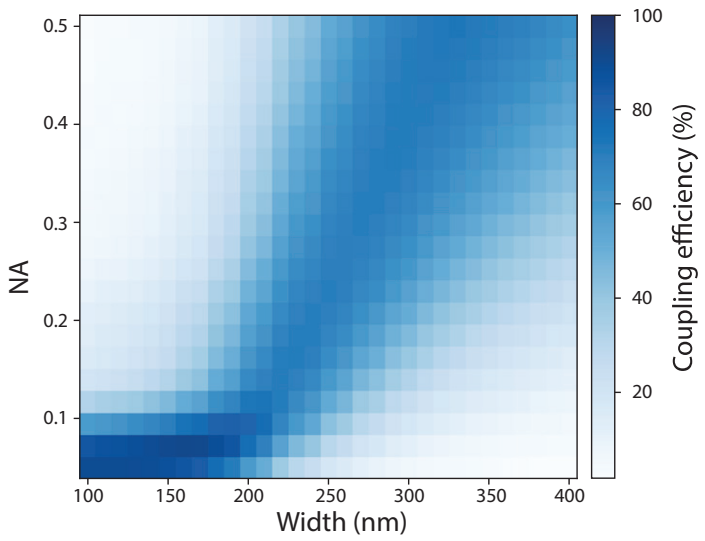

Figure 3.6: Estimated coupling efficiency from Lumerical FDTD simulation for a waveguide with a constant thickness of 330 nanometers.

To understand the limits of the coupling capability, we then look at coupling efficiencies from modal overlap. We compare the modes of tapered waveguides of silicon nitride with the diffraction-limited modes supported by different numerical aperture lenses. The coupling efficiency is calculated using modal overlap equations given by:

$$\text{overlap} = \text{Re}\left[\frac{\left(\int \vec{E}_1 \times \vec{H}_2^* \cdot d\vec{S}\right)\left(\int \vec{E}_2 \times \vec{H}_1^* \cdot d\vec{S}\right)}{\int \vec{E}_1 \times \vec{H}_1^* \cdot d\vec{S}}\right] \frac{1}{\text{Re}\left(\int \vec{E}_2 \times \vec{H}_2^* \cdot d\vec{S}\right)}. \tag{3.2}$$

Here, E1 (E2), and H1 (H2) correspond to the electric and magnetic field components of the mode supported by the tapered waveguide (lens with a given NA). The coupling efficiencies corresponding to different taper end widths and lenses with different numerical apertures are shown in Fig. 3.6. Coupling efficiencies greater than 90% can be achieved by simple tapering of the waveguide and choosing the right combination of lens.

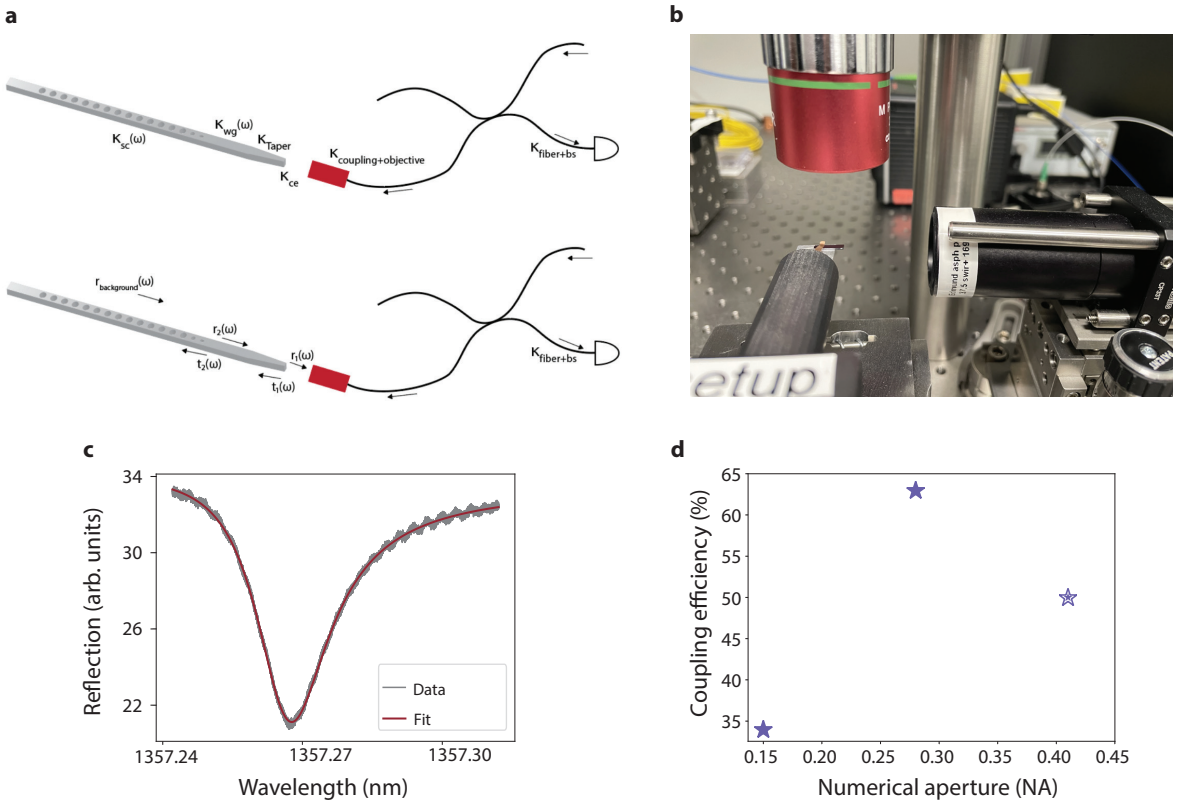

Figure 3.7: a) Different losses, reflections, and transmissions involved in estimating the free space coupling efficiency. K_{sc} stands for the scattering losses in the cavity, K_{wg} is the waveguide propagation loss, K_{Taper} is the loss in the propagation coming from an imperfect taper, K_{ce} is the loss from mode matching of the taper end mode and the coupling lens, $K_{coupling+objective}$ are the losses from optics including any fiber coupling, and $K_{fiber+bs}$ is the loss from fiber propagation and the beamsplitter. Similarly, uncoupled light can scatter back into the coupling lens as quantified by $r_{background}$, imperfect coupling between waveguide and block modes could lead to reflections r_2, and Fresnel reflection from the air-waveguide interface r_1. These losses and reflections are in general frequency dependent, as indicated by the ω dependence of the parameters. b) Experimental free-space coupling setup. An objective mode is focused onto the device edge on a chip, enabling high coupling efficiency. c) A typical device spectrum obtained using the setup. d) Measured coupling efficiencies for different numerical apertures for a device end width of 180 nm.

For experimental testing of the free-space coupling, a set of devices were made, and the devices were suspended on one side. The devices were undercut for tens of microns and separated from each other by eleven microns. This separation was chosen to make sure the Gaussian modes of different NA used in the experiment have minimal modal overlap and minimal clipping from neighboring devices. Making taper end widths $\leq$100 nm is challenging due to the charging effect during the e-beam process, as it distorts the taper edges. This is a function of device thickness and can be potentially overcome in designs with a device thickness close to $\sim$200 nanometers. Different losses and reflections involved in estimating the coupling are shown in Fig. 3.7 a). K_{sc}, K_{wg}, K_{Taper}, and K_{ce} are the waveguide/cavity losses and stands for the scattering loss, propagation loss, loss in the propagation through the taper, and loss through modal overlap mismatch. $K_{coupling+objective}$ and $K_{fiber+bs}$ stand for the losses in the optical path coming from transmission loss and the beamsplitter loss. Similarly, we also have uncoupled light reflecting off the substrate ($r_{background}$) and coupling back into the detection path, and Fresnel reflections from different refractive index boundaries (r_1). Fig. 3.7 b) shows the coupling setup, with devices clamped on a modified SEM mount. Aspheric lenses sitting at distances $\geq$30 mm were used to couple in and out of the devices. A typical cavity spectrum collected using a similar setup is shown in Fig. 3.7 c). From Fig. 3.7 d) we see that the coupling efficiencies can be improved by choosing the right numerical aperture for our devices. Greater than 65% coupling efficiencies were measured using a near NIR objective. Getting custom anti-reflection coated objectives at our target wavelength can readily allow this level of coupling efficiency in our setup. The first round of coupling attempts turned out to be challenging due to our cavity resonance

wavelength of 1359 nm. For one, our cameras were not designed to see telecom wavelengths, this meant that we had to align the two modes without the ability to see them. We sent laser beams at ∼852 nanometers to roughly align our lens mode to the waveguide edge. Due to spherical and chromatic aberrations, the telecom modes did not have a good overlap at these alignment set points. Further adjustments around these points were done using micrometer screws and feedback was done based on the amount of reflected signal. The underlying silicon substrate also had considerable reflection, which meant looking at alternate confirmations like a periodicity of 11 microns and polarization dependence to confirm the collected signal is from the waveguide, and not the substrate. Large polarization-dependent oscillations are the best indicator to know if the collected signal is from the waveguide or the substrate. A second challenge was the presence of significant water absorptions around these wavelengths. As the laser propagates through the air, water absorbs parts of the spectrum, which looks just like a cavity reflection spectrum as shown in Fig. 3.8. These absorption lines by water could be mistaken for cavities with quality factors ranging from 10,000 to 50,000. The amount of absorption significantly depends on the length of the propagation, and more water lines appear with more propagation length. To overcome this, we mapped all observable waterlines in our system and discarded any absorption dips corresponding to those points.

Once the viability of this method for high-efficiency coupling into the waveguides was established, a telecom-sensitive camera was purchased for the characterization (Raptor photonics). This made the coupling significantly faster and easier. Once the above challenges were resolved, coupling to the cavity was found to be easier and faster than tapered fiber approaches. From the chip being in the storage box to the start of characterization can

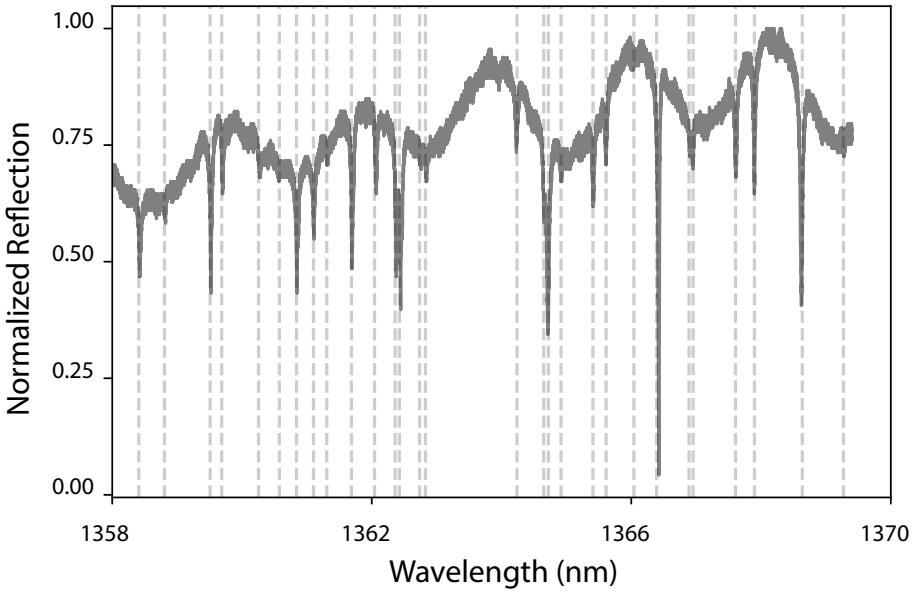

Figure 3.8: A cavity reflection spectrum for a cavity during the resonant at $\sim$ 1366.5 nm. The rest of the dips in the graph are from absorption by the water as the beam goes through the air. As the depth of the waterline is also a function of free-space laser propagation length, a combination of cavity outcoupling and characterization beam propagation length can make it challenging to differentiate the cavity from the waterlines. To avoid this we identified the waterlines observed in our system and is marked as dashed vertical lines. The cavity dip is horizontally offset from all dashed lines.

be achieved in under 2 minutes. And in most cases, slight adjustments of the stage in one direction are all that is required for characterizing a different cavity, much like grating coupler approaches. The approach presented here can also be extended to parallel coupling of multiple devices. This can be done by using the same technologies that are used for tweezer trapping, such as fiber arrays, AODs, or SLMs. Incorporating them would readily allow one to massively parallelize coupling in future photon extraction experiments, opening up the pathway for massive multiplexing. The Free space coupling introduced in this chapter is a general approach, and can be adapted to solid state systems in cryostats or trapped ion systems in a vacuum chamber. The long working distance coupling allows the reduction of overhead inside the vacuum or cryostat systems.

CHAPTER 4

FABRICATION

4.1 Introduction

In the previous chapter, we discussed the design constraints that are involved in the chip design to make it compatible with atom arrays and a scalable photonic coupling scheme. In this chapter, we cover the fabrication procedure to make a chip that satisfies all these constraints. For the chip presented in Chapter 5, part of the fabrication was done in Argonne National Lab (ANL). Specifically, the fabrication steps up to section 4.5 were carried out in ANL followed by the rest of the steps (till section 4.11) in Pritzker Nanofabrication Facility (PNF) at the University of Chicago. For the photonic chip presented in Chapter 7, the entire fabrication was performed at the PNF.

All the devices were fabricated on commercially bought silicon nitride (SiN) wafers. 330-nanometer silicon nitride on 500 μm silicon was bought from Silicon Valley microelectronics. The wafers were bought with half-dicing from the back side for easy breaking into individual chips of size 10 mm * 10 mm. The overview of the recipe is shown in Fig. 4.1, and involves the resist spinning (Fig. 4.1 b)), e-beam lithography to define the devices (Fig. 4.1 c)), pattern transfer to SiN using etching (Fig. 4.1 d), resist removal (Fig. 4.1 e), spinning photolithography resist (Fig. 4.1 f)), photolithography to mark the device region (Fig. 4.1 g)), dicing (Fig. 4.1 h)), and finally undercutting of the devices using wet etching (Fig. 4.1 i)). The detailed recipe for the fabrication is as follows:

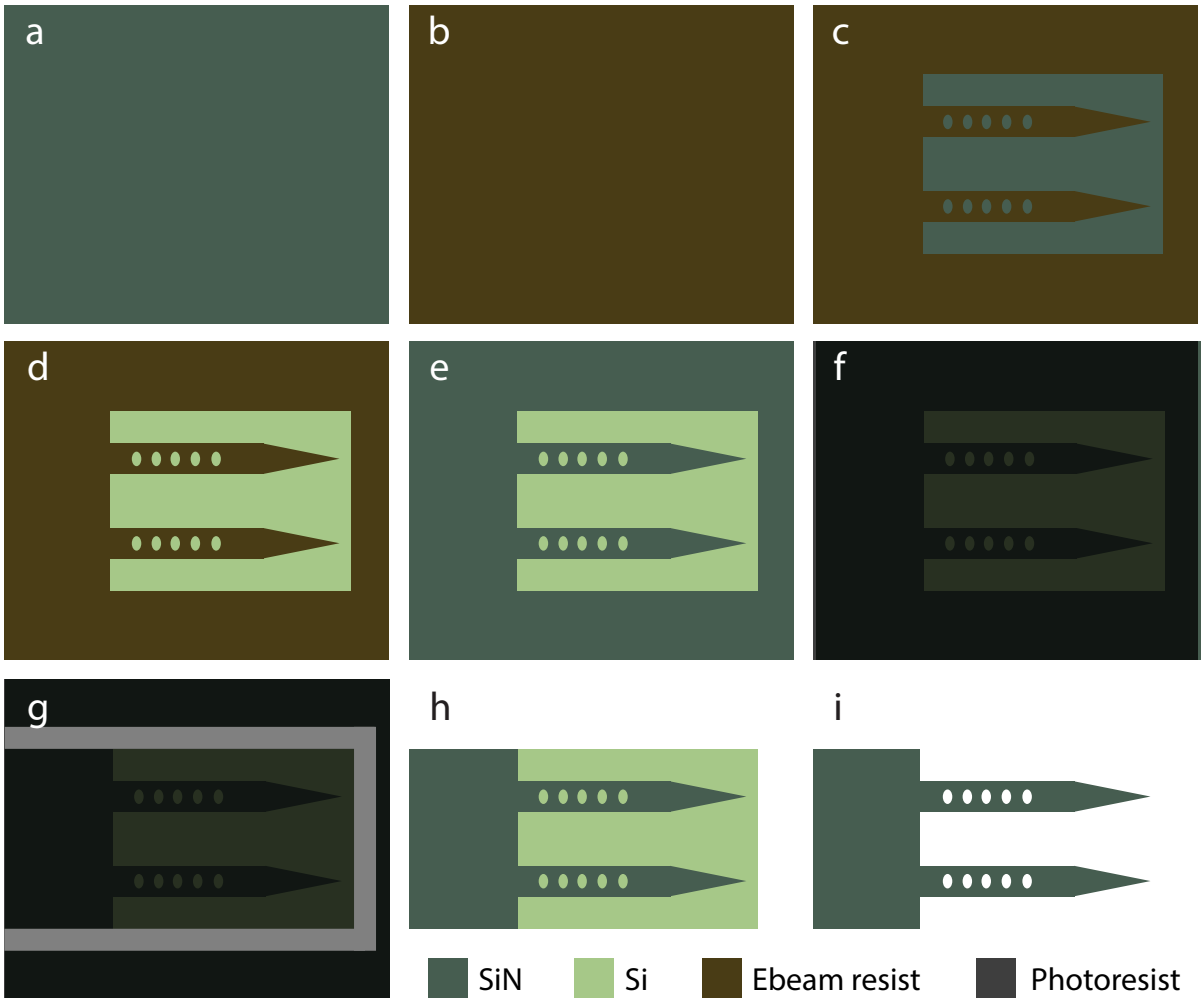

Figure 4.1: Cartoon of the fabrication procedure: a) We start from a commercially bought silicon nitride on silicon wafer. b) The sample is then coated with $\sim$ 400 nm of ZEP520A resist. c) Following this, the target design is patterned on the resist using ebeam lithography. d) The design is then transferred to silicon nitride using Fluorine etch, and the resist is then removed as shown in e). f) The sample is then coated with $\sim$ 12 microns of photolithography resist AZ P4620. g) Optical lithography is then used to define the device region that is compatible with our experimental geometry and etched using deep reactive ion etching. h) The device is then diced to separate out the target device region. i) Finally, silicon is removed from underneath silicon nitride.

4.2 Cleaning

Before separating the wafer into 10mm chips, the entire wafer was cleaned in hot nanostrip (bubbling) for 15 minutes. This was followed by 2 minutes in deionized water (DI), followed by water jet cleaning and nitrogen blow drying. The samples were then kept on a hot plate at 110 °C for 2 minutes.

4.3 Resist Spinning

This step is followed immediately after the cleaning to avoid any contamination. Before this step, the resist is taken out and kept for 1-2 hours to thermalize to room temperature. This helps to avoid water condensation when the bottle is opened and keeps the resist (ZEP520A) consistent. The wafer, right after the heating step in the cleaning process, is kept on a 4-inch chuck with good vacuum adhesion to the wafer and spun at 3500 rotations per minute (rpm) for 45 seconds. Following this, the wafer is kept at 180 °C for 2 minutes. This usually results in a resist thickness of around 405 nanometers.

In the initial rounds, ARP6200.13 stocked in the cleanroom was used. However, this seemed to have sticking issues and generally resulted in rougher sidewalls. Following this, a dedicated ZEP resist was used, which directly improved the sidewall roughness for the same parameters.

4.4 E-beam lithography and development

The pattern for the e-beam is made using the gdstk package in python. The pattern is then converted to a gpf file using the Beamer software. Proximity correction is done on all samples

to avoid pattern-dependent effects on e-beam. For this, different proximity error correction profiles for 330 nm silicon nitride on 500 μm silicon are first modeled using the software: Tracer. Following this, different models generated by Tracer with different z parameters are then experimentally swept to find the profile that gives the best proximity corrections. For e-beam, 10 mm chips are broken off from the wafer that was previously spun with the resist. Three to four devices are written in parallel to enable fast sweeping of different parameters. For writing the patterns, a beam current of 1.8 nA, with an aperture of 300 μm is used. For all the patterns, a 10 nm resolution is used in the writing along with 400 μC/cm^2 of dose. Different combinations of current and spot sizes ranging from 0.2 nA - 2 nA and 1 nm - 15 nm respectively were experimentally tried out before deciding to use the setting of 10 nm resolution and 1.8 nA current. This combination gave us the best quality factor for the devices. Different doses were also independently swept to optimize the quality factor before finalizing a dose at 400 μC/cm^2. Microscope image of a set of devices patterned onto the resist is shown in Fig. 4.2 a) and b).

Right after e-beam writing, the chips are developed in an Amyl Acetate solution for thirty seconds. This is followed by 30 seconds in IPA (Isopropyl Alcohol) and nitrogen blow dry.

4.5 Etching

After the development step, the samples are etched using an ICP (Inductively Coupled Plasma) fluorine etcher (Plasma-Therm ICP). We use a combination of C_4F_8, and SF_6 for the etching. For the etching of thick silicon nitride, ZEP is usually not preferred as its selectivity against silicon nitride in fluorine etch is not high. To find an optimal recipe

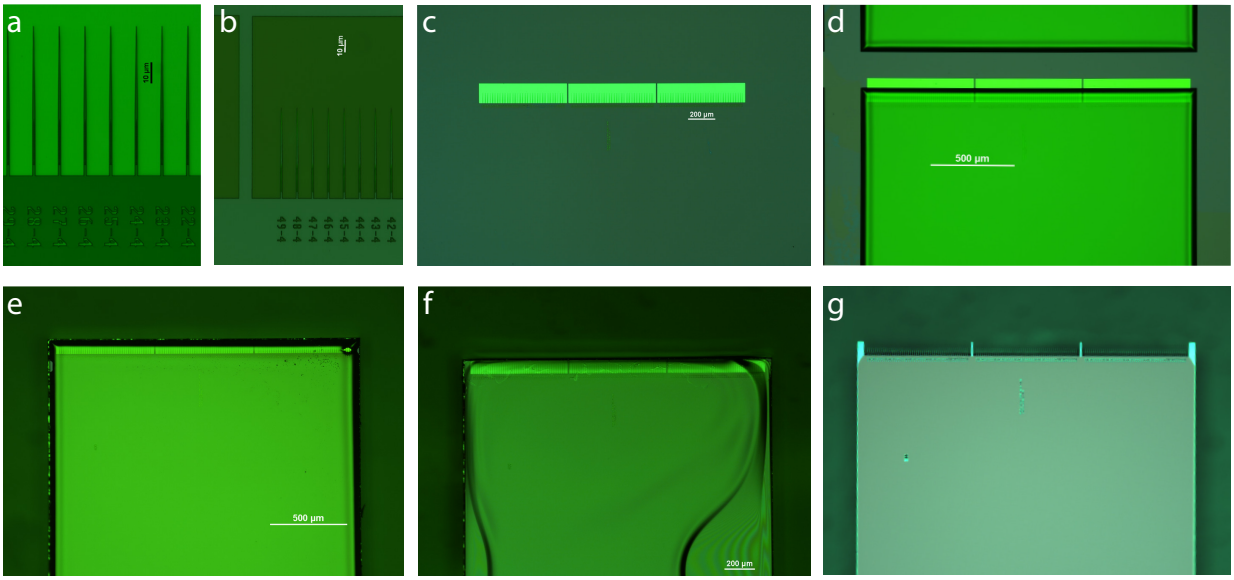

Figure 4.2: Full fabrication procedure: a) The nanophotonic cavities are initially patterned on ZEP resist, inside an underlying box as in b) for simplifying the steps that follow. c) The sample is then etched using a combination of C_4F_8 and SF_6 recipe. The three blocks represent batches of cavities made with three different mirror strengths. d) Following this, the required chip shape is patterned onto AZ P4620 photoresist and etched using deep silicon etching. e) The sample is then diced using the dicing saw. The chip geometry at this step is compatible with our requirements of having minimal impact on atom loading and imaging, and having the devices at the end of the chip. f) The chip is then coated with a layer of PMMA mask to protect the top surface from undergoing KOH etching. g) In the final KOH etching, the chip is only etched from the side, resulting in the complete undercut of the devices throughout the chip thickness.

with high selectivity against silicon nitride, each of the etch parameters was swept, and the corresponding etch rates were measured. A few of those are given below. The optimal etch parameters were initially determined using ARP resist, and the same was then translated to ZEP without any noticeable changes.

	ICP W	bias W	pressure mtorr	He sccm	SF6 sccm	C4F8 sccm	temp C	etch rate nm/min	SiN rate nm/min	Selectivity
test1	1000	6	15	5	12	12	15	34	19.8	0.58
test2	600	16	15	5	10	41	15	69.5	41	0.59
test4	100	10	15	5	50	14	15	4.1	3.75	0.91
test5	600	30	10	0	24	39	15	202	174	0.86
test6	600	11	15	5.5	12	28	15	59	75	1.27
test7	600	11	15	5.5	12	30	15	52.5	62	1.18
test8	600	11	15	5.5	12	32	15	33.5	47	1.4
test9	600	11	15	5.5	12	26	15	70	51	0.72
test10	600	11	15	5.5	12	24	15	68	73	1.07

Table 4.1: Set of experiments done to calibrate selectivity for different etch parameters. The experiments were done with CSAR ARP6200.13 resist. However, similar selectivity was also observed in ZEP.

Having only a small range of etch parameters with good selectivity is not great, as further etch parameter sweeps are necessary for good side wall angle and roughness. However, we were able to get good sidewall angles and roughness without any tweaks to the recipe with high selectivity. The etching is carried out by pasting the silicon nitride chip on a prime silicon wafer using silicon paste. The samples are etched for a total of six minutes and fifteen seconds, giving an over-etching of 8%. The over-etching is done to make sure all the holes, including the small Bloch taper holes, are etched throughout the sample thickness. Fig. 4.4 shows scanning electron microscope (SEM) images of the silicon nitride devices fabricated using the test 6 recipe given above. Devices were fabricated with a separation of 11 microns as shown in Fig. 4.4 a). Etch parameters along with the etch time make sure that the

holes are completely etched through, and that the sidewall angles are minimal, as shown in Fig. 4.4 b). In the initial rounds, the tapered end of the devices were attached to the chip for tapered fiber coupling as shown in Fig. 4.4 c); however, they were removed and the device edges were free-standing for free-space coupling fabrication rounds. Initial fabrication rounds also featured rough sidewalls as shown in Fig. 4.4 d), however, this was improved by optimizing the e-beam parameters and switching to ZEP resist. The final device have minimal roughness as seen in Fig. 4.4 b). The final etch parameters used are given below.

Property/name	**Value**
Time	6m:15s
Pressure	15 mtorr
Temperature	15 °C
SF6	12 sccm
C4F8	28 sccm
He	5.5 sccm
DC	11 W
ICP	600 W

Table 4.2: Silicon nitride Etch Parameters

An optical microscope image of the chip region after etching is shown in Fig. 4.2 c). The measured etch rates were sensitive to previous etch recipes that were run in the etcher. To avoid any cross contamination related etch rate variations, all the etchings were done in a second fluorine etcher, where the recipes are monitored and controlled. For further reproducibility of the etch rates, each etch round starts with an hour-long oxygen plasma cleaning, followed by fifteen minutes of conditioning. With this, we are able to achieve high repeatability in our etch rates. To confirm this, after each round of etching, the leftover resist thickness is measured in the region of the sample with no patterns. Corresponding etch rates of a few different runs are shown in Fig. 4.3.

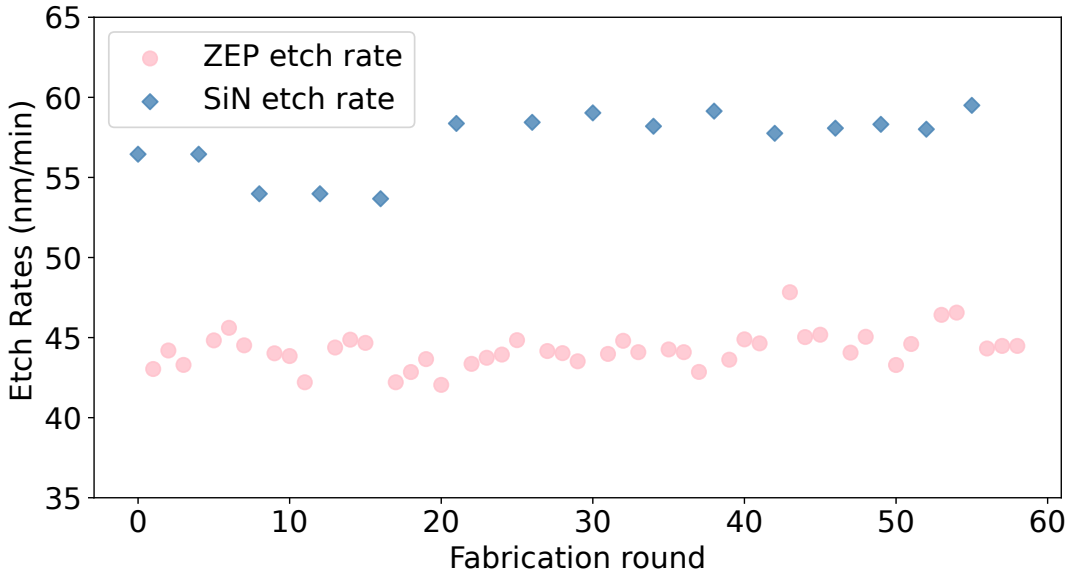

Figure 4.3: Etch rates were monitored for each chip based on the thickness of the resist before and after the etching. Simultaneously, a test silicon nitride was used before every few chips to separately tabulate the SiN etch rates. The values were measured using a Filmetrics F3 Film Thickness Spectral Reflectometer with ∼97% confidence.

In general, the etch rates of the resists are found to be stable within 3-4%. A random jump was observed in the etch rate of SiN that seemed to be uncorrelated with the measured rates on the resist (around fabrication round 20 as shown in Fig. 4.3). Given that the SiN etch rates were not completely correlated with the measured ZEP etch rates, the final etching is done for 6 minutes and 15 seconds, and is only recalibrated based on measured ZEP etch rates.

4.6 Resist stripping and photoresist spinning

Once the devices are etched into the silicon nitride, the next step is to define the chip region that we want to break off and keep inside the vacuum chamber. While the chip size is 10

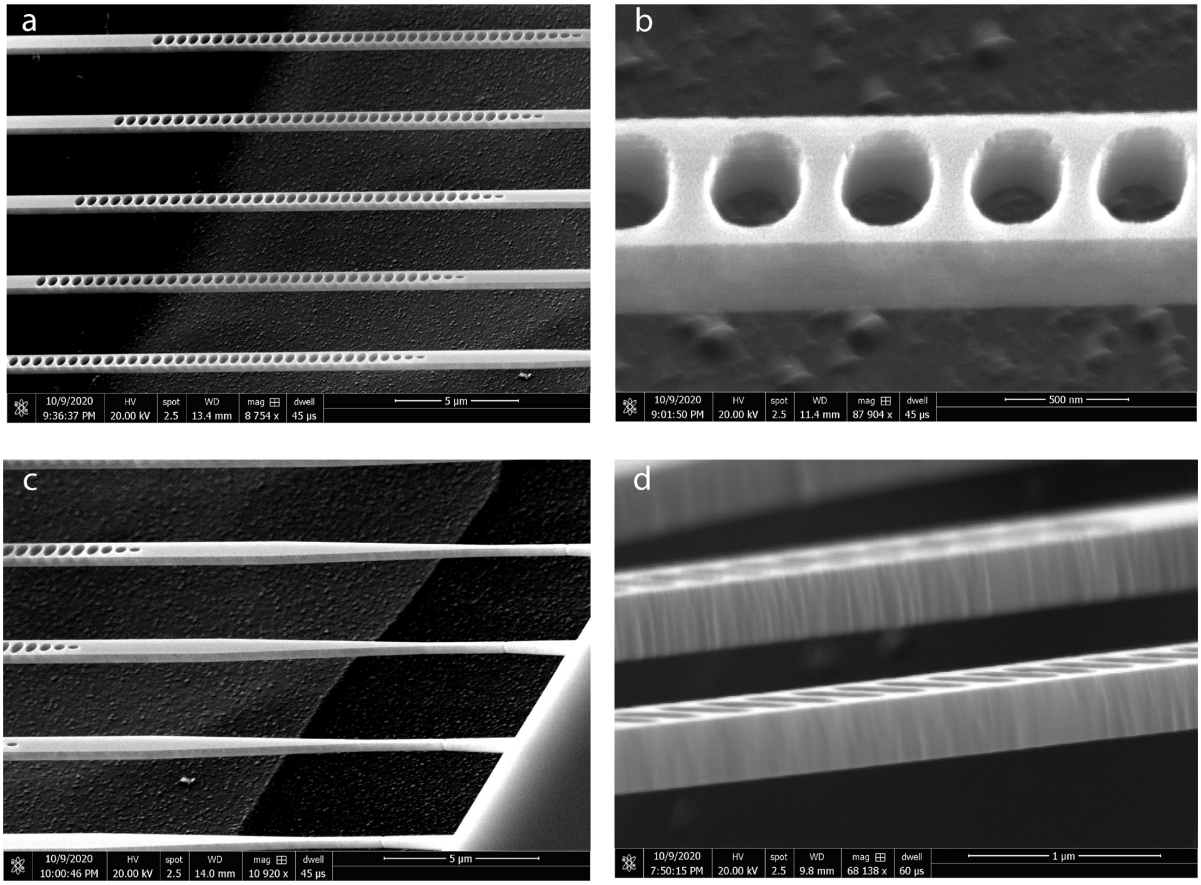

Figure 4.4: SEM images of some of the cavities fabricated during the recipe optimization process. These devices were fabricated using CSAR ARP6200.13 resist instead of the ZEP resist used for the final device fabrication. a) Shows an array of photonic cavities made by etching cylindrical holes onto a rectangular waveguide. b) Zoomed in image of the holes showing that holes have been etched through the thickness of the device. c) The waveguide width is tapered down for better mode matching. In the earlier fabrication rounds, tapered fibers were used for device characterizations instead of the free space coupling technique. For these initial rounds, the tapered edges were not freestanding and were clamped to the chip. d) The side profile of the devices shows reasonably smooth waveguide sidewalls. The profiles were further improved by improving the recipe and by switching to ZEP resist.

mm * 10 mm, the desired chip size to go inside the vacuum chamber is 2 mm * 7 mm. To do this demarcation of a smaller chip, we do photolithography. We start by removing the ZEP520A layer by placing the chips in 80C NMP (N-methyl-2-pyrrolidone) for 10 minutes. This is followed by 1 minute in IPA and 1 minute in De-Ionized water (DI). Finally, the sample is cleaned in a water jet and blow-dried using nitrogen.

Following the removal of the e-beam resist, photoresist AZ P4620, is then spun onto the sample. The resist is usually kept outside the fridge for $\sim$2 hours before the spinning to thermalize it to room temperature. The resist is spun at 1500 rpm for 45 seconds. Following this, the chip is kept on a hotplate at 110 °C for 3 minutes for soft-bake. Following the soft bake, the sample is kept at room temperature for 30 minutes for rehydration. In principle, the photoresist can be spun on top of the etched e-beam resist. This saves a resist strip process in between. However, resist sticking issues were observed when the photoresist was applied directly on top of the e-beam resist. This leads to imperfect resist layer formation and was not pursued.

4.7 Photolithography and development

A pattern marking the edges of a 2 mm * 7 mm chip is made and exposed on the chip. The design is aligned to the photonic devices based on the alignment markers made during the e-beam exposure. This step is done in the Heidelberg MLA 150, with a 405 nanometer laser and 700 mj/cm^2 exposure. A distance of 10 microns is left between the edges of the device and the chip edge to protect the device coupling edge from the dicing step.

Following this, the chip is developed in AZ 400K 1:4 developer for 9 minutes. From the

developer, the chip is then transferred to DI for two minutes and blow dried using nitrogen. Subsequently, the chip is hard-baked on a 110 °C hot plate for 3 minutes. An optical image of the chip after this step is shown in Fig. 4.2 d).

4.8 Deep etching and dicing

Once the chip layout is defined by the photolithography, the sample can technically be diced directly along those lines. However, dicing leads to rough edges, where tens of microns of additional chipping takes place along the dicing lines. Since our device coupling edges are close (∼10 microns) to the chip edge, direct dicing at this point can lead to damaged or broken edges. To overcome this, we do an intermediate deep reactive ion etching (DRIE). This step makes a trench along the chip demarcation line with a width of 210 microns and a depth of around ∼40 microns. Following the hard bake, a 20-minute break is given before the deep etching. Since the sample is hard-baked at 110 °C, lack of this thermalization time can lead to cracks on the resist layer during the etching process. These cracks can damage the device or significantly affect the final undercutting step. The chip is etched after sticking to a silicon wafer using silicon paste, and etched for 160 cycles with the standard double step deep silicon etch parameters used in the PNF cleanroom.

Once the etching is completed, the chips are removed from the wafer and diced along the trenches. The exact lines of dicing are carefully chosen to dice and remove substrate from as close to the device edges as possible, without damaging the edges. This helps in having a smoother substrate profile in the final undercut process. Fig. 4.2 e) shows the optical microscope image of the chip after the dicing step.

Name	Etch A	Etch B
Time	0:02.0 min	0:01.5 min
Pressure	25.0 mTorr	25.0 mTorr
C4F8	150 sccm	150 sccm
SF6	100 sccm	100 sccm
Ar	30 sccm	30 sccm
Bias	300 W	10 W
ICP	1000 W	1500 W

Table 4.3: Deep RIE etch parameters

4.9 Photoresist stripping and KOH mask resist spinning

Once the dicing is completed, the photoresist is removed from the chip by keeping the chip for an hour in 80 °C NMP solution. Some resist residues are observed after this step and are usually removed by sonication of the chip for five minutes.

Finally, we want to completely undercut the devices and overhang them from the edge of the chip for optical access. KOH (Potassium hydroxide) solution is one of the common undercut tools to remove silicon with good selectivity against silicon nitride. However, KOH etches in all crystal planes, albeit with different etch rates. In our samples, two silicon crystal planes are exposed to the KOH solution (<100> is exposed where SiN was removed in the etch step, and <010> is exposed from the dicing near the devices). Further, etching of the <100> plane will lead to the <111> plane being exposed, resulting in etching from three different planes. At this stage of the fabrication, direct etching of the chip in KOH solution will result in a slanted profile of the silicon substrate underneath the photonic cavities. This can lead to unwanted scattering of the tweezers, cooling, trapping, and imaging beams, which can potentially affect our atom/qubit operations. To overcome this we cover the silicon nitride surface of the chip with a mask to prevent KOH etching from the <100>

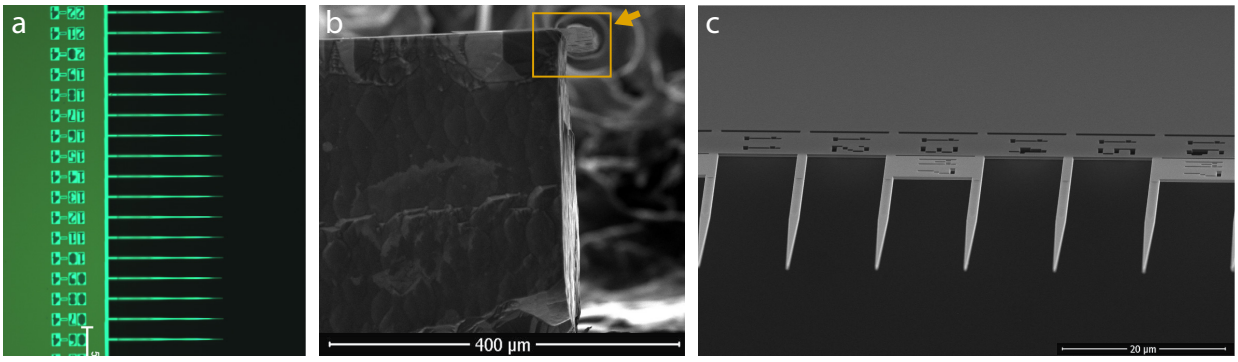

Figure 4.5: Chip profile at the end of KOH etching. a) A Microscope image of the devices at the end of the KOH etching. The color difference between SiN with and without underlying silicon can be noted. The devices are completely undercut, and some silicon is also removed from underneath the device labels. b) A scanning electron microscope (SEM) image of the chip after KOH undercut. The entire array of devices (in the box) can be seen undercut throughout the thickness of the chip. c) SEM image looking from the direction of the arrow in figure b).

direction, and to result in a directional etching in the <010> plane.

We use a double-layer polymethyl methacrylate (PMMA) as the etch mask for this step and start by placing the sample on a hot plate at 180 °C for five minutes to improve the resist sticking. Following this PMMA A4 is spin-coated onto the sample at 1500 rpm for 45 seconds. The sample is then soft-baked at 180 °C for five minutes, followed by another round of PMMA A7 spun and baked at 1500 rpm and 180 °C, respectively. Fig. 4.2 f) shows the chip after the bi-layer PMMA resist spinning. The small chip size and elongated shape make the resist layer have a non-uniform thickness across the chip. To avoid the resist sticking to the chip edge and prevent KOH etching in the <010> direction, the chip edge is gently wiped with cleanroom clothes soaked in acetone before the soft bake of both PMMA A4 and A7.

4.10 KOH etching

For the final undercutting step, the chips are kept in 80 °C KOH solution for 40-50 minutes. The optical and SEM images of the devices after the undercut are shown in Fig. 4.5. Fig. 4.5 a) shows the optical microscope image taken from above the devices. The small color difference shows the undercut region and the region with underlying silicon. This is clearer in Fig. 4.5 b) where the SEM image of the whole chip is shown from the side. The devices are marked in the box region. The substrate can be seen to be removed throughout the 500 μm thickness of the chip under the device. An SEM image from the direction of the arrow is shown in Fig. 4.5 c).

During the KOH etching, it has to be ensured that the KOH solution is at 80 °C using a base-resistant thermometer. Ideally, hot plates with feedback on the measured temperature of the KOH, or the water bath that KOH is kept in, would be the ideal way to do this. As KOH etch rates are a function of temperature, there is always a bit of uncertainty on the exact time it takes to etch the chip from the <010> direction and completely undercut the devices. Higher KOH etching time can lead to over-etching, and bowing of the silicon nitride, or even complete breaking of the device region. The etch was monitored every 15 minutes to make sure the chips are not over-etched. Since the size of the chip (2 mm * 7 mm) is small, the PMMA mask makes the chip float in the KOH solution. While this by itself is harmless, care must be taken for the chip to not crash, or fall on its device side. Following the KOH etching, the device is then cleaned twice in 80 C DI, each for five minutes, to remove the KOH residues on the chip.

4.11 Cleaning

After the undercut, the samples are cleaned in the nanostrip for 20 minutes, followed by water jet cleaning and nitrogen blow dry. The cleaning is done in a hot nanostrip while it is bubbling. Directly taking samples out of such a hot nanostrip or piranha can lead to contaminants being deposited onto the chip from the tweezer. To avoid this, the sample is cleaned in a bubbling nanostrip solution for 10 minutes, followed by moving the nanostrip onto a non-heated surface for another 10 minutes of cleaning.

After the KOH etching, the devices overhang from the edge of the chip and are extremely prone to breaking. These are some common things that have led to devices breaking. 1) Device falling down, 2) water bubbles during post-KOH cleaning flipping the chip and breaking the devices, 3) surface tension causing devices to climb up the tweezers while holding, 4) chips flipping in the carrier box, and 5) high-pressure water jet directly onto the devices. The optical image of the chip after this final step is shown in Fig. 4.2 g). The devices can be seen undercut on the top edge of the chip.

One consideration during the fabrication process was whether the water surface tension was large enough to break the devices. However, it was seen not to be the case, and there was no need for critical point drying.

4.12 Future improvements

There are a few different avenues where the fabrication process can be made more reliable and faster. In the fab process, one of the key parts is reducing the chip sizes to 2 mm*7 mm.

For this we use a dicing saw. However, since the dicing saw is very coarse, we have to do a deep silicon etch before that step. Alternatively, if we have a precision cleaver instead of a dicing saw, the deep RIE step can be avoided. This would also reduce NMP-based resist removal time, making the process more efficient.

In the fabrication process, having a holder for the chip from KOH to the end can avoid few different challenges. It can avoid chips flipping during KOH/DI/Piranha steps. It can also reduce chip handling with tweezers where surface tension can sometimes cause challenges. Since during KOH etch, the sample has to be taken out of KOH, DI cleaned, dried, and taken to the microscope station for etch verification, having such a reliable holder can reduce the chances of events that may lead to breaking of the devices.

In the etching, there is always an unreliability coming from the fact that we are using two chemicals for etching. While SF_6 does the direct anisotropic etching in the thickness direction, the quantity of C_4F_8 significantly affects the sidewall profile and effective radius of the holes. While both of them are necessary for the resonances and quality factor, in our etch rate measurements above, we are only monitoring the direct effect of SF_6. This results in some uncertainty and variations in the resonance frequency despite having the same etch rates. Moving to single compound etching such as CHF_3 might be an effective way to overcome this challenge.

CHAPTER 5

ATOM-ARRAY-PHOTONIC CHIP PLATFORM

5.1 Introduction

In the previous chapters, we demonstrated a compact chamber design for atom-array operations. To overcome potential MOT loading challenges, we introduced a chip design that minimizes the overlap with the MOT beams while maintaining the cavity access. While this design minimizes the effect on the MOT and enables atom loading next to the dielectric surfaces, it introduces a significant challenge for fluorescence imaging, a standard technique for atom presence and state detection in atom array experiments. However, in the vicinity of large materials, including dielectrics, this becomes quite challenging since the dielectric, and the features on them, scatter light beams used for imaging. These reflections are, in general, frequency-independent (depending on the incident beam frequency and the dielectric absorption coefficient at those wavelengths) and can drown out the atomic signals as background noise. Furthermore, the presence of materials can cause arbitrary reflections that can affect the effective Rabi frequencies of the addressing beams.

This chapter will cover how we overcome these challenges and integrate the dielectric chip with atom arrays. We will discuss how we image the atom array system, and show that the atom array characteristics are unaffected by the presence of the chip platform tens of microns nearby. Additionally, we will explore novel capabilities enabled by our unique imaging scheme. Finally, we present how we can move atoms from these atom-arrays and position them onto our photonic devices of interest, where ∼GHz level atom-cavity interaction

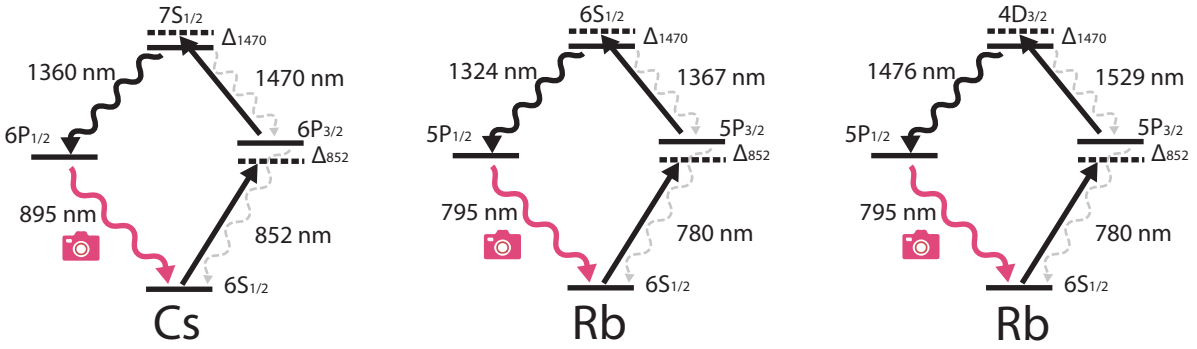

Figure 5.1: Few different ways the imaging can be done in Cs and Rb atoms. For Cs the imaging is done at 895 nm, while the excitations are at 852 nm and 1470 nm. For Rb, the imaging is done at 795 nm, while the excitation could be a combination of 780 nm, 1367 nm or 1529 nm. Here, imaging is done in the near-IR regime, but this is not a requirement. Similar level schemes can also be found for atoms like Ytterbium and Strontium.

strengths are expected.

5.2 Excited state imaging

To overcome the scattering of imaging beams from nearby dielectrics, a few different approaches have been made. For small, singular structures with symmetries, this could be relatively straightforward and can be mitigated using filtering in the image and Fourier planes [198]. For slightly more complicated singular structures, confocal microscopy has been used to overcome this [162]. To image multiple atoms next to a photonic chip, a combination of input beam polarization, incidence-angle control, and filtering of the image beam have been used [196]. In this work we want to image an array of atoms, and we want this to be independent of underlying symmetry, size, or the number of structures present. This allows multiple types of devices to be combined in the same chip system, independent of their geometry. These devices can then be of different types, including cavities, waveguides,

microwave strips, 2-d structures, and so on. We achieve this using an excited-state imaging scheme, where we image our atoms using unconventional, non-cycling atomic levels.

In our scheme, we excite the atom using a conventional imaging/cooling beam, but then add another excitation leg that excites the atom from that intermediate level ($6P_{3/2}$) to a second excited state ($7S_{1/2}$). The key idea here is that from this second excited state ($7S_{1/2}$), there is an alternate decay channel whereby the atom decays to a different intermediate level ($6P_{1/2}$) before returning to the ground state. The key atomic levels included in the scheme are shown in Fig. 5.1, and the same scheme can be extended to other atomic species. We add an excited-state transition along with our cycler transition to drive a two-photon transition to a doubly excited state and collect the fluorescence when atoms decay through different intermediate states. For cesium (Cs) atom, the excited state we use is the 7S state, and for rubidium (Rb) atom, it could be the 6S or 4D states as shown in Fig. 5.1.

This scheme allows us to filter out scattering of the excitation beam generated by the dielectrics as the fluorescence and the excitation wavelengths are well separated. Atoms imaged through this scheme are shown in Fig. 5.2 a) along with a typical photon collection histogram in Fig. 5.2 b) showing greater than 99% fidelity in estimating the presence and absence of the atom. The dependence of the detunings of both excitation lasers on the total detected fluorescence is shown in Fig. 5.2 c). The 852 nm laser detuning on the x-axis is measured with respect to the bare $6S_{1/2}$ F = 4 $\rightarrow$ $6P_{3/2}$ F = 5 transition and the 1470 nm laser detuning on the y-axis is measured with respect to the bare $6P_3/2$ F =5 $\rightarrow$ $7S_{1/2}$ F = 4 transition. The detected signal falls off as the 852 nm detuning approaches the $6S_{1/2}$ F = 4 $\rightarrow$ $6P_{3/2}$ F = 5 transition on the right side of the plot and when it approaches the $6S_{1/2}$

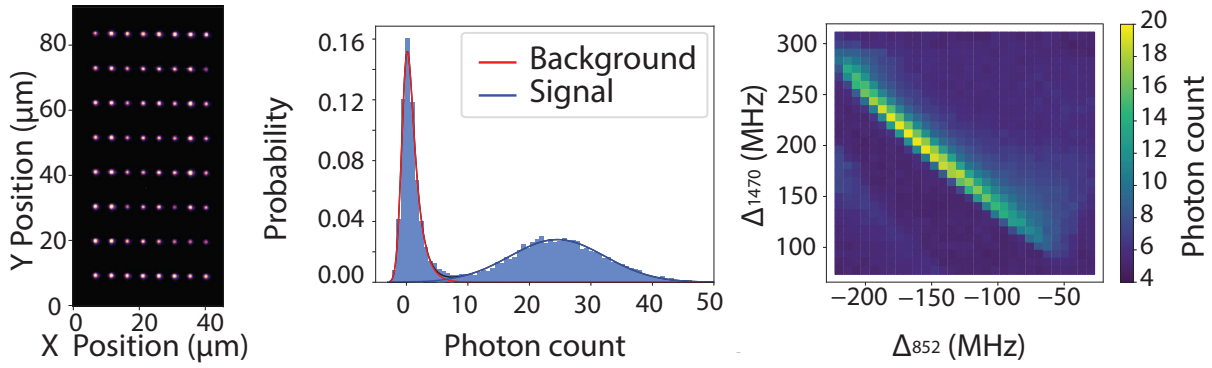

Figure 5.2: a) Fluorescence image of atoms generated through our multi-chromatic imaging scheme. b) A typical histogram of the detected 895 nm photons within a 4x4 pixel region of interest with 40 ms exposure time. From fits to the distribution, we can distinguish between the presence and absence of an atom with high fidelity $\geq 99.2\%$. c) Average magnitude of the fluorescence signal as a function of excitation laser detunings.

$F = 4 \rightarrow 6P_{3/2}$ F = 4 transition (-251 MHz on the x-axis) on the left side of the plot. We attribute this to atom loss from the tweezer as a result of resonant heating. The optimal point is far from a ground state resonance, where there is an optimum between cycling on the lower transition vs the two-photon excitation. The overall feature is blue-shifted from the bare two-photon resonance by tens of MHz due to the AC Stark shift from the tweezer.

From the histograms in Fig. 5.2, a fidelity $> 99\%$ is calculated based on the overlap of the two fit curves. In this case, the background is mostly limited by the EMCCD (Electron-Multiplying Charge-Coupled Device) noise, and is fitted to an exponentially modified Gaussian, whereas the atomic signal is fitted to a Gaussian. Our typical atom survival probability averaged over all atoms in the array after a 40 ms exposure is between 80-85%. Some of the atoms in the arrays show ~90-93% survival after the imaging for certain parameters, indicating that the overall survival probabilities can be improved after better homogenization of our tweezer arrays. Improving from the low 90s to greater than 99% is possible with additional considerations. Typically, imaging of atom arrays is done through closed cycling transitions

that also cool the atoms. However, in our scheme, the imaging is not done through a closed cooling/cycling transition. This could potentially heat the atoms. However, the first leg of the excitation is cooling, and the ratio of power, frequency of this cycling beam, and the excitation beam can be tuned to optimize the cooling vs imaging of the atoms. Further, the excited levels $7S_{1/2}$ and $6P_{1/2}$ are anti-trapped in our tweezers, adding to the probability of atoms leaving the tweezer trap. The loss from the anitraped excited states can be mitigated by imaging the atoms while they are not trapped in the tweezers. This can be achieved by a stroboscopic method where the trapping and imaging are done at a high frequency with temporally alternating beams [230].

5.3 Atom array next to photonic chips

The background-free imaging technique presented above is insensitive to scattering of the excitation beams by the photonic chip, as collection wavelength and excitation wavelengths are far separated, and can be filtered out through commercially available band filters. This readily lets us collect the fluorescence of the photons emitted by the atom without being washed out by the device scattering. To demonstrate this capability, in Fig. 5.3 a) top we show the image of atoms tens of microns close to the devices using the standard D2 fluorescence imaging technique. While there is significant scattering on top of the devices, what is particularly challenging for atom array incorporation is the fact that there seems to be significant background scattering in the region away from the photonic chip where there is no particular scatterer. This arises due to scattering by the chip at different angles, and depths. In the figure, an atom array is located at the region corresponding to 60 μm label

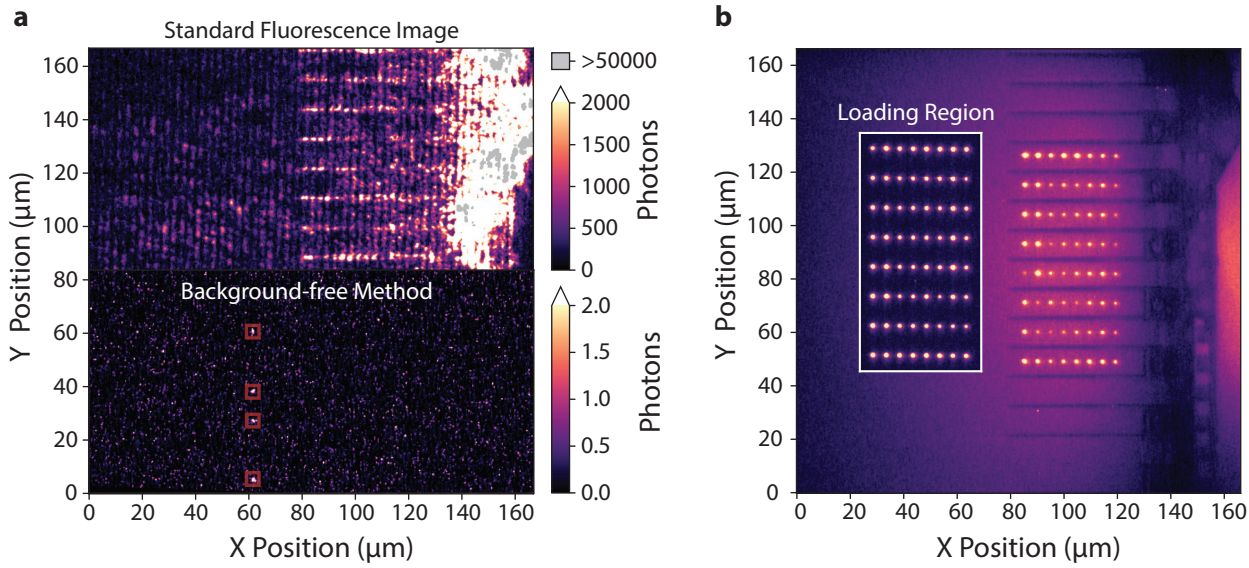

Figure 5.3: a) Top: Fluorescence image using the standard 852 nm (D2) cycling transition near our nanophotonic chip. Despite lowering the electron multiplying gain (EM gain) process on our camera to 10 from our typical value of 1000, the image is still saturated at the single atom scale, even tens of microns away from the devices. Bottom: A single-shot image of atoms (inside the red boxes) taken using the background-free technique developed in this work. Here, both images are taken with a 40 ms exposure time. b) An averaged fluorescence image of the atom array interleaved between the nanophotonic device array. No post-processing has been applied here beyond averaging the individual images. A small residual background makes the devices appear as dark shadows. We attribute this background to fluorescence at our imaging wavelength from the silicon base layer of the nanophotonic chip. The inset shows an averaged fluorescence image of an 8 x 8 atom array in the loading region.

on the x-axis. However, all the atomic fluorescence signals are washed out by the device scattering. In Fig. 5.3 a) bottom, we show that the same atom array imaged using our background-free method, where the atoms are clearly visible in a single shot of the image. This capability is the key enabling feature that allows us to combine atom arrays next to the photonic chips. Fig. 5.3 b) shows atoms loaded in the loading region and moved in between the devices before being imaged.

In an array of atoms, the histograms corresponding to different tweezers can be optimal at different excitation beam power/frequencies due to non-uniformity in the tweezers. This

non-uniformity can arise from different optical aberrations, objective field of view related limitations, or from the addition of different sinusoidal functions that form the tweezer arrays. We compensate for this by optimizing the amplitude corresponding to each tweezer while generating the RF tones. In general, the imaging histograms can be made uniform across the array either by individually balancing the tweezer power based on the detected histogram or by measuring the trap frequencies of each atom and adjusting the trap power to have uniform trap frequencies. We use the trap frequencies as the metric to generate a uniform array of atoms.

Another important metric for atoms in tweezers is their temperature. Larger atomic temperatures can lead to atoms exploring a mixture of thermal levels and exploring more trap potential. Further, starting atomic temperature can also play a key role in the atom's survival in the tweezer. To understand the typical temperature of atoms loaded onto the tweezers, we measure their temperature by turning off the tweezers and looking at the recapturing probability of the atoms. Following the polarization gradient cooling step, we typically have 50-55% loading of atoms in our array. We then turn off the tweezer and turn it on after a few microseconds and measure the atom survival probability as shown in Fig. 5.4 a). The survival of the atom in the trap is a function of the atomic temperature, and we use Monte Carlo simulation to model the atom loss. From the atom survival curve, we model the atomic temperature to be 50 μK at a trap depth of 0.8 mK. For the experiments in this chapter, we used tweezers with a beam waist of 1.1 μm with individual tweezer power of 3 mW.

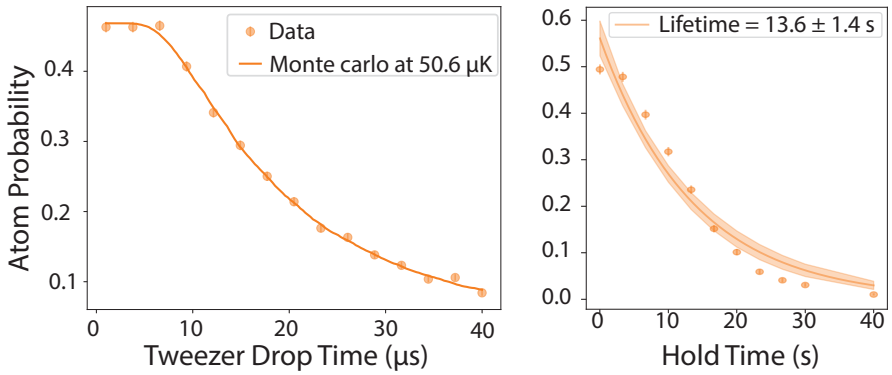

Figure 5.4: a) Probability of recapturing the atom in tweezer after turning off the tweezer for a finite time. The solid line is the temperature estimate based on Monte-carlo simulations. b) Atomic lifetime based on atom survival after finite hold time. Solid line is an exponential fit to the data.

Similarly, we measure the atom-lifetime by holding the atoms in the tweezer for a finite amount of time before detecting them using our imaging scheme. The probability for the atoms to survive after a finite hold time is shown in Fig. 5.4 b). Ideally, imaging the atoms in the beginning to confirm their presence and doing a second measurement after a finite hold time would avoid the uncertainty of which atom was not loaded as opposed to which atom was loaded and then lost during the hold time. However, since we have losses from our imaging, and given our imaging is also adding to the heating of the atom, we avoid this and just do one image acquisition at the end of the hold time. From the average atom survival, we extract the atom lifetime in the tweezers to be around 13 seconds. This exponential decay of the atom survival probability is consistent with background gas collision limited lifetime. This lifetime is measured tens of microns away from the chip. The additional mounting structure and clamps placed inside the chamber to mount the chip contribute

to the reduction in the atomic lifetime. Additionally, having the chip at the center of the chamber causes significant blocking of the MOT beams, and the resultant MOT was not visually visible at the same dispenser current used in Fig. 2.4. This contrasts our MOT loading before the placement of the chip and the mounting structure inside the chamber, where, at the same dispenser current, we found more than 10 million atoms in the MOT. To compensate for this, we operated the dispenser at half an ampere higher (3.7 Amps) than our set point for the 60-second lifetime data in Fig. 2.4. This additional influx of cesium in the MOT region also makes a significant contribution to the reduced lifetime.

5.4 Loading onto the pancakes

Once the atom arrays can be operated next to a photonic chip, the subsequent question is whether we can load the atoms onto the photonic chips where they can interact with the cavity modes of interest. For this, we have to make sure the atoms and the devices are on the same focal plane. Further, we want the capability to deterministically move the atomic plane with respect to the device plane to optimize the loading of atoms close to the devices. In free-space atom array experiments, atoms are routinely trapped in tweezers. The cross-section of a typical tweezer generated from a 0.6 NA objective is shown in Fig. 5.5 a). However, when an optical tweezer is brought on top of the photonic chip the tweezer is reflected from the top and bottom side of the device, resulting in a standing-wave like potential as shown in Fig. 5.5 b). The intensity maxima of these standing waves are separated by $\sim \lambda/4$, and atoms can be trapped in multiple of these potentials based on the tweezer power and the atomic temperature. However, as explained in the next chapter, the evanescent

field of the cavity decays exponentially with distance from its surface. For strong atom-cavity interactions, we want the atoms to be sitting on the intensity maxima closest to the photonic device surface.

This can be achieved by optimizing the tweezer plane with respect to the photonic device. Using this approach $> 90\%$ efficiency has been achieved in moving atoms deterministically to the first intensity maxima (also referred to as the first pancake) [162]. We use Monte-Carlo simulations to understand the optimal loading trajectories of atoms that leads to the occupation of the first intensity maxima. The corresponding loading trajectories of 10 atoms initialized in the tweezer with random positions and velocities are shown in Fig. 5.5 c). For the device thickness of 330 nm used in our experiment, the atoms in tweezers experience a discontinuity in the potential while moving from free space to the device. This discontinuity prevents adiabatic transfer of atoms to the first pancake. Here, the trajectory is evolved within a moving optical tweezer, characterized by a depth of 1.2 mK and a constant speed of 0.02 μm/μs. However, this discontinuity can be overcome with multiple approaches. In Fig. 5.5 d), we show that some of the atoms are able to overcome this barrier when initialized with temperatures in the range of 50-70 μK. We see up to 40% loading efficiency into the first pancake depending on the starting depth of the tweezers. Since atomic temperature measured in our system are in this range, we expect similar loading efficiencies to the first pancake. Further, we also note that fast movement of tweezers can also achieve similar results and allow some atoms to overcome the potential barrier. This is shown in Fig. 5.5 e) where some of the atoms are able to overcome the barrier when the tweezer was moving at a speed of ~ 0.1 μm/μs. For all the Monte Carlo trajectory simulations, a tweezer depth

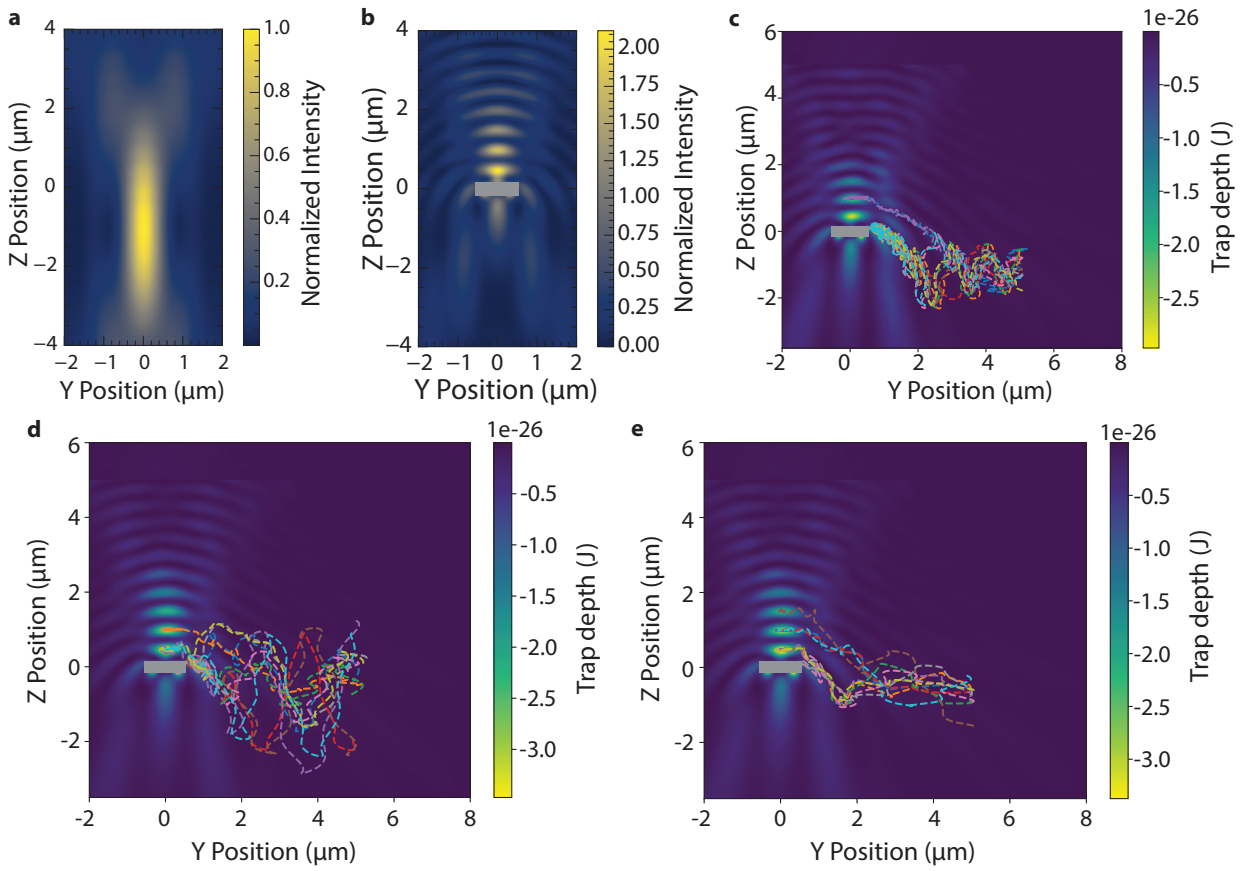

Figure 5.5: a) The tweezer trap potential is free space. b) The trap potential is modified on top of the photonic device as the incident tweezer interfere with the reflected tweezer. c) Monete carlo simulation of trajectories of atoms traveling from free-space to on top of the devices. Atoms that are on path to the first pancake ends up crashing to the device due to discontinuity in trap potential. Here, atomic temperature is 10 μK and tweezer is moved at a speed of 0.02 μK/μs. d) If atoms are initialized in the traps at higher temperature (60μK), some of the atoms are able to overcome the barrier and reach the first pancake. e) Atoms can also reach the first pancake even if they are initialized at lower temperature, but tweezers are moved non-adiabatically.

of 1.2 mK is assumed.

Given the importance of finding the right z-plane for tweezers to optimally load onto the first pancake, experimentally we need a way to position our microscope objective with respect to the devices. General room temperature variations, as well as the temperature changes caused by MOT coil switching on and off cause our objective to change its position by microns. However, given the thickness of the device is around 300 nm, it is necessary to have the positioning capability of the objective to be comparable (or comparable to $\lambda/4$). Further, we want them to be stable at that point of interest. For optimal objective positioning, we want a metric that can be fed into our experimental control system for routine checks and adjustment. We do this by taking a picture of the device using the objective and taking its laplacian to convert the image to a number. A Laplacian curve generated as the objectives move closer to the devices is shown in Fig. 5.6 a). Although this worked as a good indicator, we found this metric to be noisy and less precise than our requirement. To reduce the noise on the contrast curve, we filter the image using a bilateral filter before we take the Laplacian. The bilateral filter helps reduce the noise while maintaining the edge information allowing us to reduce the noise in the Laplacian and also to narrow down our positioning capability. Similarly, to reduce the width of the laplacian curve, we find an optimal region of our chip (in our case, the edge of the devices as shown in Fig. 5.6 b)), where we found the curve to be the narrowest. Combined with both of these capabilities, we achieve positioning sensitivity with precision less than $\sim$100 nanometers on the rising and falling edge of the curve. The Laplacian curve for the image in Fig. 5.6 b) is shown in c), demonstrating the possible precision in tweezer positioning.

Finally, we need to understand the correlation between the Laplacian score curve and the optimal loading onto the target pancake. For this, we load an array of atoms in the loading region tens of microns away from the photonic chip and move them onto the devices in parallel. This measurement is sensitive to the relative plane of the tweezer and the device. When the tweezer plane is far above the device plane, moving to the device and back has relatively no effect. On the other end, when the tweezer plane is below the device, atoms in the tweezers are lost during this move. The boundary between these two regimes positions the tweezers for optimal loading onto the first pancake. Further, due to our thickness, the efficiency of loading to the first pancake is 30-40% at the optimal positions. This experiment also allows us to explore these regimes. Fig. 5.6 d) shows an array of eight atoms from the loading zone moved to different "row offsets" and brought back to the loading zone after 40 ms to check the survival probability. Here, "row offset" is a parameter that maps device positions to AOD frequencies, with devices being centered at a row offset of zero. The atoms are brought to the devices from negative row offset frequencies. On the device edges (regions close to zero), the tweezer trap is leaky, and parking the tweezer here leads to atom loss. However, the atoms can survive on top of the devices (row offset =0) for the 40 ms waiting time. For the positive row offset, the atom survival probability corresponds to the atoms surviving the first move across the device to the positive row offset value, staying in the tweezer for 40 ms, and moving back to the loading zone by crossing the device for a second time. Given the finite angle present in our photonic chip with respect to the objective angle (positioned to correct for the glass angle), we also see that we have a gradient in the optimal z-plane for different atoms in the array.

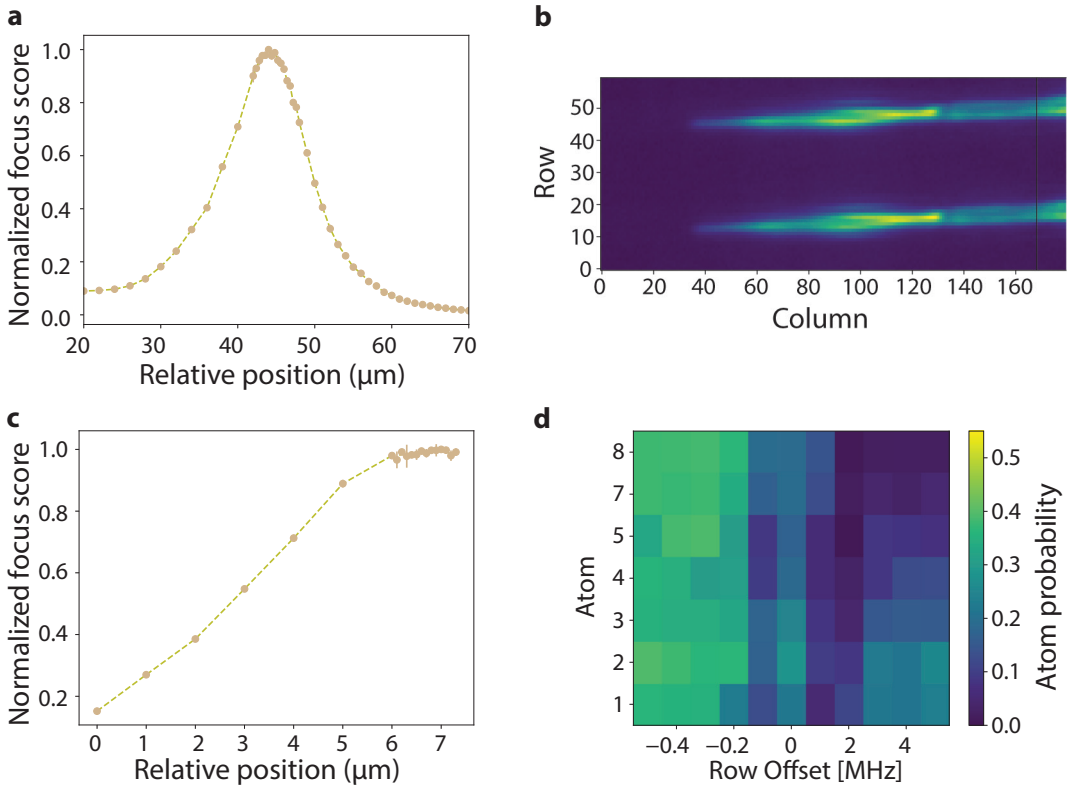

Figure 5.6: a) Estimated focal score as the tweezer objective moves closer to the chip from an arbitrary starting point. b) The region of the chip used for the focal score calculation. A bilateral filter is applied to the image for noise reduction. Focal score is calculated by taking Laplacian of this image. c) Optimized focal score curve with careful device region selection and bilateral filter. The error bars in the rising region of the graph is smaller than the marker size and correspond to ~ 100 nm precision in objective positioning. d) The survival probability of atoms when eight different tweezers are taken across eight different devices. Here, zero on the Row Offset axis corresponds to the calibrated center of the devices. When taken across the device (positive row offset), the probability of atoms traversing back to the loading zone is a function of the corresponding pancake's loading probabilities. A small angle between the device plane and the atom array plane results in different survival probabilities across the array as different atoms are loaded onto different pancakes.

Although these measurements are indicative of the atomic position in desired pancakes, they are not conclusive evidence of the same. One approach to understand the atomic position would be to take advantage of the different Stark shifts atoms experience in the pancakes. Since the pancakes on top of the photonic devices have different intensities, they will have corresponding different light shifts. This measurement can be done in a manner very similar to the previous one, where we load the atoms, move them onto the device, do a light-shift sensitive blowout measurement, and move atoms back and image them. However, a surprise benefit of our imaging scheme was the ability to image atoms when trapped on top of the photonic devices. Given the imaging time of tens of milliseconds combined with modified trap potential on top of the photonic devices, the ability to image the atoms on top of these devices is not an obvious outcome. For this to succeed, the atomic lifetime on top of the photonic devices has to be larger than the imaging time, the atoms should not be significantly heated during the transport to the device, and the atoms have to survive in the modified trap potential while being imaged.

In Fig. 5.7 a), we show an averaged image of atoms trapped on top of the photonic devices. The images are taken with a 40 ms exposure time. A typical single-atom imaging histogram while atoms are trapped on top of the device is shown in Fig. 5.7 b). Here, the fidelity of detection is estimated to be 86% with a threshold of 5 photons. While the background is comparable to that of atoms in the loading region, the atomic signal is shifted to lower photon numbers. This is due to an increased atomic loss during the imaging due to the modified trapping potential. This can be further optimized in future experiments by optimizing the

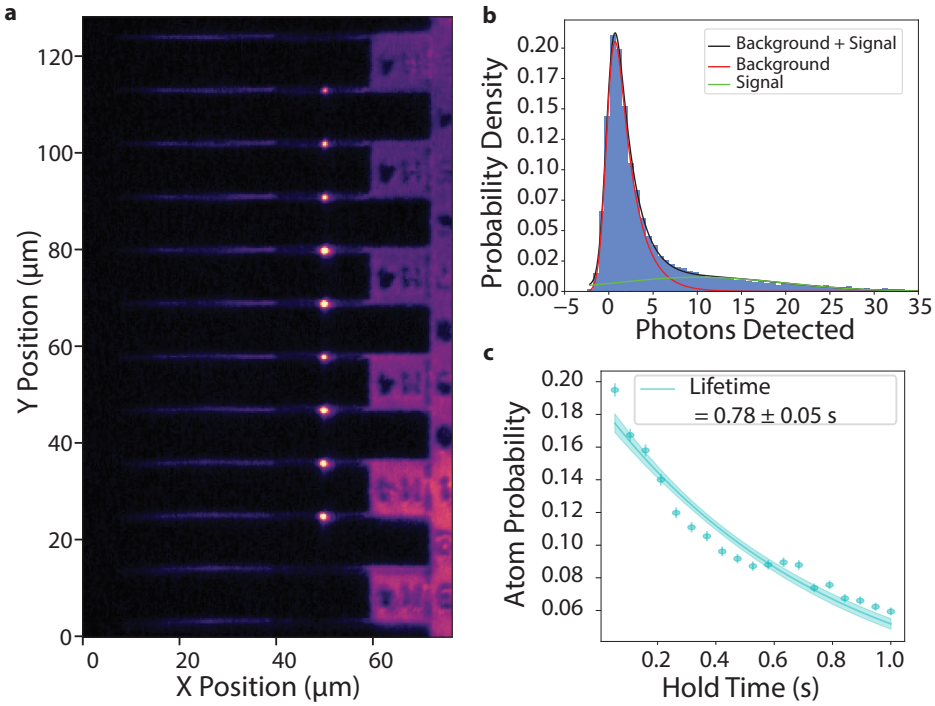

Figure 5.7: a) Averaged image of atoms trapped on top of the photonic chip, b) A typical single-atom imaging histogram while atoms are trapped on top of the devices. Here the fidelity of detection is estimated to be 86% with a threshold of 5 photons. c) Atom survival in the tweezer as a function of holding time trapped on top of the devices. Atoms are relatively long-lived even on top of the devices with lifetimes of individual atoms varying from 0.7 to 1 second.

tweezer power, the power, and the detunings of the imaging laser. Additional methods such as employing Raman sideband cooling to achieve lower atomic temperatures or imaging with lower drive power for longer timescales as in [198] can improve this measurement. The corresponding lifetime measurement of the atom trapped on top of the photonic device is shown in Fig. 5.7 c), and from the fits, we estimate an atomic lifetime of 0.78 seconds. Reduction in the atomic lifetime in these standing wave traps is consistent with the earlier observations of atoms trapped on top of nanophotonic devices [167], and is expected from thermally excited phononic modes of the devices[231]. However, this lifetime is sufficiently large compared to observed coherence times on top of the devices of $\sim$ 2 ms[168], atom rearrangement times of $\sim$100 μs, and the required atom-cavity interaction time for entangled photon generation $\sim$100 ns [205].

Given the ability to image atoms on the trap, to determine the pancake the atoms are loaded to, we probe the AC Stark shift experienced by the atom. Our tweezer wavelength of $\lambda = 935$ nm is magic for the $6S_{1/2} \rightarrow 6P_{3/2}$ transition, meaning that the Stark shifts induced on the $6S_{1/2}$ and $6P_{3/2}$ levels are equal in both sign and magnitude, rendering it insensitive to the intensity variation between the trapping potentials. The $6P_{3/2} \rightarrow 7S_{1/2}$ transition is not magic to this tweezer wavelength and experiences different Stark shifts in different pancakes. This allows the ideal two-photon imaging frequency to be a proxy for assessing the pancakes we are loading the atoms into. However, this is not an ideal proxy as the intensities of the beams had spatial modulation due to the photonic devices that also affected the imaging (see Appendix). Given this, we measure the Stark shifts on the $6S_{1/2}$ $\mathrm{F} = 3 \rightarrow 6P_{1/2}$ $\mathrm{F} = 4$ (D1) transition at 895 nm and compare it to the Stark shift the atom

experiences in the free space tweezer.

We begin this Stark shift measurement by loading the tweezers with atoms in the loading region, moving the tweezers between the devices, and then moving the tweezers onto the devices from the side. We then apply a variable frequency 895 nm laser pulse in order to blow out the atoms from the tweezer when the pulse is resonant with the Stark-shifted atomic transition. Finally, we image the atoms to detect the survival rate. In Fig. 5.8 b), we show typical blow-out survival curves showing the increased Stark shift when the atoms are loaded onto the devices. In Fig. 5.8 c), we plot the fitted centers of the blow-out survival curves as we move the atoms across the device region, showing that the observed increase in the Stark shift only occurs when atoms are directly on top of the devices where they are trapped in the higher intensity standing wave potential shown in Fig. 5.8 a). The tweezer power, aberrations, and the angle between the devices and the tweezer focal plane contribute to the variations in the observed Stark shifts and loading probabilities across the devices and can be further optimized in future experiments.

From the observed Stark shifts and blow-out curves of the individual atoms, we can extract the probability of loading onto different pancakes. For this, we simulate atomic motion in each of the pancakes based on Monte-Carlo simulations and find the average Stark shift experienced by the atoms in each of these pancakes. Monte-Carlo simulation for the first pancake is shown in Fig. 5.9 a). We then take a Stark shift curve measurement of the atom in a normal free-space tweezer and scale it by the ratio of the average Stark

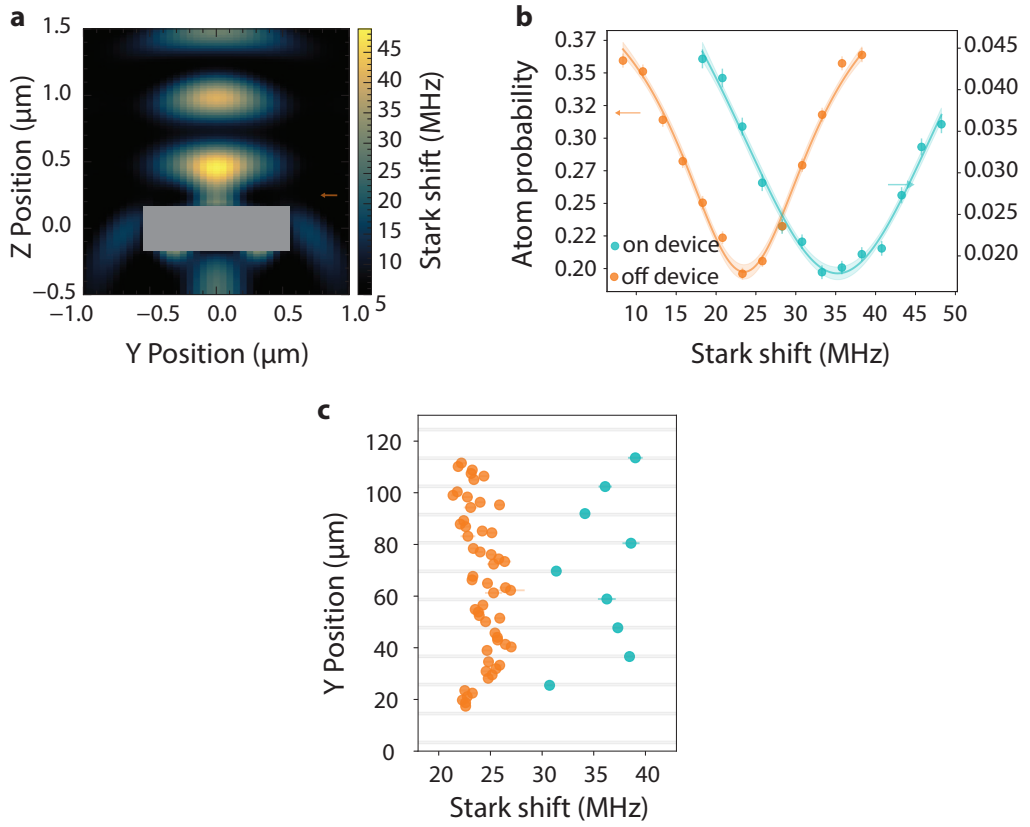

Figure 5.8: a) Cross section of the nanophotonic device and the expected Stark shift on the D1 transition for the different intensity maxima formed on top of the device by the partially reflected tweezer. b) Averaged Stark shift measurements on the 895 nm $6S_{1/2}F = 3 \rightarrow 6P1/2F = 4$ transition in between the devices (orange) and on top of the devices (cyan). Centers estimated from Lorentzian fits to similar plots at each position are used to generate (c). Error bars represent the standard error of the mean. c) The centers of the Stark shift curves for individual atoms as a function of their positions. The gray lines are estimated device positions from Fig. 5.7 a). The Stark shifts are larger in magnitude when the atoms are on top of the devices, as expected from the modified trapping potential on top of the devices as shown in Fig. 5.7 a)

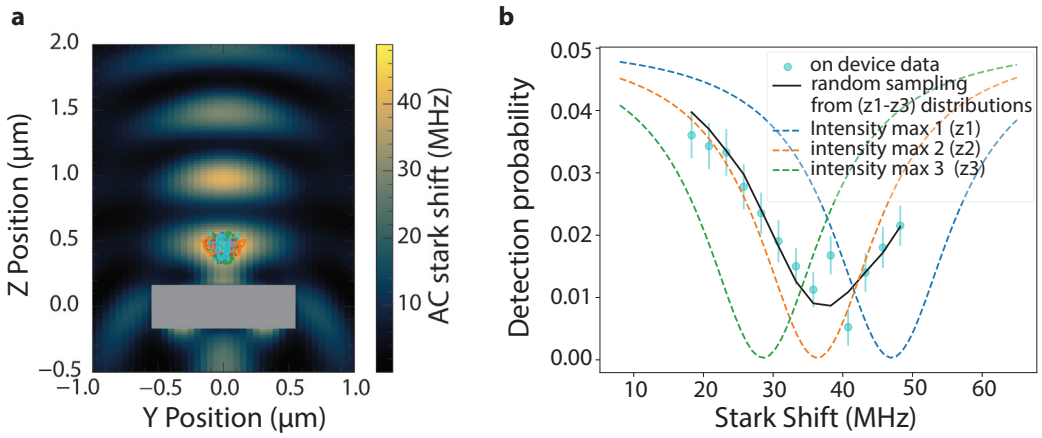

Figure 5.9: a) Monte Carlo simulation of atoms sampling different potential in the first pancake (z1). b) Expected Stark shift survival curves for the first three intensity maxima (z1-z3). The experimental curve is fitted to random sampling from the three survival-curves, with a probability of 0.29 to be in the first intensity maximum, 0.66 to be in the second intensity maximum, and 0.05 to be in the third intensity maximum.

shift in the pancake to the average Stark shift in the free-space tweezer, where both are obtained from Monte-Carlo simulations. This is the Stark shift curve corresponding to the first pancake (z1) given in Fig. 5.9 b). Stark shift curves for second and third pancakes (z2 and z3), were obtained in a similar fashion by Monte Carlo simulations in corresponding pancakes. Given that the atoms have a finite probability of sampling different pancakes at each experimental cycle, a minimization algorithm was developed to fit the curve, based on the assumption that each point of the detuning, the atoms samples different curves with a finite probability. The corresponding curve that has a loading probability of 29% to the first intensity maximum(z1), 66% to the second intensity maximum (z2), and 5% to the third (z3) is given in Fig. 5.9 b) in the solid black line. Experimental data is the Cyan markers, showing that this is consistent with the earlier Monte Carlo simulations of atoms loading onto the pancakes that showed a maximum efficiency of 40% for atoms to load onto the first pancake.

In order to fully integrate atom arrays with nanophotonics, we must be able to rearrange the atoms into defect-free arrays and then load them onto the devices. To achieve this, we start by taking an image of the initial random loading (25 ms) and rapidly process ($\sim$7 μs) the image data into an occupation matrix. This information is then used to drop the unoccupied tweezers and compress the remaining atoms into a defect-free array before translating the whole array to the devices. The experimental sequence for this procedure is shown in Fig. 5.10 a). The final step of this procedure can be done either by loading one atom per device or by loading multiple atoms to a single device. We demonstrate both capabilities in Fig. 5.10 by showing initial images of the randomly loaded atoms in free-space tweezers next to a second image of the same atoms post-rearrangement loaded onto the devices in each configuration, one atom per device (Fig. 5.10 b) and three atoms on a single device (Fig. 5.10 c). We also show averaged post-rearrangement images for 15,000 stochastic loading and rearranging events in each configuration, where seven to eight atoms can be seen in each of the post-rearrangement averaged images from the nine initial loading sites. For the single-shot images labeled Image 1 and Image 2, we first plot the two single-shot atom images and then plot a semitransparent image of the devices over them to show the device locations without obscuring the raw atom image underneath.

5.5 Future improvements

In the current set of experiments, there is a finite probability of atom loss while being transported onto the photonic device. This limitation comes from the discontinuity in the trap potential as the atoms are moved onto the devices. We overcome this by giving the

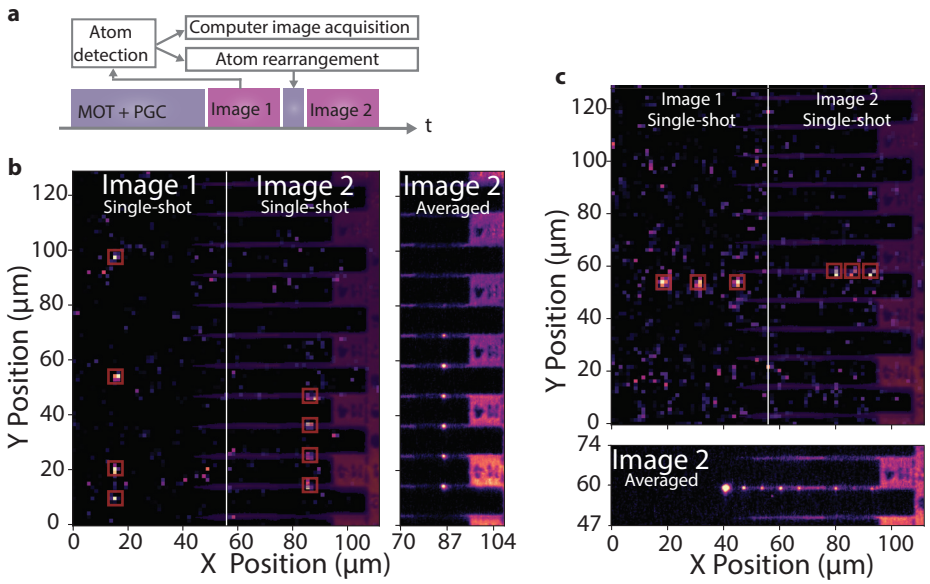

Figure 5.10: a) Experimental sequence used for defect-free rearrangement of the atoms from free-space onto the devices. After cooling the atoms and loading them into the tweezers, we take Image 1 to detect the stochastic loading pattern and use this information to rearrange the array into a defect-free configuration which we then translate over and onto the devices before we take Image 2. b) Image 1 shows a single-shot image of the randomly loaded atoms in a nine tweezer array in the loading region. After detecting these atoms in the first image, they are rearranged into a defect-free array with the same spacing as the devices. This compressed array is then loaded onto the devices and the final configuration is shown in Image 2. An averaged image of the final configuration after this procedure is shown to the right. For all images in this figure, a 25 ms exposure time was used to increase the atomic survival rate through the first image. c) Here, an array of stochastically loaded atoms in Image 1 are rearranged and loaded onto a single device as shown in Image 2. In the bottom plot, the averaged image of the final configuration is shown. The bright single atom on the left of the averaged image is an atom that is rearranged to a position outside the device region.

atoms sufficient energy to overcome the barrier. However, the resulting success rates are still limited to 30-40%. While for many probabilistic protocols, this is more than enough given the amount of multiplexing we can achieve, there are applications like fast deterministic readout, where this loss can be a challenge. For such applications, one possibility is to use ground-state cavities. The discontinuity in trap potential during the transport is a function of device thickness, and for thicknesses less than $\sim$ 250 nm, transport is possible without the discontinuity. Our device thickness of $\sim$ 330 nm is due to the reasons explained in Chapter 3. However, for ground state cavities, a thickness close to 200 nm is sufficient, allowing for discontinuity-free transportation as shown in Fig. 5.11. Here, the Monte-Carlo simulation shows the trajectory of atoms moving from free space to the first pancake of a device of thickness 180 nm when moved at a speed of 0.04 μm/μs. Since our platform can have arrays of cavities, it is possible to make interleaved or additional cavities with different thicknesses by adding new masking and etching steps. Another possibility would be to find new materials where cavity requirements and transportation requirements are met together. This can also be achieved by optimizing the silicon-to-nitride ratio in the silicon-nitride thin film used.

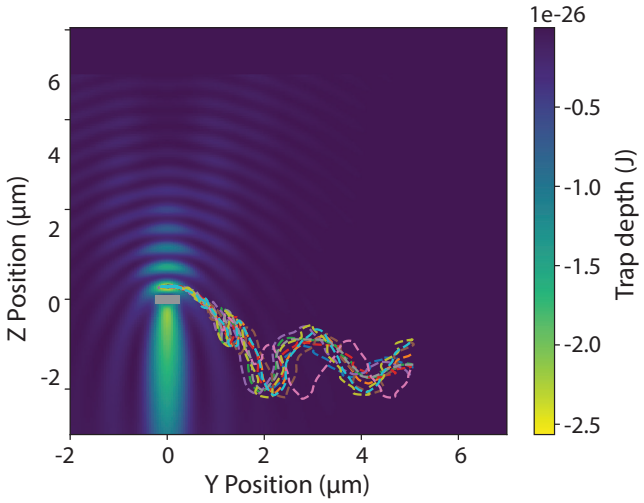

Figure 5.11: Deterministic transportation of atoms from free-space tweezer to on top of the photonic chip. Here the device is smaller and has a thickness of $\sim$ 180nm.

CHAPTER 6

A TELECOM PHOTONIC INTERFACE FROM EXCITED STATES

6.1 Introduction

In previous chapters we have shown that we can have an array of atoms coupled to arrays of photonic devices. These devices could be waveguides, cavities, or more complicated 1D or 2D structures. One of the key applications this platform can be useful for is distributed quantum computation. This requires having the ability to do computation as well as the ability to distribute entanglement. And for useful quantum computation, the system should be able to scale the number of computational qubits and photonic interfaces. In our system, large-scale multiplexing is possible in spatial and temporal dimensions. The spatial capability comes from having a large number of cavities we can couple to. And the temporal multiplexing capability comes from having a larger number of atoms than the cavities, allowing us to repeat the entanglement generation schemes for each cavity.

The computational capability can be integrated into the system using Rydberg interactions. While there are potential challenges from charge accumulations on the photonic chips, recent experiments show promising results with Rydberg gates near a similar cavity [232]. To distribute entanglement, we can couple atoms to the cavities and use them to generate photons that are entangled with the atomic states. Atoms have been integrated into similar cavity systems for more than a decade [162], including demonstration of transport and entanglement of atoms on top of these cavities [168].

For short distances ($\sim$ a few meters), the entanglement distribution can have similar efficiencies across different wavelength regimes. However, for long-distance fiber-based entanglement distribution, the fiber losses make any realistic experiments prohibitively expensive at any wavelength other than in the telecom regime, as explained in the first chapter. In this chapter, I will introduce a quantum network with individual nodes of neutral alkali atoms coupled to a nanophotonic crystal cavity (PCC) (see Fig. 1(a)) and a multilevel excitation protocol that yields emission in the telecom range. We show that this node is capable of generating a high fidelity atom–photon entangled state required for distributing entanglement. The protocol is robust under realistic conditions, and we evaluate the performance, including accurate simulations of the full atomic-level structure, the nanophotonic cavity design, and its effect on the polarization purity of laser excitation pulses. Compared to previous neutral atom proposals based on crossed fiber cavities [233] or ytterbium coupled to a nanophotonic crystal cavity [204], this protocol presents an alternative that is compatible with well-controlled alkali 'workhorse' atoms such as rubidium and cesium and only requires a single nanophotonic cavity. We establish the experimental feasibility of our protocol and show that it is within reach of the current experiment that we are building.

6.2 Generalized excitation scheme

Atom-photon entanglement can be generated across many degrees of freedom. Zeeman level, hyperfine levels are the generally used degree of freedom for atoms, and polarization and time-bin are the common photonic degrees of freedom. We choose Mf=0 Zeeman levels of

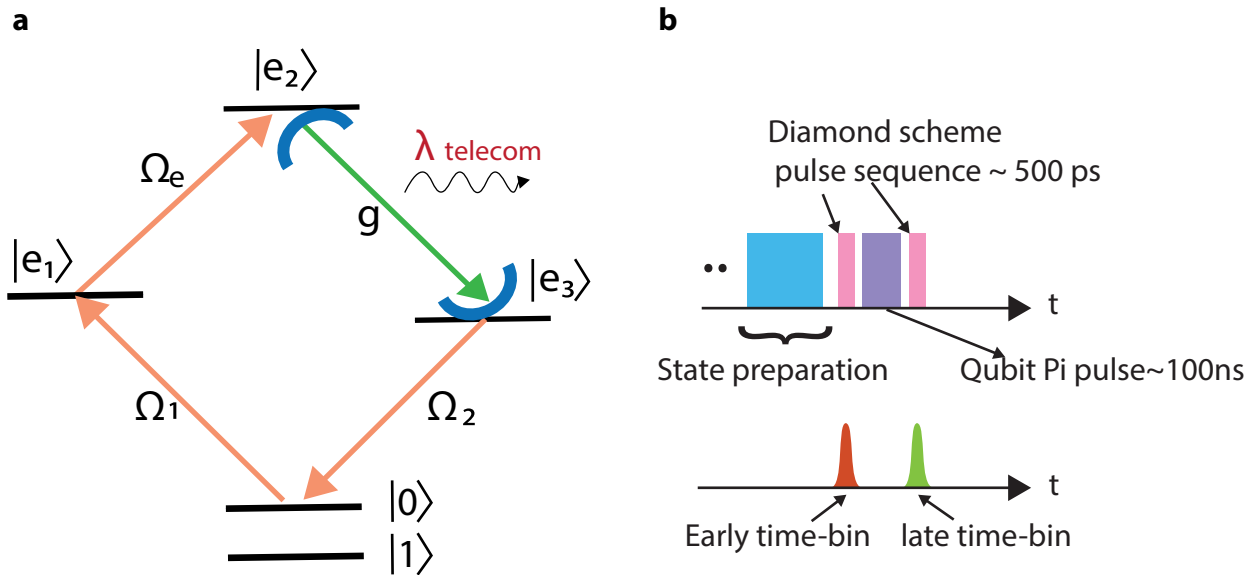

Figure 6.1: a) A generic diamond atomic-level structure with a cavity resonant with an excited-state atomic transition. $|0\rangle$ and $|1\rangle$ are the qubit states. Starting from $|0\rangle$, a pulse Ω_1 takes the electron to $|e_1\rangle$. From there a constant field Ω_e excites the electron to $|e_2\rangle$. Subsequently, a single telecom photon is emitted into the cavity and coupled to the optical fiber by decaying to $|e_3\rangle$. Finally, a calibrated pulse Ω_2 takes the electron back to $|0\rangle$. b)Entanglement scheme: After the state is prepared in a superposition of state $|0\rangle$ and $|1\rangle$, the diamond pulse sequence is executed, resulting in early time-bin telecom photon emission. Subsequently, the qubit states are then flipped, and a second diamond pulse sequence is executed, resulting in the late time-bin photon emission. At the end of this sequence, atomic states $|0\rangle$ and $|1\rangle$, are entangled with early and late time-bin photons.

the F=3,4 hyperfine levels in cesium atoms (similar levels exist for Rb85 and Rb87) as our qubit levels as they are insensitive to magnetic field noises, resulting in longer coherence. For photons we use time bins as our photonic qubit states as they are robust against polarization fluctuation commonly seen in fiber propagation. Having a long coherence time combined with low fiber loss, telecom wavelengths can enable long-distance entanglement distribution.

The protocol however is agnostic to the atomic states that are being used and can be made to work with multiple different levels. We consider the generic diamond level scheme [234, 235] shown in Fig. 6.1(a), which captures the general structure of alkali atoms such as

rubidium, cesium, and ytterbium. The scheme has two parts; a qubit part consisting of spin states $|0\rangle$ and $|1\rangle$ and a photon-generation part consisting of excited spin states $|e1\rangle$, $|e2\rangle$ and $|e3\rangle$. To generate spin–photon entanglement, the qubit states are initially prepared in a superposition state $(|0\rangle + |1\rangle)/\sqrt{2}$. A laser-driven two-photon transition then transfers the population in the $|0\rangle$ state to the excited state $|e2\rangle$, from which the atomic state coherently relaxes to state $|e3\rangle$ by emitting a telecom photon into the cavity. Finally, a strong laser pulse transfers the population from $|e3\rangle$ back to the ground state $|0\rangle$. At the end of this cycle, the qubit states are flipped ($|0\rangle \leftrightarrow |1\rangle$) by a π pulse on the qubit transition, and the cycle is repeated as shown in Fig. 6.1(b). Ideally, this creates the state

$$|\psi\rangle = \frac{1}{\sqrt{2}}(|0\rangle\,|\lambda_{\mathrm{L}}\rangle + |1\rangle\,|\lambda_{\mathrm{E}}\rangle). \tag{6.1}$$

Here $|\lambda_{\mathrm{E}}\rangle$ ($|\lambda_{\mathrm{L}}\rangle$) represents an early (late) telecom photon. This is a maximally entangled state between the atomic qubit and a photonic qubit in a time-bin encoding, which can be used to distribute entanglement between distant atoms through photonic Bell measurements.

The ideal evolution described above is in the absence of atomic spontaneous emission and cavity loss. To estimate how such imperfections limit the quality of the spin–photon entanglement, we numerically simulate the dynamics of the scheme. In a suitable rotating frame, the coherent dynamics are governed by the Hamiltonian

$$\hat{H} = \Omega_1(t)\,|\mathrm{e}_1\rangle\langle 0| + \Omega_{\mathrm{e}}\,|\mathrm{e}_2\rangle\langle \mathrm{e}_1| + \Omega_2(t)\,|0\rangle\langle \mathrm{e}_3| + g\,|\mathrm{e}_3\rangle\langle \mathrm{e}_2|\,\hat{c}^{\dagger} + h.c., \tag{6.2}$$

where $h.c.$ denotes the Hermitian conjugate of the displayed expression and $\hat{c}$ is the

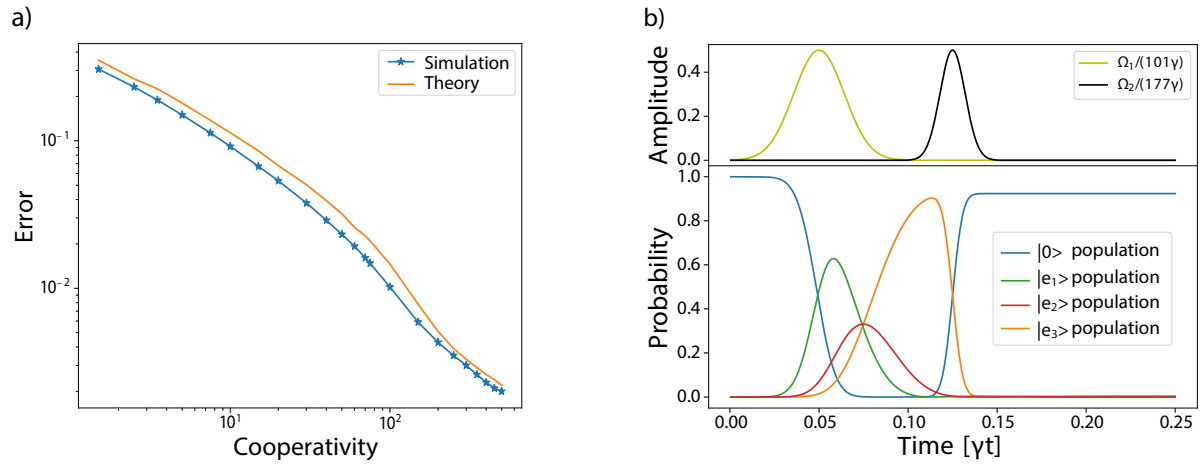

Figure 6.2: Error scaling with cooperativity for the analytical estimate (orange) and the numerical simulation (blue markers); the solid line for simulation is a guide to the eye. The simulation is in agreement with the analytical prediction of the error scaling. Two square pulses are used for both cases. For the simulation, the length of the second pulse is fixed to be 0.0002γ to minimize the spontaneous decay from state $|\mathrm{e}3,\,0\rangle$. (b) Time evolution of the excitation pulses (top) and probability in different states (bottom) for a cooperativity of $\mathrm{C} = 10$ and optimized laser couplings with Gaussian pulses. The first pulse Ω_1 (yellow) depopulates $|0\rangle$ (dark blue). The presence of light field Ω_e and the cavity leads to a transfer to state $|\mathrm{e}3\rangle$ (orange). After the photon has been emitted from the cavity, on timescale $1/\kappa$, the resulting state is $|\mathrm{e}3,\,0\rangle$. A pulse Ω_2 takes the population built in $|\mathrm{e}3\rangle$ to $|0\rangle$. In both plots $\gamma_1 = \gamma_2 = \gamma_3 = \gamma$ and $\kappa = 2000\gamma$.

annihilation operator of the cavity field. The atom-cavity coupling is characterized by g while atom-laser couplings are characterized by Ω's. Note that Ω_1, Ω_2 are time dependent while Ω_e is constant. We have assumed all laser frequencies ($\omega_{\mathrm{L}1}, \omega_{\mathrm{Le}}$, and $\omega_{\mathrm{L}2}$) to be resonant with the relevant atomic transitions and that $\omega_{\mathrm{cav}} + \omega_{\mathrm{L}2} = \omega_{\mathrm{L}1} + \omega_{\mathrm{Le}}$ where ω_{cav} is the cavity resonance frequency. We choose to have resonant driving frequencies because we want to transfer the population quickly between the excited levels to circumvent spontaneous emission.

Spontaneous emission is described by Lindblad operators $\hat{L}_1 = \sqrt{\gamma_1}\,|d_1\rangle\langle \mathrm{e}_1|$, $\hat{L}_2 = \sqrt{\gamma_2}\,|d_2\rangle\langle \mathrm{e}_2|$, and $\hat{L}_3 = \sqrt{\gamma_3}\,|d_3\rangle\langle \mathrm{e}_3|$. Here, the decay rates are denoted by γ's and we

have introduced *dump*-levels ($|d_i\rangle$), which allow us to disregard the evolution of the system following spontaneous emission from one of the excited spin states. This amounts to a worst-case scenario where we assume that any spontaneous emission brings the system to a state with zero overlap with the desired target state in Eq. (6.1). We describe the decay of the cavity field through a Lindblad operator $\hat{L}_\mathrm{c} = \sqrt{\kappa}\hat{c}$, where $\kappa = \kappa_\mathrm{f} + \kappa_\mathrm{l}$. Here, κ_f describes the desired outcoupling to a fiber while κ_l describes intra-cavity loss. Note that such a loss is detectable and thus only affects the efficiency of the protocol. We solve this equation analytically and show that the error in fidelity scales as [205]

$$1 - F \approx \frac{\ln(C)}{C}, \tag{6.3}$$

assuming $\Omega_2' \gtrsim C\gamma_3$. Here, we have defined the cooperativity $C = \frac{g^2}{\kappa(\gamma_2+\gamma_3)}$. Notably, the error quickly decreases with the cooperativity, allowing fidelities $> 90\%$ for modest cooperativities of $C \gtrsim 10$ (see Fig.6.2(a)). Furthermore, we note that some errors which are currently included in our fidelity estimate such as spontaneous decay from the $|\mathrm{e}_1\rangle$ and $|\mathrm{e}_2\rangle$ state may, in principle, be detected by the absence of a telecom-photon. Employing such error-detection can therefore further boost the fidelity at the expense of a slight decrease in the success probability of the protocol.

6.3 Implementation with alkali atoms

The generic level structure considered so far has to be implemented in real atoms. We consider cesium and rubidium atoms since they have telecom transitions from the meta-

stable first excited states and can be trapped near a PCC [162, 163, 167, 196] with strong light-matter coupling [167]. Here, we focus on an implementation with cesium atoms while a similar implementation is also possible with rubidium atoms.

Cesium has telecom transitions to $7S_{1/2}$ from both $6P_{1/2}$ and $6P_{3/2}$ with wavelengths 1360 nm (O band) and 1470 nm (S band) respectively. These levels are split into hyperfine levels and further into Zeeman sub-levels in the presence of magnetic fields. As a result, the atomic level structure includes many more levels than required for the protocol. Nonetheless, by means of selection rules, laser frequencies, and a suitable choice of qubit states, we can realize the diamond level scheme as shown in Fig. 6.3(a). We choose magnetic field insensitive clock states, $\left|6S_{1/2}, \mathrm{F}=4, \mathrm{m_F}=0\right\rangle$, $\left|6S_{1/2}, \mathrm{F}=3, \mathrm{m_F}=0\right\rangle$, as our qubit states $|0\rangle$ and $|1\rangle$, respectively. The superposition of the clock states can be created by first initializing in the state $\left|6S_{1/2}, \mathrm{F}=4, \mathrm{m_F}=0\right\rangle$ via optical pumping and then applying a $\pi/2$ pulse between the clock states.

We choose π-polarized laser excitation pulses, which allow us to make use of the selection rules $\Delta\mathrm{F} = 0, \pm 1$ and $\Delta\mathrm{m_F} = 0$ to realize the photon-generation part of the level scheme. We identify $\left|6P_{3/2}, \mathrm{F}=5, \mathrm{m_F}=0\right\rangle$ as $|\mathrm{e}_1\rangle$, $\left|7S_{1/2}, \mathrm{F}=4, \mathrm{m_F}=0\right\rangle$ as $|\mathrm{e}_2\rangle$ and $\left|6P_{1/2}, \mathrm{F}=3, \mathrm{m_F}=0\right\rangle$ as $|\mathrm{e}_3\rangle$ respectively. The first pulse takes the population to $\left|6P_{3/2}, \mathrm{F}=5, \mathrm{m_F}=0\right\rangle$ state. Depending on the strength and spectrum of the pulse, it will also off-resonantly drive the transition to $\left|6P_{3/2}, \mathrm{F}=3, \mathrm{m_F}=0\right\rangle$ state, but part of this is coupled back into the cycle by Ω_e. The transitions with $\Delta\mathrm{F} = 0$ have vanishing Clebsch-Gordan coefficients when $\Delta\mathrm{m_F} = 0$. This selection rule blocks all other off-resonant transitions in the scheme.

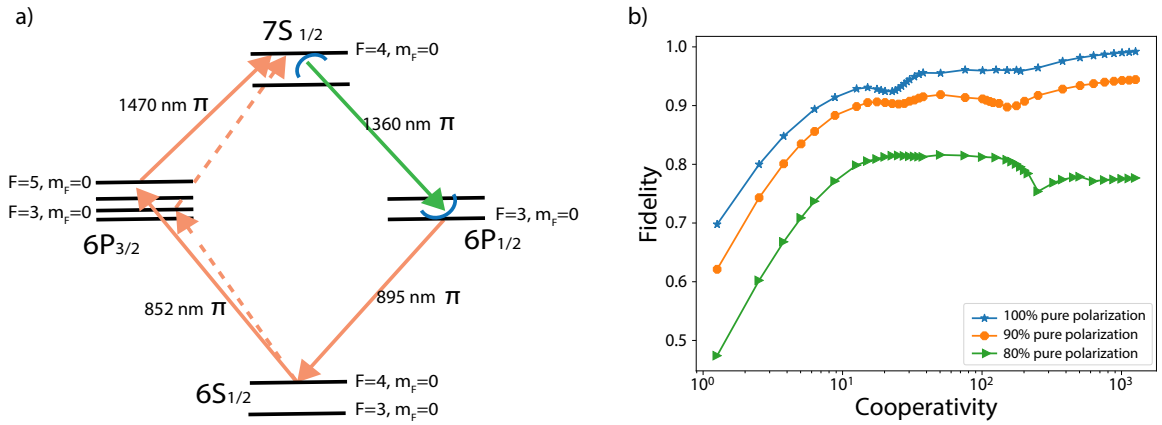

Figure 6.3: (a) A realistic implementation of the diamond scheme based on the cesium level structure. Here Zeeman sub-level states $\mathrm{m_F} = 0$ of $\left|6S_{1/2}, \mathrm{F} = 4\right\rangle$, $\left|6P_{3/2}, \mathrm{F} = 5\right\rangle$, $\left|7S_{1/2}, \mathrm{F} = 4\right\rangle$, $\left|6P_{1/2}, \mathrm{F} = 3\right\rangle$ act as $|0\rangle$, $|\mathrm{e}_1\rangle$, $|\mathrm{e}_2\rangle$, and $|\mathrm{e}_3\rangle$, respectively. A transition to $\left|6P_{3/2}, \mathrm{F} = 3, \mathrm{m_F} = 0\right\rangle$ is allowed by selection rules, but it is off-resonant. All transitions are π polarized. (b) Scaling of the maximum fidelity with cooperativity for polarization purities of 100%, 90%, and 80% for all the transitions. Solid lines are a guide to the eye. Equal contributions from σ^+ and σ^- are considered in case of polarization impurity. All hyperfine sub-levels and Zeeman sub-levels are considered in the simulation. The dips in the graph correspond to off-resonant couplings leading to lower fidelity. The simulation variables are parameterized based on the decay rate (γ) from the $7S_{1/2}$ state given by $2\pi \times 3.28$ MHz. The decay rate from $6P_{3/2}$ is $2\pi \times 5.2$ MHz and $6P_{1/2}$ is $2\pi \times 4.6$ MHz corresponding to 1.58γ and 1.38γ respectively. The cavity decay rate κ is assumed to be 200γ and consecutive square pulses are used for the optimization.

The above implementation in cesium is conditioned on polarization selection rules and is thus sensitive to polarization fluctuations. Even a small percentage of erroneous polarization will result in coupling to other levels and a high polarization purity is imperative for the implementation of the scheme. As we will see in the following section, the presence of nanostructures can have considerable effects on the polarization of a beam in its vicinity. To understand the effects of impure polarization, we simulate the full atomic-level structure and consider small admixtures of σ^+ and σ^--polarized light along with the intended π polarized driving pulses. The effect of an imperfect polarization purity on the fidelity is shown in Fig. 6.3(b). As expected, the fidelity is limited by the presence of other polarizations for high cooperativities. The coupling to other hyperfine levels also causes a non-trivial dependence on the cooperativity with local minima appearing when Ω or the cavity coupling g becomes comparable to the hyperfine splitting.

6.4 Nanophotonic crystal cavity and polarization purity

We design a PCC operating at telecom wavelengths to evaluate the expected cooperativities and effects on the polarization, and thereby the fidelity of the above scheme, using Finite-Difference Time-Domain (FDTD) simulations. We design a cavity resonant at 1360 nm corresponding to the transition between $7S_{1/2}$ and $6P_{1/2}$ at 340 nm thickness with a quality factor of 2×10^5 and a mode volume of 0.7 $(\lambda/n)^3$ as shown in Fig. 6.4(a). Here n is the refractive index of the PCC material which is taken here to be 2.016, corresponding to that of commercially available silicon nitride and used in the previous chapters. The contours of the atom-cavity coupling g are shown in Fig. 6.4(b).

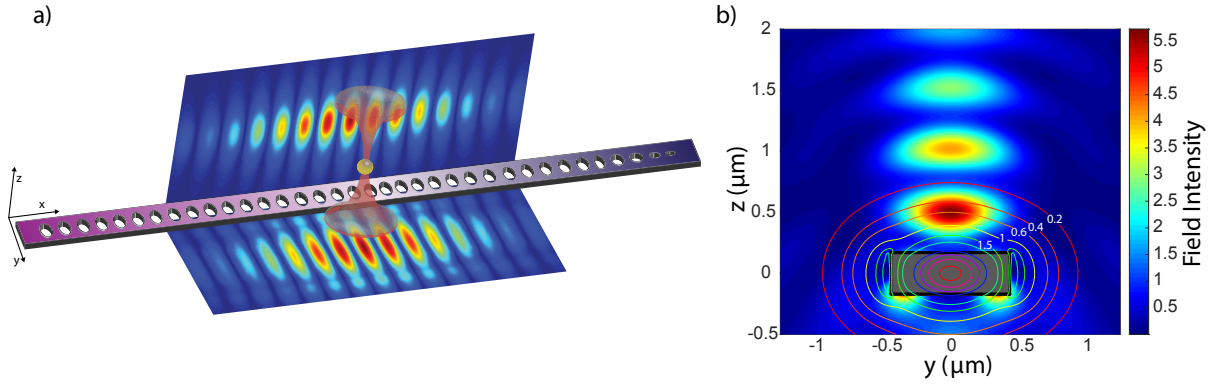

Figure 6.4: (a) Design of a photonic crystal cavity along with the resonant mode profile at 1360 nm corresponding to the transition between $7S_{1/2}$ and $6P_{1/2}$ of cesium. (b) Standing wave formation on a waveguide of width 876 nm and thickness of 340 nm when an optical tweezer beam at 910 nm is incident from above. Here the incident Gaussian is normalized at a distance of ~ 2 μm from the cavity. A cross-section of the waveguide is shown (dark rectangle). The atom can be trapped in the electric field maxima closest to the surface. The contours show lines of constant atom-cavity coupling g (in units of $2\pi\times$ GHz) exponentially decaying from the center of the waveguide. Assuming critical coupling, i.e $\kappa_{\mathrm{f}} = \kappa_{\mathrm{l}}$, the corresponding cooperativities are in the range from 5 to 260.

The atom is coupled to the resonant mode of the cavity through the evanescent field, which decays exponentially with increasing distance from the surface of the structure. We consider trapping an atom in the standing wave formed by an optical tweezer on the surface of a waveguide [162]. Fig. 6.4(b) shows this standing wave formation when the incident tweezer beam interferes with the reflected beam from the waveguide. An atom can be loaded in the trap formed by the intensity maxima closest to the waveguide (or a cavity region) as shown in previous chapters. Assuming critical coupling with a quality factor of 2×10^5, cooperativities of 50 can be achieved at the region of trapping, which will allow high fidelity implementation. The assumption of critical coupling will, however, reduce the collected photon number from the cavity to half, which would affect the success probability but not the fidelity of the protocol.

We now look at how the polarization purities of the addressing beams are affected by the presence of this cavity. The classical light fields Ω_1, Ω_e, and Ω_2 can address the atom based on the direction set by the quantization axis and the polarization requirement. Since we are interested in π polarizations for the implementation of our scheme, we fix the cavity polarization axis (y-axis based on the simulated fundamental TE mode) to be our quantization axis. The requirement of π (set to be y) polarization for classical fields (Ω) restricts their propagation direction to the x or z axis. With the propagation direction fixed along the z-axis, we simulate how the presence of the PCC affects the polarization purity of the exciting beams near the PCC surface. Fig. 6.5(a) shows the polarization purity of a 895 nm (corresponding to the Ω_1 field) y-polarized plane wave incident normal to the surface of the PCC. The addressing beams do not have to be focused tightly to achieve the desired Rabi frequencies and are therefore modeled as plane waves. We find that the reflection from the PCC can have considerable effects on the polarization purity of the driving pulses, depending on the position where the atom is trapped. While being confined by the standing wave optical trap, the atom still has some thermal motion and therefore samples over a region determined by the trap geometry and the temperature of the atom [167]. This leads to an effective average polarization purity as well as an average cooperativity for a given atomic temperature. Positioning the atom in a region of high polarization purity is thus imperative for high-fidelity implementation of the scheme.

The position of the atom close to the surface of the cavity can be tuned by changing the thickness of the cavity and thereby changing the trap position [162]. This tunability allows us to have control over the effective polarization purity as well as the atom's coupling to

the cavity field. The trapping distance from the surface and the corresponding polarization purity in the trapping region for different thicknesses of the cavity is shown in Fig. 6.5(b) for a trapping field at 910 nm. In general, we find that polarization impurities are higher when the atom is trapped closer to the cavity. The given polarization purity is an average over a volume of $200 \times 200 \times 50$ nm^3 in the x, y, and z dimensions, similar to observed sizes of atomic wavefunctions near a PCC [167].

Along with the polarization purity, the trapping distance also determines the atom's coupling to the cavity field. The effective coupling experienced by the atom is directly proportional to the electric field of the cavity mode at the position of the atom [130]. This electric field falls off exponentially with the distance from the surface. Consequently, strong coupling requires the atom to be placed as close to the cavity as possible. This leads to an apparent trade-off between polarization purity which increases with trapping distance and the atom-cavity coupling which decreases with trapping distance.

6.5 Realistic results

To estimate realistic fidelities attainable for the diamond scheme, we simulate a cavity with a thickness of 340 nm, quality factor of 2×10^5, and extract cooperativity and polarization purity at the trapping region from the FDTD simulations. Assuming critical coupling such that $\kappa_\mathrm{f} = \kappa_\mathrm{l}$, we attain a cooperativity of 35 averaged over the region where the atom would be trapped. At this trapping region, we find average polarization purities of 93.89% for 852 nm, 94.99% for 895 nm, and 97.79% for 1470 nm plane waves incident from the positive z-axis. A polarization purity of 97.66% was found for the cavity field. Based on these polar-

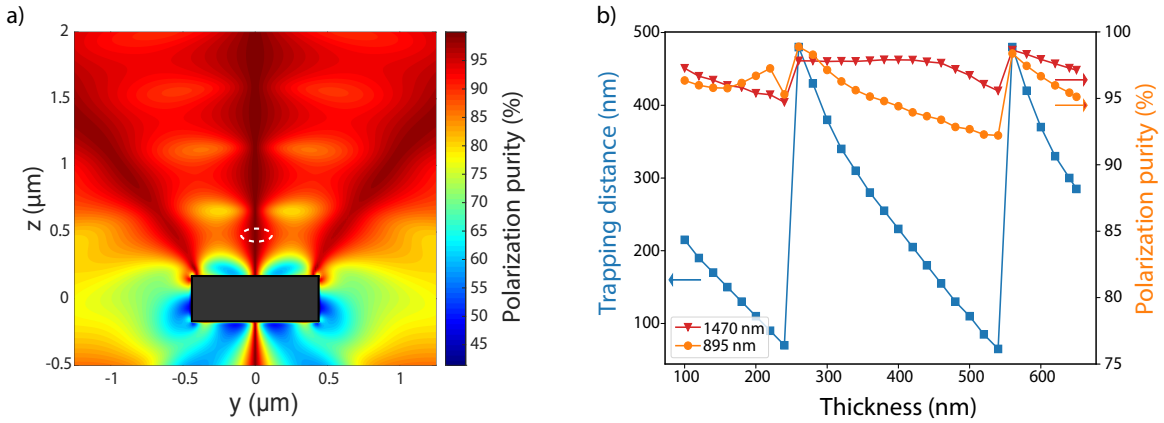

Figure 6.5: (a) A nanostructure modifies the polarizations of an incident light field near its surface. An 895 nm plane wave with polarization in the y direction is incident on the waveguide (black rectangle) from the positive z-axis. The time-averaged polarization purity around the waveguide is shown in the cross section. The region where the atom would be trapped based on the intensity distribution in Fig. 6.4(b) is marked by a dashed white ellipse. (b) The trapping distance (blue squares) of the atom from the surface of the device can be modified by changing the thickness of the waveguide. The corresponding polarization purity also changes with the thickness of the waveguide (orange dots for 895 nm and red triangles for 1469 nm). The polarization purity is averaged over an area of $200\times200\times50$ nm^3. Solid lines are a guide to the eye.

ization purities, a fidelity of 0.93 can be achieved for the simulated average cooperativity of 35 with square pulses of length 2.5 ns for Ω_1 and 0.5 ns for Ω_2.

We note that reflections of the addressing beams from the PCC can lead to position dependent variations of the corresponding Rabi frequencies. From the FDTD simulations, we estimate that such variations will reduce our fidelities by 2.5%. This error can be further reduced by cooling the atom to lower temperatures using Raman sideband cooling or using tighter traps [199].

Cavities of similar and higher quality factors have been made, and pulses as short as 50 ps can be made using commercially available electro-optic modulators, enabling realistic high fidelity implementation of the scheme. Moreover, fidelities greater than 0.9 can be achieved with cooperativities as small as 15 for the simulated polarization purity, implying the possibility of high fidelity implementation even in lossy cavities and higher temperatures of the atom. Additionally, further optimization of the cavity can be performed to obtain higher atom-cavity coupling, higher polarization purity, and lower cavity losses to improve the fidelities.

6.6 Other sources of errors

Apart from the dominant error sources due to the polarization purity of the control fields that are affected by the nanostructure and the off-resonant coupling to additional atomic levels, we consider additional noise sources and estimate their contribution:

Amplitude noise: Laser amplitude noise causes a variation in Rabi frequencies affecting our fidelity. We estimate that with standard amplitude stabilization techniques these

variations will be below 0.05% which would lead to a 0.01% reduction of the entanglement fidelity.

Random light shifts: As the atom moves in the optical tweezer due to its temperature it experiences varying light shifts from the trapping beam. These variations are < 5MHz for typical trap intensities [167] which can lead to a small reduction of entanglement fidelity by 0.1%. However, these variations can be avoided by using magic wavelength traps in the cesium implementation or by performing the protocol stroboscopically with the trap being switched off during the entanglement generation [230].

Qubit dephasing in optical tweezers: The tight focussing of the trapping beam leads to fictitious magnetic fields that can cause decoherence of the qubit states. An appropriate choice of magnetic fields can be used to mitigate this effect [162]. For $m_F = 0$ Zeeman states, as considered here for the cesium implementation of our protocol, this source of error as well as dephasing caused by external magnetic field fluctuations is negligible.

Scattering: Even though the transition frequency of the atom is far detuned from the tweezer frequency, the high intensity of the tweezer beam can cause off-resonant scattering leading to lower coherence times. For realistic intensities, we expect the scattering rate to be at the Hz level, enabling sufficiently long coherence times.

Polarization noise: Commercially available polarization-maintaining fibers offer polarization extinction ratios close to 25 dB. With these values, we expect less than 0.05% fidelity reduction of the entangled atom-photon state. Additional polarizers can be used to reduce this value further.

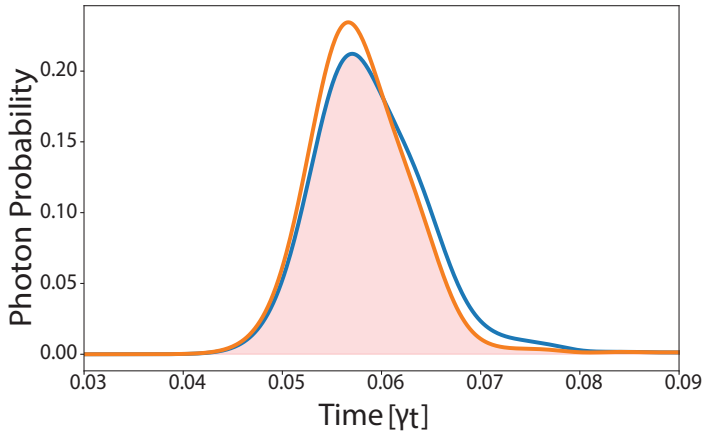

Figure 6.6: Due to the atomic motion the shape of the emitted photon varies, which can limit the interference contrast in a two-photon interference scheme. We find on average a 15% reduction in the overlap (shaded region) between the ideal photon (orange) and the emitted photon (blue).

6.7 Entanglement of distant quantum nodes

Quantum network nodes can be entangled through beam splitter interference schemes, which rely on the indistinguishability of the photons. The variations of cavity coupling and Rabi frequencies in the trap region will reduce the indistinguishability of the emitted photons, which can affect the entanglement fidelities of distant nodes. From our FDTD simulations, we estimate that the overlap of emitted photons in the case of realistic Gaussian pulses can be reduced by 15% on average due to Rabi frequency and cavity coupling variations (see Fig. 6.6). The reduction in fidelity arising from such overlap mismatch can be mitigated by time-filtering, by which we can maintain high fidelity at the expense of entanglement rate[236].

6.8 Extensions of the diamond scheme

The diamond scheme presented in this chapter enables us to generate atom-telecom-photon entanglements. However, minor modifications to the protocol can also allow for more complex atom-photon states such as Greenberger–Horne–Zeilinger (GHZ), or cluster states. The generation of the GHZ state can be done very similarly to the entanglement generation scheme depicted in Fig. 6.1(b). After the state preparation, applying consecutive diamond pulse sequences N times, followed by a pi pulse to flip the qubits, and reapplying N number of diamond pulse sequences results in an N-qubit GHZ state. Out of the N qubits, N-1 will be photoni,c along with one matter qubit. A simplified version of this is given in Fig. 6.7(a), where five diamond pulse sequences are applied before and after the π pulse to flip the qubit. At the end of this sequence, the atom is entangled with 5 telecom photonic qubits in the form:

$$\begin{aligned} |\Psi\rangle = \frac{1}{\sqrt{2}} \big(&|1\rangle|\lambda_{\text{early1}}\rangle|\lambda_{\text{early2}}\rangle|\lambda_{\text{early3}}\rangle|\lambda_{\text{early4}}\rangle|\lambda_{\text{early5}}\rangle \\ &+|0\rangle|\lambda_{\text{late1}}\rangle|\lambda_{\text{late2}}\rangle|\lambda_{\text{late3}}\rangle|\lambda_{\text{late4}}\rangle|\lambda_{\text{late5}}\rangle \big) . \end{aligned} \tag{6.4}$$

Similarly, the scheme can be extended to generate a cluster state by initializing the atom in a superposition state, followed by sequences of diamond pulse sequence and $\pi/2$ rotation on the atom [237, 238]. Each round of the $\pi/2$ + diamond pulse sequence adds another photon to the generated linear cluster state. A linear cluster state generated in this fashion with 10 pairs of $\pi/2$ and diamond pulse sequence is demonstrated in Fig. 6.7(b). At the end

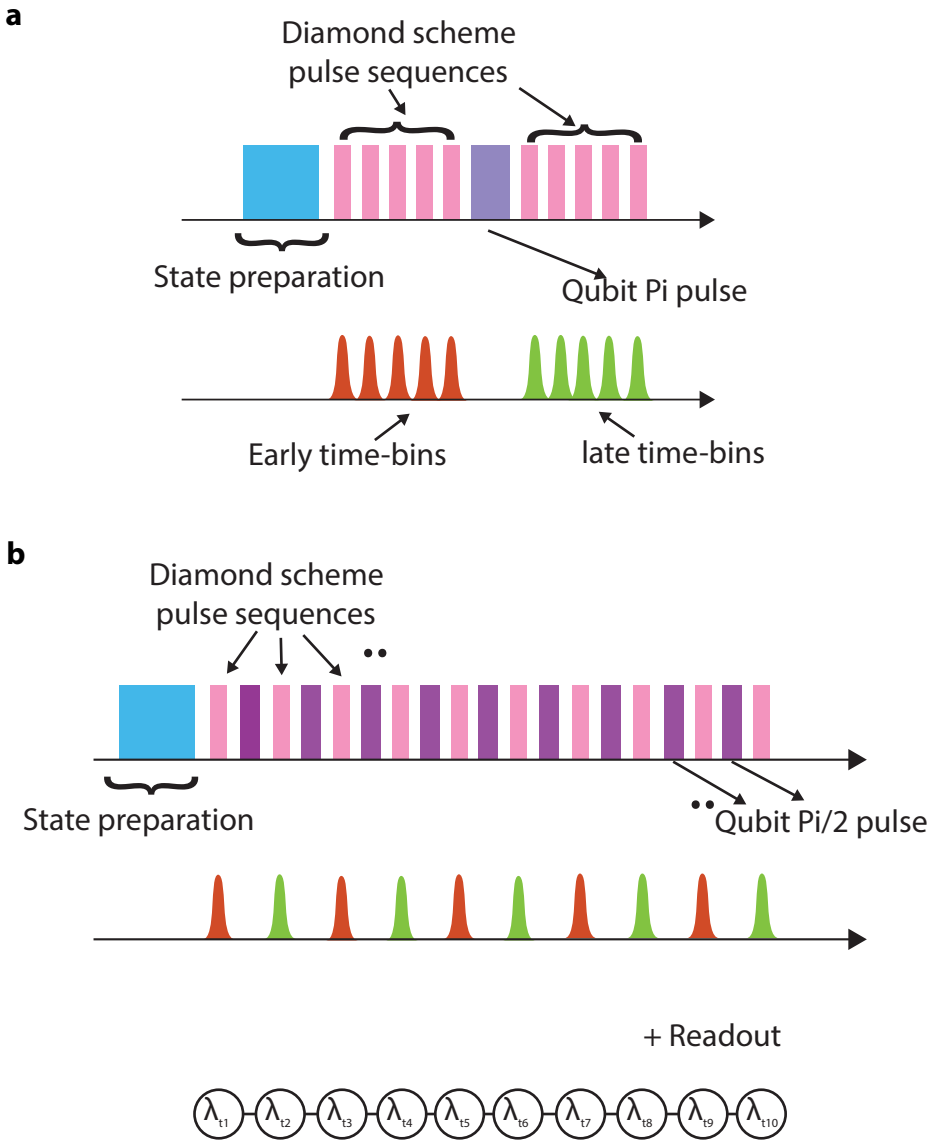

Figure 6.7: (a) Extension of the entanglement scheme to generate 6 qubit GHZ state with 5 photons and an atom. Here, N diamond pulse sequences are executed before the Pi pulse and following the pi pulse to generate an N qubit cluster state. (b) Modification of our scheme to generate a 1-dimensional cluster state. For generating ten photons in a cluster state pi/2 pulse rotation and diamond pulse sequence are repeated ten times (including the pi/2 part of the state generation). Finally, the atomic state is readout to leave the photons in a ten-qubit linear cluster state.

of the sequence, the cluster state consists of 10 photons and the atom. By reading out the atomic degree of freedom, the photons are left in a 10-qubit linear cluster state that can be used as a resource state.

6.9 Summary and Discussion

In this chapter, we proposed and analyzed the performance of a node architecture that consists of an individual atom coupled to a nanophotonic crystal cavity that operates at telecom wavelengths. We have shown that this node is capable of generating a high-fidelity atom-photon entangled state under realistic conditions taking both the full atomic-level structure and the properties of the nanophotonic cavity into account. We have analyzed the scaling of the fidelity with the cooperativity of the atom-cavity system and find that fidelities larger than 0.9 are attainable with the current state of the art technologies. Further, apart from the clock state implementation presented in the main text, one can also find a level scheme based on stretched states, where off-resonant transitions are forbidden for pure polarizations. Schemes based on stretched levels have an additional advantage of being insensitive to a subset of polarization impurities based on the level selections. However, the coherence time of stretched state qubits are smaller as they are more sensitive to magnetic field fluctuations.

Our assumptions are rather conservative and we expect that even higher fidelities are achievable. For instance, lower temperatures of the atom would reduce the region over which the polarizations and Rabi frequencies of the driving fields are averaged and would lead to higher fidelities. Furthermore, a careful cavity design could enlarge the regions of

high polarization purity and align them with the trapping region.

Finally, the proposed node architecture can be extended in several important directions. A multi-qubit node can be achieved by coupling multiple atoms to the same cavity [239–241]. Operations between these qubits can be enabled via photon mediated gates through the cavity. Such an architecture will enable advanced network functionalities such as cavity mediated entanglement purification [121, 242] and quantum repeater protocols [92, 233, 243, 244], thereby paving the way towards large scale multi-node quantum networks.

CHAPTER 7

A RESONANT CAVITY ARRAY FOR MULTIPLEXED INTERACTIONS

7.1 Introduction

In the previous chapters, we have introduced our platform that can combine atom arrays with arrays of photonic devices, along with a protocol that allows the generation of entangled telecom photons from atoms trapped on top of the photonic cavities. The photonic devices that atoms were trapped on in Chapter 4 were cavities that can be used for the above entangled atom photon generation. However, they were not on resonance with the atomic transition, resulting in no coupling between the atom and the cavity. In this chapter, we introduce a new set of chips with multiple photonic devices that can be brought to atomic resonance. As a precursor to entangling telecom photons with atoms, this set of devices can also be used to get Purcell-enhanced telecom photons.

Single photons are a quantum resource state for Gaussian boson sampling [245] and linear optical quantum computing [246]. Single photons can also be used for enhanced imaging [247, 248] and cryptography [249]. In this chapter, we will cover the use of excited states for generating single photons, the new set of photonic devices with multiple devices that can be brought to resonance, and how we tune the cavity resonance frequencies. This will be presented along with the setup and experiment for single photon generation and extraction.

7.2 Single photons from excited state

Similar to the scheme presented in the previous chapter, single photons can be extracted from atoms coupled to photonic devices. However, the requirements for this are simpler, as ground state qubit manipulations and coherent transfer back to the initial states are not a requirement. The general diagram for the single photon source is given in Fig. 7.1. The atoms are excited using a two-photon excitation to the $7S_{1/2}$ state. The atoms can decay back to the ground state following the excitation pathway, or through the $6P_{1/2}$ state. However, the $7S_{1/2} \rightarrow 6P_{1/2}$ transition is coupled to the cavity, leading to Purcell-enhanced emission through the cavity. From the $6P_{1/2}$ state, atoms can decay to both ground levels. For continuous measurements, we keep a re-pumping beam resonant with the $6S_{1/2}$ to $6P_{3/2}$ F=3-4 crossover to avoid pumping to the state.

7.3 Resonant cavity array

In chapter 4, we showed how atoms can be trapped on top of the photonic device. However, the cavities presented in that chapter were not resonant with the atomic transitions. To overcome this, new sets of devices were fabricated, with the additional requirements of having more than ten devices that can be brought to resonance (and within the objective field of view), high quality factors, and good cavity to fiber coupling efficiencies. The fabrication details followed for the devices are given in Chapter 3, and are made completely in-house. The quality factors of the cavities are a function of the design, the side wall quality, and the roughness of the sample, as the scattering loss is a function of these. This can be

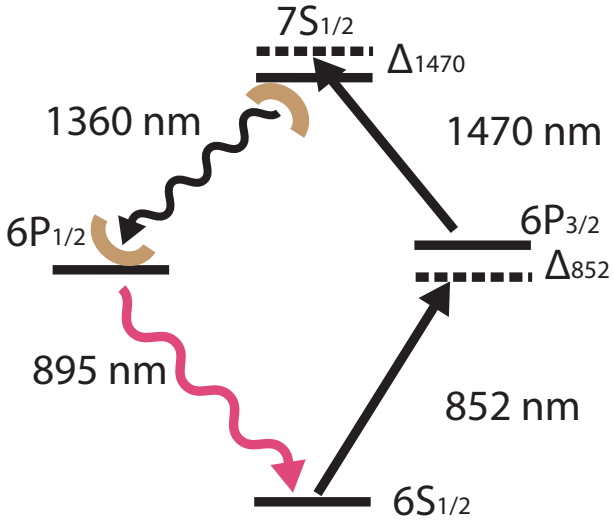

Figure 7.1: Single photon generation scheme for cesium atoms. Atoms are doubly excited to $7S_{1/2}$ state, which is coupled through cavity to $6P_{1/2}$ state. Purcell enhanced emission results in a telecom photon being emitted into the cavity before atoms decay to the $6P_{1/2}$ state, and eventually decaying back to the ground state.

optimized by better cavity design parameters and optimized etching parameters. Having multiple devices on resonance across a chip requires nanometer-scale accuracy, across a large region. And requires this accuracy to carry over through the ebeam, development, and the etching process. This task is particularly challenging and requires tens of fabrication rounds to achieve a sample that has 20-30 devices that can be brought to resonance.

Finally, we also require a high coupling efficiency of photons emitted into the cavity to fibers outside the chamber. Free-space coupling, introduced in Chapter 3, is used to couple light in and out of the waveguides, and coupling efficiencies unto $\sim 65\%$ have been measured outside the chamber. This can also be improved by using different combinations of lenses/objectives and the taper end width of the waveguide. Similarly, another coupling efficiency that we need to take into account is the coupling efficiency from the cavity to

the waveguide. A photon emitted into the cavity by the atom can either be lost to vacuum through intrinsic scattering losses (κ_s), or can be coupled to the waveguide through the cavity mirror (κ_{wg}). While high quality factors mean the photon lifetime in the cavity is higher, this increase in lifetime could be coming from lower κ_s or lower κ_{wg}. For our application, we need to maximize the collection of cavity photons, and this requires large κ_{wg} and small κ_s (also known as the overcoupling regime of the cavity). The ratio of κ_{wg}/κ_s can be increased by reducing the scattering losses and by reducing the cavity mirror strength. The scattering loss is a function of the cavity design, sidewall quality, and the device roughness, and improving this requires more careful design and etch parameter optimizations. On the other hand, κ_{wg} can be increased by reducing the number of cavity mirror holes on the coupling side of the cavity.

In our experiments, we have different cavity hole numbers added to the chip to make use of different cavity strength regimes. This is a unique advantage and capability of the system, and enables different types of cavities to be combined in the same system. As the number of cavity mirror holes increases, the mirror strength increases and κ_{wg} reduces. We can estimate the cavity outcoupling efficiencies assuming that at the steady state, the reflection is given by: [250, 251].

$$R = \frac{(1-\kappa)^2}{(1+\kappa)^2}, \tag{7.1}$$

where $\kappa = \kappa_{wg}/\kappa_{sc}$. Experimentally, R is given by the value of the normalized reflection

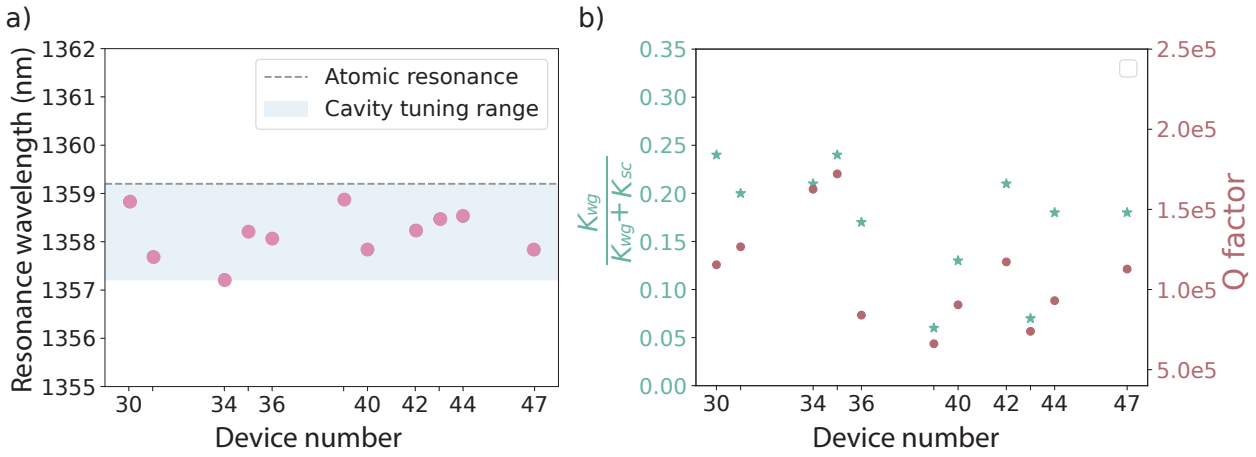

Figure 7.2: a) An array of cavities within the cavity field of view that can be brought to resonance. These cavities have resonance frequencies that are blue detuned with respect to the atomic transition and within our tuning range of 2 nanometers. b) Quality factors and cavity outcoupling of devices shown in a). Here, the device number corresponds to the labels given to devices during fabrication. The consecutive device number corresponds to devices separated by 11 μm. The tick labels correspond to the devices plotted.

dip at resonance. From here we have:

$$\frac{\kappa_{wg}}{\kappa_{sc}} = \frac{1-\sqrt{R}}{1+\sqrt{R}} \tag{7.2}$$

Finally, the total photon collected from the resonator compared to the loss is given by:

$$\frac{\kappa_{wg}}{\kappa_{wg}+\kappa_{sc}} = \frac{1}{1+\frac{\kappa_{sc}}{\kappa_{wg}}}. \tag{7.3}$$

.

The plot of quality factors and cavity waveguide Coupling efficiencies for a set of devices is shown in Fig. 7.2. Here, the device number corresponds to the label assigned to each cavity on the chip, with adjacent cavities getting consecutive numbers. All the device numbers shown in the plot are within the tuning range of the atomic resonance. Typical coupling

efficiencies of the cavities range from 10%-40% limited by the mirror numbers. Improving the fabrication and the design to reduce the scattering losses, while simultaneously reducing the mirror number, can enable similar cavity quality factors with better out-coupling efficiencies. A typical device that we make can have ∼100-150 devices within a 5 nm range of the target wavelength.

7.3.1 Device tuning

The devices in Fig. 7.2, while close to resonance, is not exactly on resonance. To couple these devices to the atoms, we need the ability to tune the cavity resonance. Multiple approaches have been used for cavity resonance tuning. In solid state experiments, a common method is gas deposition, where a thin layer of material is deposited onto the devices [252]. However, since our experiments are done in a vacuum, this method can have an impact on the vacuum lifetime of the atoms or the pump lifetime. An alternate method based on heating has been previously demonstrated [162]. In this method, a high-power laser is shone onto the devices, modifying their refractive index and thereby their resonance frequency. In this case, the laser used for heating the device has to be continuously on to lock the cavity resonance at the target frequency. The combination of the atom and the material for the photonic device leads to two major considerations for the heating laser. For effective heating of the device, the heating laser has to have a higher frequency than the bandgap of the device material. Second, if the heating-laser frequency is larger than the frequency of different transition frequencies of the atom, there is a chance of atoms scattering some of these photons. For qubits, this could lead to decoherence and infidelities.

Given that the cesium atoms ground state transitions are at 852 nm and 895 nm, we are able to use any wavelengths larger than this. However, the typical bandgap of silicon nitride is ∼234 nm, which is much higher than atomic transition frequencies. This makes it challenging to use a heating laser directly on the silicon nitride device. However, this can be overcome by using an intermediate layer to absorb heat and then transfer it to silicon nitride. Previously, this approach was used to shift cavity resonance by depositing silicon in a small region close enough to the cavity [162]. Silicon has a band gap close to 1107 nm, allowing the use of wavelengths in the range of 1060 nm. Heating the silicon using an above-bandgap excitation and transferring the heat to silicon nitride can then be an effective way to tune the cavity resonance. In our system, the devices are directly attached to the silicon substrate, allowing direct tuning of these cavities without additional heat transfer layers. We shine a focused 1060 nm laser directly at the edge of the waveguide where the device is attached to the substrate. The power of the 1060 nm laser then directly corresponds to the device resonance frequency as shown in Fig. 7.3.

The cavity resonance wavelength can be tuned 2-3 nanometers red of its starting wavelength using this method. Beyond this, we noticed, the devices were breaking off or completely losing the cavity feature. Given this one-directional tuning capability, we can only bring the devices whose resonance wavelength is at a lower wavelength than the atomic transition. The final device that was placed in the chamber had 17 devices that could be brought to atomic resonance, with 14 of them in the same cavity field of view. The final chip had even more devices; however, around one-third of the devices broke when the chip fell down while being mounted inside the chamber.

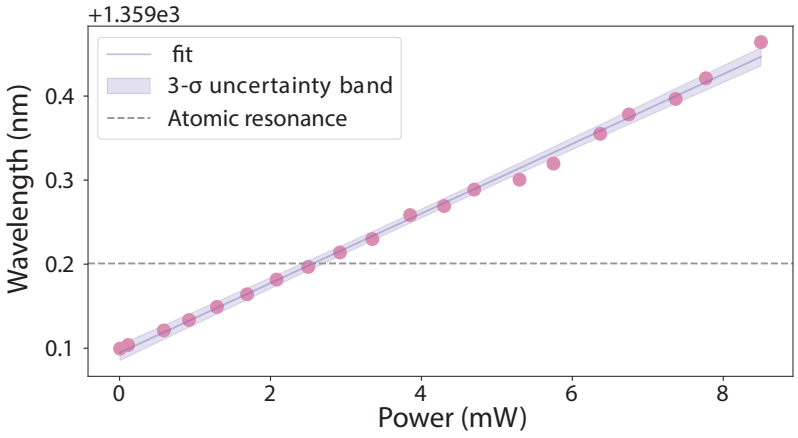

Figure 7.3: The device resonance frequency is tuned by shining a focused 1060 nm laser beam at the edge of the device. Here, the dashed line corresponds to the atomic transition. The slope of the heating shows a tuning capability of ∼0.05 nm/mW of laser power.

7.4 Device drift

In the experiment, we start at a point where multiple of these devices can be brought to resonance. However, over the course of the experiment, we have observed multiple occurrences of resonance frequency drifting across all the devices. The main reason behind this drift is unwanted deposition on the devices. We observe device resonance frequency variations during the baking process, during dispenser activation, and during normal operation. During the baking procedure, we observed a nominal variation of 0.3 nanometers towards lower wavelengths as shown in Fig. 7.4 (a). This variation is small and still keeps most of the devices within the tuning range. Under previous dispenser activations, we had a nominal redshift of the wavelength on the devices. However, during the bake of the above devices, the dispenser had an unexpectedly high flux of Cesium at much lower currents than normal. While the dispenser had a working point of 3.7 to 4 Amps, after the venting, pumping, and baking, the working point of the same dispenser is between 2 to 2.2 Amps. Similar behavior

was not observed in the previous rounds of venting and pumping, and the reason for this observed difference in the working point of the dispenser is not clear. As a result, the devices were exposed to a high flux of dispenser output for more than a week, resulting in around 1 nanometer of redshift of the resonant wavelength. Given that the devices can only be tuned towards higher wavelengths, this reduces the number of devices from the original 17 that can be used. However, the chip also has more devices that originally started out at 3 to 4 nanometers blue of the atomic resonance, now entering the tuning range. Fig. 7.4 a) shows resonance frequencies of a few devices before baking (circles), after baking/pump activation (diamonds), and after dispenser activation (asterisk). Uniform behavior of blueshift in wavelength after baking and redshift after dispenser activation is observed. These devices are on the same chip as the set of devices presented in Fig. 7.2, but in a different region. These devices can be accessed by moving the objective.

Similarly, normal operations in high dispenser current also cause a gradual redshift in device resonance frequencies, as shown in Fig. 7.4 b). The rate of the redshifts is correlated with the dispenser current and can be increased or reduced by the corresponding increase or reduction in the dispenser current. While the chip was made to take into account potential redshifts with extra devices that come into our tuning capability with redshift, being able to work with the same set of devices is desirable. Each chip region can have different optimal MOT loading parameters, and each device set can have slightly different cavity parameters, requiring separate optimization for each cavity. Light-induced atomic desorption (LIAD) is an effective tool in removing certain deposits from the device surfaces. We see that devices can be blue detuned back to their original resonance frequency with continuous exposure

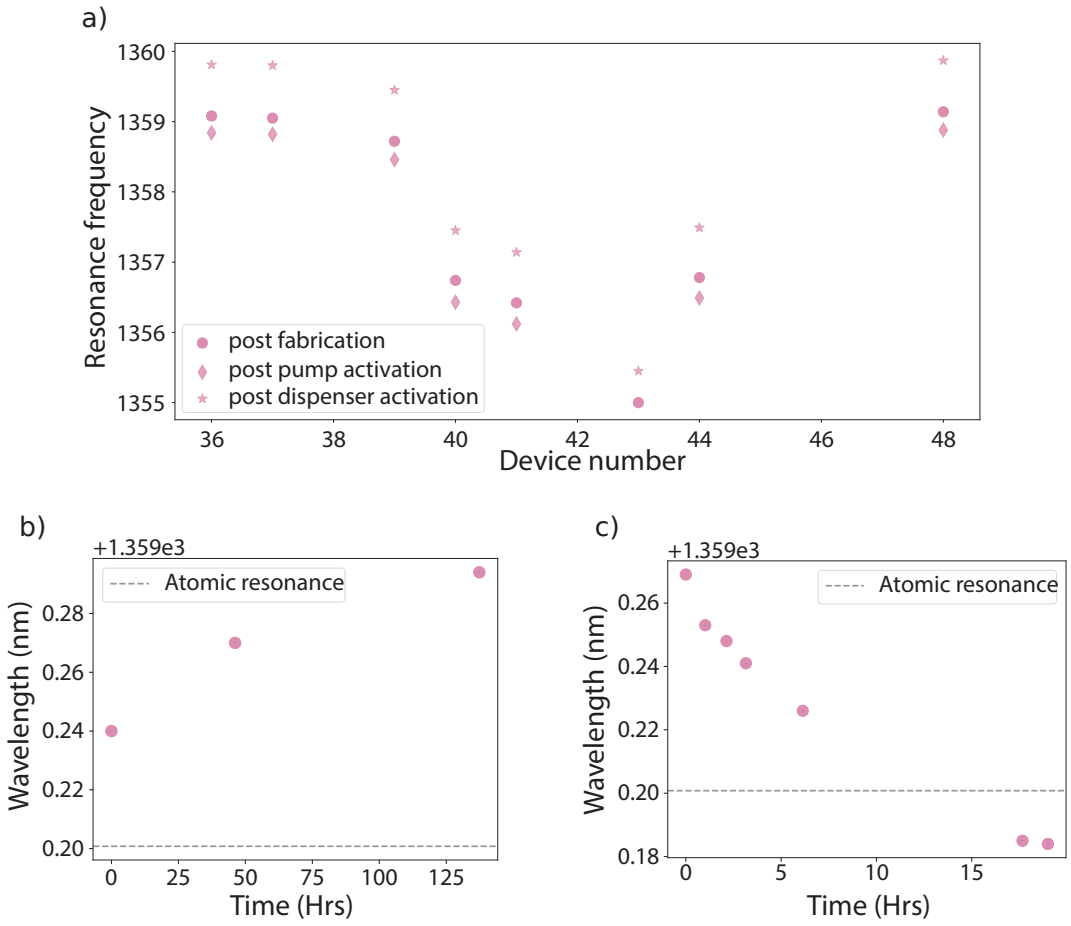

Figure 7.4: a) Resonance frequencies of a set of devices and their variations during different stages of vacuum chamber baking. The devices were found to blue-shift by $sim0.2$ nm (diamond) during the bake at 140 °C and pump activation. Following this, the dispensers were activated and the resonance frequencies were found to be shifted by $sim1$ nm (asterisk). b) During the regular experiment, the devices can red shift based on the dispenser current. c) LIAD can be effectively used to blue shift devices that have red shifted during the operation.

to LIAD beam. Fig .7.4 c) shows that devices blue shift by ∼0.1 nm over the course of a day with the dispenser switched off for the previous set of devices in the chamber. The blue shift from LIAD is a function of the angle of exposure, the power of the laser used, and the wavelength. We observe differences in rates of this blue shift compared to the previous chip under similar conditions, and this requires further studies to understand the origin of this variation. Since the rate of redshift is proportional to the dispenser current and blue shift is a function of LIAD, it is possible to work in a regime where devices always remain blue shifted with respect to the atomic transition, or even to passively keep the devices in resonance with the atomic transition.

7.5 Experimental setup

The main experimental setup is introduced in Chapter 2. For single photon extraction, cavity locking, and atomic addressing, we make use of certain paths shown in Fig. 2.8. An 852 nm line is added to one of the MOT beams that goes through the objective and is focused down to tens of microns to drive high Rabi frequency transitions in the D2 line. This line goes through an amplitude EOM (iXblue 20GHz Mach Zehnder interferometer) for pulsed excitation of the atoms, along with a semiconductor amplifier (SOA) for high extinction ratio. Along with this, a focused 1470 line, different from the imaging beam, is combined into the objective to drive fast Rabi oscillations from $6P_{3/2}$ to $7S_{1/2}$. These beams are shown in Fig. 7.5. The atoms excited to state $7S_{1/2}$ emit a photon into the cavity and decay back to the ground state. We collect the photons emitted into the cavity using the free-space coupling technique introduced in chapter 3, and route them to a superconducting nanowire

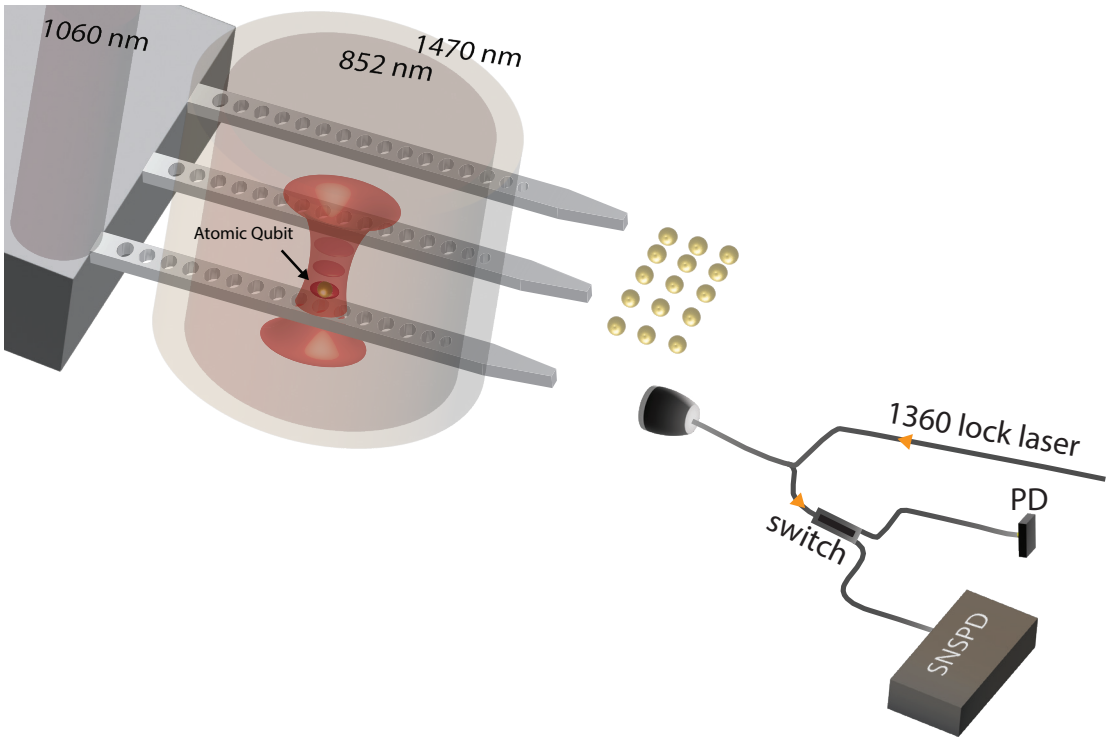

Figure 7.5: An atom from the array is transported onto the cavities fabricated on the chip for single photon emission. A 1060 nm laser beam is focused on the substrate close to the device edge to tune the cavity resonance. A 1360 nm laser, locked to the atomic transition, is used to probe the cavity resonance, and the reflected signal is measured on a photodiode (PD). This signal is then used to feed back on the AOM amplitude to control the 1060 nm laser power to keep the cavity on resonance. A fiber switch is used to move between cavity locking and photon collection on the SNSPD. The 852 nm and 1470 nm laser beams come from the top and excite the atoms to the $7S_{1/2}$ state, from which the atom decays through the cavity.

single photon detector (SNSPD) as shown in Fig. 7.5.

For atoms to interact with the cavity modes, the cavity has to be resonant with the atomic transition. Towards this, we lock the cavity to atomic resonance. We lock a 1360 nm laser to cesium $6P_{3/2}$ to $7S_{1/2}$ transition using saturation absorption spectroscopy. We then use this laser to probe the cavity, measure the cavity reflection, and feed back on the heating laser to keep the cavity on resonance using a side-of-fringe lock. We use an optical circulator to send the probe laser to the cavity while collecting the photons from the cavity on the collection end of the circulator. We use an optical switch to route photons to a low-noise amplified detector for cavity locking vs SNSPD for single photon detection of photons emitted by the atoms.

7.6 Towards telecom single photons; Outlook and future direction

At the time of writing this thesis, an atom array have been established next to the devices presented in this chapter. With the re-establishment of the right z-plane for loading atoms onto the target pancakes and locking the cavity to resonance, interactions between atoms and telecom cavity modes can be established. The atom-cavity coupling is also a function of the exact position of the atom with respect to the cavity mode, as the cavity coupling strength is a function of position and is given by:

$$g(r) = \sqrt{\frac{\mu^2 \omega_c}{2\hbar\epsilon_0 V}} E(r), \tag{7.4}$$

where E(r) is the electric field at the trapping region, normalized to the electric field

maxima of the cavity mode. In our setup, finding the cavity maxima (along the cavity length) can be done promptly, given the ability to have an array of atoms that can load onto the device simultaneously or in a back-to-back fashion.

A key initial application of this would be the generation of single photons from the device. Our normal imaging scheme, when the atoms are coupled to the device, can result in correlated emission of 1360 nm photons into the cavity and 895 nm photons into the vacuum modes, part of which would be collected by the objective and in the EMCCD camera. Using single photon detectors instead of EMCCD can lead to the detection of these correlated photons. Furthermore, coupling more than one atom to the cavity can result in cavity-mediated interaction between the atoms, and can result in interesting correlated features on the photons collected through the cavity [253].

Finally, with the integration of ground-state spin control, pumping, and a pulsed line to bring the atom coherently back from the $6P_{1/2}$ state to $6S_{1/2}$ F=4, the scheme presented in the previous chapter can be directly realized to generate atom-telecom photon entanglement. The scheme can also be extended to generate GHZ, or cluster states, which might be of interest as a photon resource state. While the initial experiments might focus on a single cavity for proof-of demonstration experiments, the schemes can be directly generalized to work in parallel across all the resonant cavities in the field of view of our objective. Multiple cavities can be locked on resonance by multiplexing the cavity locking mechanism described in the chapter. Arrays of 1060 nm lasers can be generated by fiber arrays coupled to AOMs, and the emission from each of the cavities can be mode-matched to a fiber array and routed to detectors.

CHAPTER 8

SCALING QUANTUM NETWORKS WITH ATOMS

8.1 Introduction

In this chapter, we will introduce two different approaches to scale quantum networks and to distribute entanglement at large distances. In the first approach, we will use an array of atoms coupled to a single concentric cavity as our quantum network node. Along with the telecom operation introduced in the previous chapters, we show that this architecture can scale to long distances.

In the second approach, we will introduce a hybrid quantum system. This system combines the capabilities of both atoms and multimode rare earth ensemble memory to deliver a network that can scale to thousands of kilometers. This system enables a hybrid network that combines the capabilities of individual quantum systems to deliver a unique quantum network that can scale to thousands of kilometers.

8.2 A multiplexed network architecture with atom arrays coupled to a cavity

Here, we propose a Yb atoms based quantum network and repeater node architecture that is capable of high-rate, multiplexed entanglement generation, and operating at telecom wavelengths. This architecture is based on arrays [28, 31] of individual neutral ytterbium (Yb) atoms, an alkaline earth-like species [254–256], in large ($\approx 1\,\mathrm{cm}$), near-concentric optical cav-

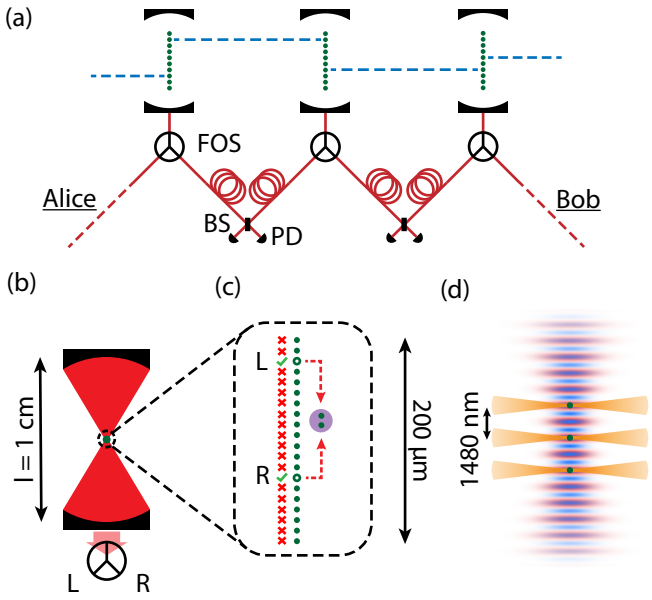

Figure 8.1: **Overview of the network architecture**. (a) Nodes based on arrays of atoms (green circles) in optical cavities generate a Bell pair over each link (blue dashes) to distribute entanglement between end-users Alice and Bob. We employ "heralded" entanglement generation based on photon interference on a 50:50 beamsplitter (BS). Fiber-optic switches (FOS) connect adjacent nodes at will by routing the photons from each cavity. (b) The near-concentric optical cavities have a mirror spacing of ≈ 1 cm while the atom array spans a length of only ≈ 200 μm. (c) The time signature of the photons on the detectors (PD) informs which atoms at each node are in a Bell state (green check marks). Subsequent, deterministic gates can be achieved by moving these atoms (dashed red arrows) and performing Rydberg entangling operations (purple circle). (d) A standing wave in the cavity traps atoms in a one-dimensional array (blue) to overlap with the highest field strength of the telecom mode (red). Atoms are positioned with auxiliary optical tweezers (yellow) that also move the atoms.

ities [257–260] (see Fig. 8.1). We consider a time-bin entanglement generation protocol, similar to the one introduced in previous chapter, that combines a strong, 1.48 μm-wavelength transition [261, 262] and long-lived nuclear spin-1/2 qubit states of ^{171}Yb with temporal multiplexing along the array of atoms.

Based on recent progress with alkaline-earth atomic arrays [204, 254–256, 263–266] and realistic assumptions regarding the operation of these nodes, we show that our multiplexing protocol can generate Bell pairs over $>$ 1000 kilometers within the coherence time of the

qubits, and is compatible with entanglement purification protocols [121, 267, 268] as well as the distribution of many-body states [83, 269–271].

8.2.1 Multiplexed remote entanglement generation

To motivate the proposed architecture, we begin with an overview of our multiplexed time-bin networking protocol. Specifically, we consider the example of a network link of length $L = 100\,\text{km}$. The associated two-way signal transmission time per attempt is $\tau = 2L/c$, where $c = c_0/n$ is the speed of light in optical fiber ($n = 1.4$) that includes both the quantum signal and classical heralding signal; $\tau \approx 1\,\text{ms}$ for this distance. We estimate that ≈ 5800 entanglement attempts will be required if there is only a single qubit (atom) at each node, resulting in a $\approx 0.16\,\text{Hz}$ entanglement generation rate. The attempt time is dominated by signal transmission such that the duty cycle (fraction of time) of entanglement-producing operations is only $\approx 4\%$.

If instead we have $N = 100$ qubits at each node and multiplex their signals as described below, we can drastically decrease the number of required attempts to only ≈ 60 resulting in a ≈ 50-fold increase in the entanglement rate to $8\,\text{Hz}$ at $L = 100\,\text{km}$. In this case, the duty cycle for entanglement-producing operations is $\approx 50\%$. Although the time required per attempt is longer when multiplexing across a large number of atoms, the favorable scaling in success probability per attempt over long network links leads to substantially improved entanglement generation rates compared to the case of a single atom.

8.2.2 Atom arrays in near-concentric optical cavities

The nanophotonic cavities presented in the previous chapters accomplish these goals by having the ability to have a large number of atoms and cavities, allowing for spatial and temporal multiplexing. The architecture presented below presents an alternate approach where arrays of atoms are coupled to a single concentric cavity. This approach overcomes any potential challenges of the nanophotonic cavities that might arise from the integration of the Rydberg interactions [232]

Near-concentric cavities with large mirror spacings ($\ell \gtrsim 1\,\mathrm{cm}$) have recently been used with great success in myriad cavity QED research directions [257–260], and offer enough optical access to enable single-atom control in cavity-coupled atom arrays. Crucially, the mirror spacing is similar to the size of glass cells used in many recent high-fidelity Rydberg entanglement studies [49, 265, 266, 272]. Further, near-concentric cavities are widely used in trapped ion systems [257] that are also sensitive to transient electric fields from dielectric surfaces [273]. Therefore, it is reasonable to expect that these cavities are compatible with deterministic Rydberg-mediated gates and Bell state measurements needed in a quantum repeater and purification architecture.

We focus on a near-concentric system with $\ell = 0.975\,\mathrm{cm}$ and radius of curvature $R = 5\,\mathrm{mm}$ for which the cavity stability parameter $\mathcal{G} = 1 - \ell/R = -0.95$ [258, 274]. ($\mathcal{G} = -1$ defines the concentric limit which is unstable.) We choose a single-sided cavity, where the reflectivity of one mirror is much greater than the other to allow photon passage, with a finesse of $50,000$. We couple this cavity to the $^3\mathrm{P}_1 \leftrightarrow {}^3\mathrm{D}_2$ transition with wavelength $\lambda_{\mathrm{net}} = 1480\,\mathrm{nm}$ and decay rate $\Gamma = 2\pi \times 318\,\mathrm{kHz}$. Based on these parameters, the coupling

strength to the cavity is $g_{34} \approx 2\pi \times 1.53\,\mathrm{MHz}$ and the single-atom cooperativity is $C \approx 16$

We trap the atoms in a standing wave at $\lambda_{\mathrm{trap}} = \lambda_{\mathrm{net}}/2 = 740\,\mathrm{nm}$ to ensure maximal coupling with the telecom field (at λ_{net}) in the cavity [see Fig. 8.1(d)]. The standing wave at λ_{trap} is fortuitously close to the 'magic' wavelength for the optical clock transition ($^1\mathrm{S}_0 \leftrightarrow {}^3\mathrm{P}_0$) where the two states have equal polarizability [275]: $\lambda_{\mathrm{m}} = 760\,\mathrm{nm}$. The expected $1/e^2$ waist radius for this standing wave is $w_{\mathrm{trap}} \approx 14\ \mu\mathrm{m}$; the trap depth (and frequency) are free parameters. Optical tweezers are employed to create an atom array from the magneto-optical trap (MOT) before the standing wave is turned on, and the tweezers are positioned to overlap the desired anti-nodes of the standing wave [see Fig. 8.1(d)]. The standing wave provides strong axial confinement with $\lambda_{\mathrm{trap}}/2$ spacing between the anti-nodes and guaranteed maximal overlap with the anti-nodes of telecom cavity mode at λ_{net}, and the tweezers provide strong transverse confinement.

8.2.3 Atom-photon entanglement via four-wave mixing

We entangle the nuclear spin-1/2 qubit in the ground state of $^{171}\mathrm{Yb}$ with a 1480 nm-photon on the $^3\mathrm{P}_1 \leftrightarrow {}^3\mathrm{D}_2$ transition via a four-pulse scheme that uses two Zeeman states within the $^3\mathrm{P}_1$ manifold as intermediaries [see Fig. 8.2(a)]. The target state of our protocol is the atom-photon Bell state $|\psi\rangle_{\text{atom-photon}} = (|0\rangle_a \left|\lambda_{\text{early}}\right\rangle_p + |1\rangle_a |\lambda_{\text{late}}\rangle_p)/\sqrt{2}$, in which the atomic qubit states $\{|0\rangle_a, |1\rangle_a\}$ are entangled with the photon occupation in an early and late emission time bin $\{\left|\lambda_{\text{early}}\right\rangle_p, |\lambda_{\text{late}}\rangle_p\}$. Such time-bin encoded states are ideally suited for long-distance entanglement distribution via optical fibers as they are robust against birefringence in fibers that would adversely affect other encodings such as polarization-encoded

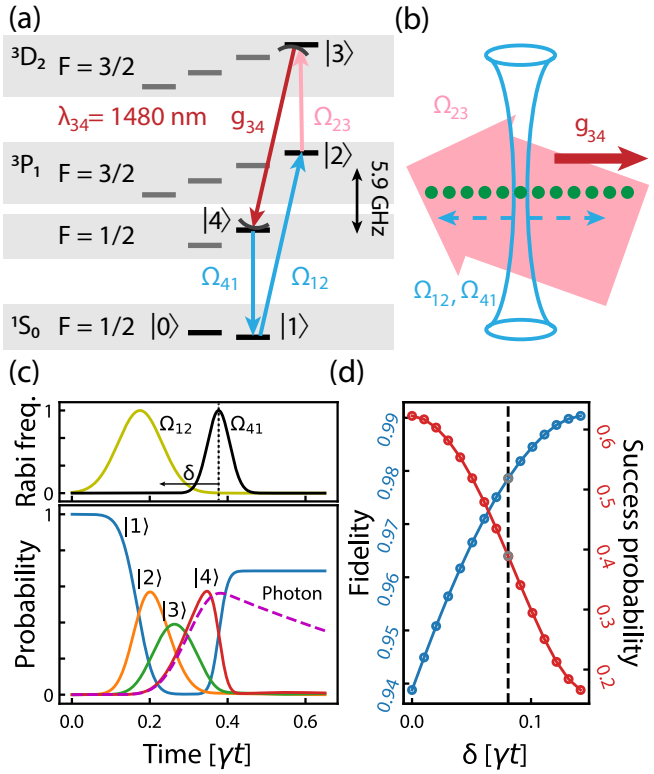

Figure 8.2: **Multiplexed remote entanglement via a four-pulse excitation scheme.** (a) A minimal diagram of the ^{171}Yb level structure showing two hyperfine Zeeman states in the $^3P_1$ manifold as intermediaries. (b) Local application of Ω_{12} and Ω_{41} on an atom-by-atom level is the primary mechanism for our time-based multiplexing scheme. (c) Analysis of the pulses and internal dynamics during the process as well as the temporal shape of the extracted photon that is entangled with the nuclear qubit in the ground state. The black arrow highlights that the relative timing of the two pulses Ω_{12} and Ω_{41} is a free parameter. The maximum Rabi frequencies of these pulses are $\{\Omega_{12}^{\max}, \Omega_{34}^{\max}\} = \{13.2\gamma, 23.0\gamma\}$ and $\gamma = 2\pi \times 180\,\text{kHz}$ is the decay rate of $^3P_1$. (d) The resulting atom-photon entanglement fidelity and success probability vs the relative timing δ of Ω_{12} and Ω_{41} in units of γ. [(c) corresponds to $\delta = 0$.] We choose δ as shown in the black dashed line for the remainder of this work.

states. To create $|\psi\rangle_{\text{atom-photon}}$ we start by preparing a superposition of the atomic qubit states $(|0\rangle_a + |1\rangle_a)/\sqrt{2}$. Then a coherent atomic pulse sequence results in the emission of a photon into the cavity mode only if the atom is in $|1\rangle$. The proposed four-level system that allows such a state selective emission is shown in Fig. 8.2(a), and was inspired by similar sequences that have recently been considered for alkali species [205], and described in Chapter

5. After the emission in the early time bin, a $\pi-$pulse on the qubit states flips $|0\rangle_a$ and $|1\rangle_a$, and a second optical pulse sequence causes emission in the late time bin. This completes the protocol and leaves the system in the target state $|\psi\rangle_{\text{atom-photon}}$.

We leverage the $F = 3/2$ and $F = 1/2$ hyperfine structure of the $^3\text{P}_1$ manifold to provide the well-separated intermediate states $|2\rangle$ and $|4\rangle$, and we assume a magnetic field of $B \gtrsim 100$ G although this is not strictly necessary. Note that we expect $\lesssim 10^{-4}$-level field homogeneity across the array [276, 277], corresponding to ~ 10 kHz-level shifts of the telecom transition. These shifts are the % level of the photon bandwidth, and are mitigated by pairing atoms in identical locations within their respective arrays, thus experiencing similar local environments. We apply Gaussian pulses Ω_{12} and Ω_{41} on a per-atom basis within the array [Fig. 8.2(b)] as the primary mechanism for our time-based multiplexing scheme. Ω_{23} and g_{34} couple to all atoms globally, but are distantly off-resonant with negligible differential effect on the qubit $|0\rangle - |1\rangle$ when Ω_{12} and Ω_{41} are not applied to the atom. Hence, we raster the tightly-focused Ω_{12} and Ω_{41} beams across the atoms such that the position of the atom in the array is mapped to the time-stamp of the photon emitted into the cavity.

The pulse scheme is similar to the one described in Chapter 5, and is shown in Fig. 8.2(c). We leave Ω_{23} at a constant value for the entire duration of the four-wave mixing (FWM) protocol. We then transfer population from $|1\rangle$ to $|2\rangle$ with Ω_{12}. These two fields populate $|3\rangle$, which is transferred to $|4\rangle$ by the coherent cavity coupling g_{34}. Note that other schemes for transferring population from $|1\rangle$ to $|3\rangle$, such as a two-photon π-pulse detuned from the intermediate state $|2\rangle$, are expected to further suppress double-excitation due to decay during the first half of the FWM protocol to below 1%. We then perform Ω_{41} to co-

herently transfer the atomic population back to $|1\rangle$. The relative timing of the Ω_{12} and Ω_{41} pulses introduces a trade-off between process fidelity and success probability [Fig. 8.2(d)]. Essentially, the process is limited by spontaneous emission from $|4\rangle$ which occurs at a rate $\Gamma_{41} \approx 2\pi \times 180\,\mathrm{kHz} \approx g_{34}/8.5$. Moving the Ω_{41} pulse earlier mitigates the decay but reduces the probability of success. Note that the remote entanglement scheme is heralded, so events that do not produce photons only affect success rates, while events that produce photons but leave the atom in the wrong state are classified as successful and lead to infidelity. We choose the values shown in Fig. 8.2(d) for which the fidelity (success probability) of producing $|\psi\rangle_{\text{atom-photon}}$ with the photon in the fiber is ≈ 0.98 (≈ 0.39).

8.2.4 Entanglement distribution using quantum repeater nodes

We now return to the discussion of entanglement distribution rates for our multiplexed scheme and we begin by considering a single link between two nodes. For distances larger than $\approx 20\,\mathrm{km}$, we find a drastic improvement of the entanglement rate as more atoms per node are used. At a distance of 100 km we see a ≈ 50-fold faster rate when using 100 atoms per node compared to the single-atom case. We find that the entanglement rate sees diminishing returns for $N \gtrsim 200$ due to two main factors. First, the probability of successfully creating a Bell pair asymptotically saturates at 1 such that larger numbers of atoms are not needed for suitably large rates. Second, the time per entanglement attempt becomes dominated by the total time required to perform the four-wave-mixing protocol for all the atoms at each node, rather than the classical signal transmission time between them

We now turn to the use of intermediate repeater nodes to extend the range of entanglement generation to greater distances. The goal is to connect these intermediate links into a larger chain which we refer to as the "network-level" architecture. We break the length L between end-users Alice and Bob into 2^m segments with length $L_m = L/2^m$, where m is a non-negative integer we call the "nesting level" of the network.

8.2.5 Repeater protocol

We divide the intermediate links into two groups in alternation such that adjacent links are not in the same group [see Fig. 8.3(a)]. Our protocol is based on the generation of Bell pairs across all Group 1 links in parallel followed by all Group 2 links in parallel. Naively, the mean time required to generate Bell pairs across all links is approximately twice the mean time required for a single link. However, the number of attempts required to successfully create entanglement follows a geometric distribution and both groups must wait for the success of *all* constituent links. Hence, we stochastically sample the distribution of attempts for each link in both groups in order to estimate mean entanglement generation rates at the network level. Note that if N atoms are employed in the multiplexed entanglement generation in Group 1, $N-1$ atoms are available for generating entanglement in Group 2.

After the Bell pairs have been generated on Group 1 links, the constituent atom at each node in these Bell pairs – recognized by its time stamp – must be isolated and preserved from the subsequent operations on the Group 2 links. Our protocol is based on transferring those qubits from the nuclear spin-1/2 ground state ($^1\mathrm{S}_0$) to an auxiliary computational basis [278] of the nuclear spin-1/2 metastable clock state ($^3\mathrm{P}_0$) that has a lifetime of $\approx 20\,\mathrm{s}$.

Accordingly, we leverage the (nearly-)clock-magic wavelength of the cavity standing wave-optical tweezer trap system. The metastable clock state is transparent with respect to the four-wave mixing sequence and a negligible relative phase is anticipated on this auxiliary qubit. We expect that transferring the qubit to the auxiliary basis will occur at a rate much faster than the entanglement generation rates over distances of interest and therefore have a negligible effect on the total rate. Rates of $\Omega_{\text{clock}} \approx 2\pi \times 100\,\text{kHz}$ and a transfer fidelity of $\gtrsim 0.99$ are anticipated with ^{171}Yb [279]. Alternatively, the atom(s) could be moved away from the array and the laser fields to preserve coherence during Group 2 operations.

With Bell pairs across all neighboring links, we now complete the end-to-end entanglement protocol by entangling atomic pairs and performing deterministic Bell-state measurements at each node to effectively reduce the nesting level of the network by 1. Bell pairs between increasingly distant nodes are traced out of the system through this process until end-users Alice and Bob directly share a Bell pair. We couple to highly-excited Rydberg states to perform the required local deterministic entanglement operations [49, 265, 272], inspired by a recent approach with alkaline-earth atoms coupling from the clock state to Rydberg states in the $^3S_1$ series [265]. However, this interaction occurs only over short distances, requiring the atomic pairs to be re-positioned [see Fig. 8.1(c)]. The optical tweezers will remove the atoms from the cavity standing wave and translate them to within several microns of each other prior to Rydberg excitation. Tweezer-mediated coherent translation of atomic qubits over such distances is routinely performed on the $\sim$ ms timescale with minimal decoherence [168, 281–283] and Rydberg-mediated gates are on the $\lesssim \mu$s timescale [49, 265, 272]. These steps are again much faster than the entanglement distribution rates and

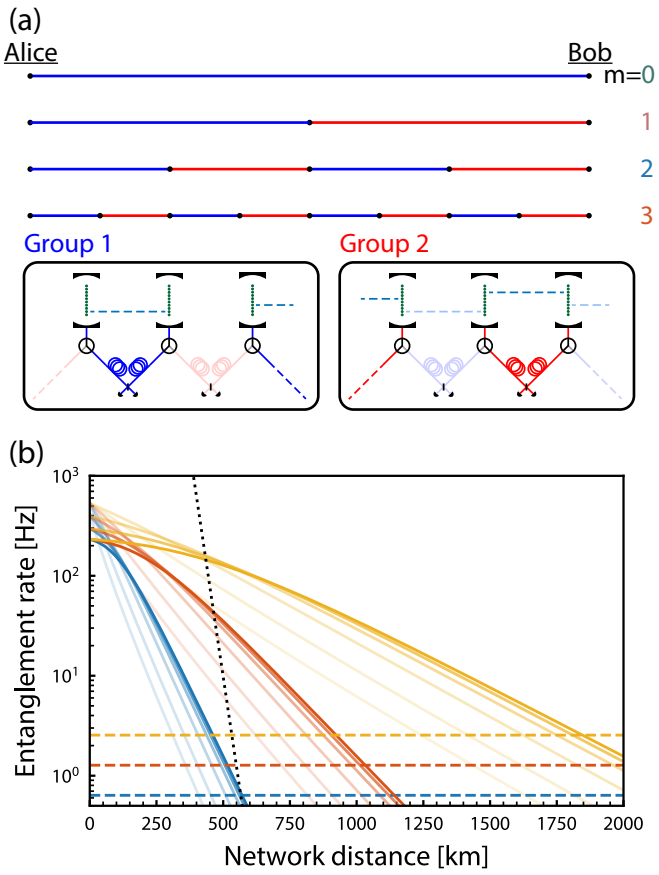

Figure 8.3: **Network-level entanglement generation**. (a) In order to distribute entanglement to end-users Alice and Bob over greater distances, $2^m - 1$ intermediate repeater nodes are used, where m is the nesting level. Bell pairs are generated in parallel within Group 1 (blue) and Group 2 (red). Intermediate nodes have two atoms involved in Bell pairs. (b) Simulated entanglement distribution rates over the full network versus the network length L for nesting levels $m = 2$ (blue), 3 (orange), and 4 (yellow). various numbers of atoms N is shown as an opacity scale for N=10,20,50,100,150,200 with N=200 being fully opaque. The dashed lines again show conservative estimates of the coherence of the qubits at each nesting level. Note that the number of qubits depends on m, so the estimated coherence is $2^m/(2\pi T_2)$. The black dotted line shows for comparison the direct entanglement distribution rate by sending entangled photon pairs at a rate of 10 GHz [280].

are only performed when remote Bell pairs have been successfully created, so we can neglect their effect on the total rate. The expected near-term fidelity of Rydberg-mediated gates and local measurement is $\gtrsim 0.99$ [204, 265], which is high compared to the fidelity of generating Bell pairs: $\approx 0.98^2 = 0.96$ [see Fig. 8.2(d)]. A detailed network fidelity budget is outside the

scope of this work.

8.2.6 Summary of the results

We consider the network-level entanglement distribution rate based on this protocol for varied network length L, nesting level m, and atom number per node N. We compare this rate against a conservative estimate of the coherence of *all* qubits in the system. Naturally, this depends on the nesting level, and hence the network level coherence estimate is $\Gamma^m_{\text{coherence}} = 2^m/(2\pi T_2) = 0.16 \times 2^m$ Hz. Figure 8.3(b) shows the network level generation rate versus the network length for nesting levels $m = 2$, 3, 4 with various atom numbers per node N shown as an opacity scale. We also compare against direct communication (without intermediate nodes) based on entangled photon pairs at a wavelength of 1550 nm with a repetition rate of 10 GHz [280]. The direct communication rate falls sharply, passing below our coherence time estimates at a distance of ≈ 600 km. We find that the achievable network length increases for higher nesting levels and saturates for $N \approx 200$ atoms. In particular, for $m = 4$ our system enables a network of $L \approx 1500$ km.

8.2.7 Outlook and conclusion on multiplexed atom-array based repeater architecture

We have proposed a platform that combines the strengths of neutral atoms – efficient light-matter interfaces [146, 284–286] with telecom operation [205, 233, 261], high-fidelity qubit operations and measurement [49, 204, 265, 272], scalability to many qubits [270, 287, 288], and long coherence times in state-independent optical traps [263, 264, 279] – for the first time

to enable new directions in quantum communication and distributed quantum computing. Moreover, we have demonstrated how this platform can offer dramatic improvements in entanglement generation rates over long distances by temporal-multiplexing across an array of atoms within each entanglement generation attempt.

We show that entanglement generation rates with $N \approx 100$ atoms across $\gtrsim 100\,\text{km}$-links compare favorably with conservative estimates of the atoms' coherence time. We further demonstrate that multiplexed repeater-based networks with $2^{(m=4)}$ links and $N \approx 100$ atoms at each node can generate entanglement over $\approx 1500\,\text{km}$. Additionally, we show that our system is well-suited for entanglement purification [121, 267, 268], providing a promising architecture for a transcontinental quantum network.

More generally, the confluence of the associated research thrusts – Rydberg atoms arrays [287, 289], cavity QED with strong atom-photon coupling [146, 284, 285], and atom-array optical clocks [263, 264, 279] – into one platform will enable new methods to engineer, measure, and distribute many-body entangled states with single-qubit control. For example, the optical cavity can mediate non-demolition measurements [290, 291] that could augment the Rydberg-based quantum computing platform. Conversely, Rydberg-mediated interactions and single-atom control may help to enhance and distribute spin-squeezed states of optical clock qubits generated via the cavity [269, 292, 293]. Finally, the marriage of short-ranged (Rydberg-mediated) and infinite-ranged (cavity-mediated) interactions combined with the possibility of atom-selective control and readout will enable new opportunities for the study of quantum many-body phenomena such as the simulation of magnetism [259] and chaotic dynamics [271] in regimes not readily accessible to classical computers.

8.3 Hybrid quantum system based repeater architecture

Here, we propose to combine ensemble-based quantum memories with single-spin photon transducers to enable a near-term hybrid quantum repeater with large scale multiplexing, efficient photon generation, and near-deterministic entanglement swapping. In our scheme, a single-spin photon transducer is used for high-rate generation of entangled photon pairs where, for each pair, one photon is to be stored in a multi-mode ensemble-based memory in a repeater node and the other to be transmitted through a fiber to generate distant entanglement over the elementary segment between the nodes. Successfully entangled stored photons are read out from the memories, and near-deterministic entanglement swapping can be accomplished with the aid of extra single-spin photon transducers, thereby extending entanglement over neighboring elementary segments.

Furthermore, we outline a specific implementation with cavity-coupled single Rb atoms and Tm-doped crystal memories. We show how a single Rb atom coupled to two nanophotonic cavities with visible and telecom resonance frequencies, respectively, can function as a robust photon-pair source producing entangled visible and telecom photons. The telecom photon can propagate in standard optical fibers with minimum loss, and the visible photon is compatible with the resonance of the Tm-doped crystal. Thus, no frequency conversion is required for the repeater. We simulate the performance of the repeater for quantum key distribution and show that rates of tens of secret bits per second over distances of up to 1000 km can be achieved with up to 9 repeater stations, each containing only two ensemble-based memories and four single Rb atoms. Further increase of the rate is possible through

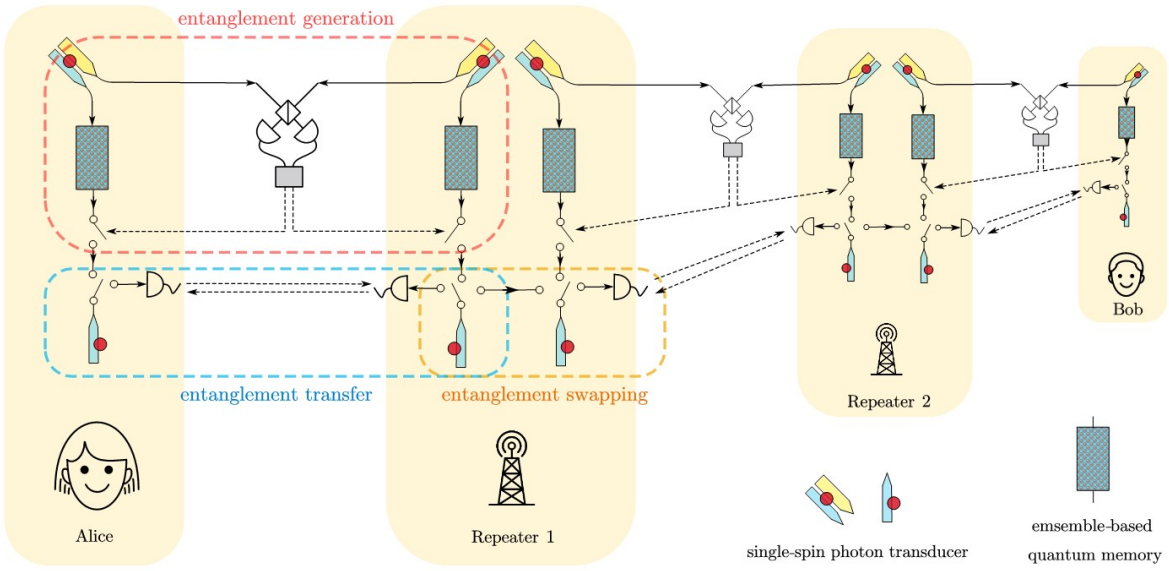

Figure 8.4: Structure of the quantum repeater chain architecture. The whole system contains two end-nodes, Alice and Bob, connected by a series of repeater nodes. This figure depicts an example with two repeater nodes showcasing the key components involved. The yellow blocks represent the repeater nodes with the local devices depicted within. The protocol involves three main steps: entanglement generation, entanglement transfer, and entanglement swapping, as circled with dashed lines in different colors in the figure. The whole protocol harnesses two kinds of devices as the key components – the single-spin photon transducers and the ensemble-based quantum memories. The others are common devices, including 50-50 optical beam splitters, photon detectors, and optical switches, as sketched with conventional symbols in the figure. The solid-line arrows represent the optical fibers and the dashed-line arrows the classical channels. Both the end nodes and the repeater nodes have symmetric layouts.

additional multiplexing.

8.3.1 Structure of the Repeater Chain Protocol

The general structure of the quantum repeater, composed of the single-spin photon transducers and ensemble-based quantum memories, is depicted in Fig. 8.4. The protocol is designed to distribute entanglement between two distant end nodes, Alice and Bob. It divides the total distance between Alice and Bob into multiple segments. In each segment, we

use photon transducers to repeatedly emit entangled photon pairs on each side, storing one photon from each pair in the ensemble-based memories and attempting heralded entanglement generation over the segment with the other photons. Upon success, the now entangled photons are retrieved from the memories on each side and mapped into single-atom systems in a heralded fashion. This is followed by entanglement swapping using local Bell measurements to generate entanglement between Alice and Bob. The protocol thus consists of three main steps: entanglement generation, entanglement transfer, and entanglement swapping as circled separately in Fig. 8.4.

For the initial entanglement generation step, as shown within the dashed red boundary in Fig. 8.4, two identical single-spin photon transducers are employed to produce entangled photon pairs continuously. For each photon pair, one of the photons is to be stored in the multi-mode ensemble-based quantum memory while the other is sent via optical fiber to the middle station. At the middle station, a linear optics Bell measurement is performed to entangle the photons stored in the quantum memories. While the success of this operation is probabilistic and subject to photon loss, information about which photon pairs were successfully entangled is sent back from the middle station to the nodes where quantum memories are located. The successfully entangled photons will be read out from the memories for further processing, while the failed ones will be discarded.

As illustrated in the area enclosed with the dashed blue line in Fig. 8.4, the successfully entangled photon pairs read out from the Tm-memories are transferred into the single-spin photon transducer systems. The entanglement is swapped from the photons to the spins by means of a cavity-mediated controlled phase gate [148, 291], which also heralds successful

retrieval of the photons from the Tm-memory. The heralding signals are sent between the nodes to confirm the successful transfer. Once confirmed, the successfully entangled spins will be stored until entanglement swapping can take place with the neighboring link. Unsuccessfully entangled spins will be reset to attempt the next photonic transfer. Note that we employ separate spin systems for each memory to ensure that the unsuccessful retrieval of a photon from one memory does not influence the already successfully stored photon from the other.

Lastly, for the entanglement swapping between neighboring sections, one has to implement a Bell state measurement between the two adjacent spins in one repeater node. In this case, one can let one of the spins re-emit a photon, guide it to interact with the other spin, and finally, detect the photon and both spins in certain bases, as sketched in Fig. 8.4 within the dashed orange rounded rectangle. This operation is deterministic up to local losses.

Below, we outline a concrete implementation of this protocol with trapped single neutral Rb atoms and Tm-doped crystal quantum memory (Tm-memory) and assess its performance.

8.3.2 Rb entangled-Photon emitter and entanglement generation protocol

The Rb entangled-photon emitter consists of a single neutral Rb atom trapped with optical tweezers and coupled to two nanophotonic cavities, one with resonance wavelength at 1470 nm and the other at 795 nm. There have been previous designs for two-mode cavity coupling of emitters with crossed cavities or using both TE and TM modes in a waveguide [294, 295]. It is however challenging for such setups to maintain the required cavity quality factor while increasing the frequency separation of the two modes, which, in our case, corresponds to a

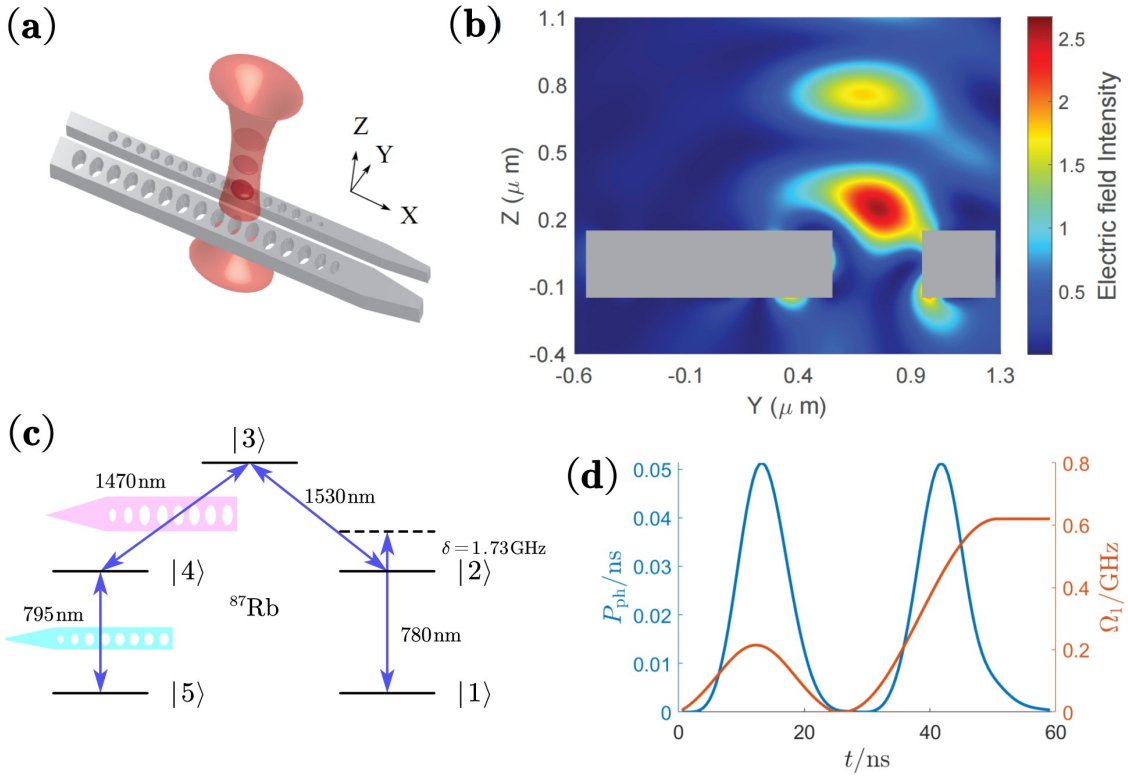

Figure 8.5: Rb emitter design and mechanism. (a) Parallel dual cavity design. The wide and narrow gray strips placed along the X direction represent the nanophotonic cavities resonant with the telecom and visible photons emitted from the Rb atom, respectively. They are of a TE mode telecom wavelength cavity (1470 nm) and a TM mode visible wavelength cavity (795 nm) both with a refraction index of 2.6 and a thickness of 300 nm. The light-red cone denotes the combination of the incident and reflected trapping lights, forming antinodes of high light intensity marked as dark red. The Rb atom is trapped in the nearest node to the cavities. (b) The slice of the simulated relative electric field intensity of the trapping light of the Z-Y plane centered around the trapping light position. It is normalized to the incident tweezer beam intensity. The two solid gray rectangles indicate the two nanophotonic cavities viewed from the X direction. (c) The intended driving path, from $|1\rangle$ to $|5\rangle$, in the Rb atom. The first two couplings are laser-induced and the later two are cavity-induced. There is a detuning $\delta = 1.73$ GHz respecting the $|1\rangle - |2\rangle$ energy difference in the first laser driving. (d) Temporal profile of the driving pulse of the first laser (orange) and emitted telecom and visible photons (blue).

wavelength difference of 675 nm.

Instead, we propose a parallel-cavity arrangement with the Rb atom located on the top of the two cavities, as shown in Fig. 8.5(a). Such an architecture enhances the independence of the two cavities and is feasible by integrating atoms with on-chip nanophotonic cavities [196, 296]. However, there are still many issues that need to be considered for choosing suitable system parameters. On one hand, we need both cavities to be close enough to each other to reflect the tweezer light to form a stable trap for the Rb atoms [162, 167]. In addition, placing the cavities closer to each other also provides larger atom-cavity coupling strengths, resulting in Purcell-enhanced emissions into the desired cavity mode. On the other hand, as the cavities of 1470 nm and 795 nm get closer, photonic modes can leak into each other, reducing the achievable quality factors.

We address these challenges by carefully selecting the material with the optimum refractive index, cavity separation, and cavity thickness. In our design, we chose silicon-enriched silicon nitride, SiN, as the cavity material with a refractive index of 2.6. This selection enables better mode confinement compared to stoichiometric Si_3N_4, allowing for minimal separations between the cavities while maintaining high cavity quality factors. Similar high quality-factor cavities have been proposed and fabricated in silicon-enriched silicon nitride [297–299]. For practical fabrication considerations, both cavities are assumed to have a thickness of 300 nm. We perform simulations with a 1060 nm tweezer and 400 nm separation between the cavities and present the results in Fig. 8.5(b). Our findings demonstrate that this design enables the 1470 nm telecom-photon cavity to achieve a quality factor of 1.4×10^5 with an average cooperativity of 34 with the Rb atom, while the 795 nm visible-photon cavity

reaches a quality factor of 3.8×10^5 with an average cooperativity of 11.

We will now describe in detail how this Rb-dual-cavity setup can function as a source of entangled photon pairs with the two photons at telecom and visible wavelengths, respectively. To achieve this, we harness five specific electronic orbital states from the ^{87}Rb atom. They are: $|1\rangle$: $5^2\mathrm{S}_{1/2}|F=2, m_F=2\rangle$, $|2\rangle$: $5^2\mathrm{P}_{3/2}|F=3, m_F=3\rangle$, $|3\rangle$: $4^2\mathrm{D}_{3/2}, |F=3, m_F=3\rangle$, $|4\rangle$: $5^2\mathrm{P}_{1/2}, |F=2, m_F=2\rangle$, and $|5\rangle$: $5^2\mathrm{S}_{1/2}, |F=1, m_F=1\rangle$. Fig. 8.5(c) shows the coupling and driving of these five levels. In each photon emission cycle, we initialize the Rb atom in state $|1\rangle$ and drive it first to the $|2\rangle$ state with the first laser and then to the $|3\rangle$ state with the second laser. From the $|3\rangle$ state, the Rb atom will decay initially to the $|4\rangle$ state emitting a photon into the telecom cavity mode (1470 nm), followed by another decay to the $|5\rangle$ state emitting a second photon into the visible cavity mode (795 nm).

The second laser is continuously driving the transition $|2\rangle \leftrightarrow |3\rangle$ at a Rabi frequency of the same order as the cavity couplings; however, the Rabi frequency of the $|1\rangle \leftrightarrow |2\rangle$ drive is chosen to be about an order of magnitude lower. Besides, the pulse of the $|1\rangle \leftrightarrow |2\rangle$ drive is modulated with a pause in the middle of the driving process as shown by the orange curve in Fig. 8.5(d). The paused driving is calibrated such that the telecom and visible photons have equal probabilities of being both generated in the early time-bin (λ_E) and the late time-bin (λ_L), as shown by the blue curve in Fig. 8.5(d). Ideally, this results in an entangled state of the form:

$$\psi_{\mathrm{vt}} = \frac{1}{\sqrt{2}} \left(|\lambda_\mathrm{E}\rangle_\mathrm{v} |\lambda_\mathrm{E}\rangle_\mathrm{t} + |\lambda_\mathrm{L}\rangle_\mathrm{v} |\lambda_\mathrm{L}\rangle_\mathrm{t} \right), \tag{8.1}$$

where the subscripts refer to the visible (v) and telecom (t) photons. We note that the Rb

atom is not entangled with the final photonic state and can repeatedly emit states of the form above.

In each elementary segment, both end nodes are equipped with Rb emitters. The visible photons generated by the two Rb emitters are directly stored in quantum memories within the nodes, while the telecom photons are to be sent via optical fiber to a middle station. At the middle station, a beam splitter is used for erasing the which-way information, and photon detectors after the beam splitter are used to tell in which time-bins the two photons arrive. In this way, with a maximum probability of 50% for the photon detectors to detect an early as well as a late photon, it ideally projects the two visible photons into a maximally entangled state

$$\psi_{\mathrm{vv}} = \frac{1}{\sqrt{2}} \left(|\lambda_{\mathrm{E}}\rangle_{\mathrm{vl}} |\lambda_{\mathrm{L}}\rangle_{\mathrm{vr}} \pm |\lambda_{\mathrm{L}}\rangle_{\mathrm{vl}} |\lambda_{\mathrm{E}}\rangle_{\mathrm{vr}} \right), \tag{8.2}$$

where the subscripts "l" and "r" denote the left and right ends and the $\pm$ sign is determined by whether the same detector (+) or different detectors (-) measure a photon in the early and late time bins. This allows one to realize the heralded entanglement generation in each segment in a multiplexed fashion.

8.3.3 Rare-earth quantum Memory

In our proposal, multimode quantum memories (QMs) require an ensemble-based approach [300, 301]. Several possible methods exist, including electromagnetically induced transparency (EIT) [302], and photon-echo-related approaches [303], including the atomic frequency comb (AFC) protocol [304, 305]. Relevant hardware includes alkaline atoms [306–310] and rare-

earth-ion-doped crystals (REID crystals) [311–314]. While the transition of Rb vapor or laser-cooled Rb is naturally resonant with the emission wavelengths of photons from a single Rb atom, here we focus on the use of REID crystals. The reason is three-fold. Firstly, the multiplexing potential of the AFC quantum memory protocol includes spectral, temporal, and spatial multiplexing. Secondly, the 2-level AFC protocol in Tm-doped memory is noiseless, since atomic decoherence translates into a reduced readout efficiency rather than a reduction of the (post-selected) fidelity. Thirdly, some Tm-doped crystals have matching resonance lines with ^{87}Rb, with the example of Tm-doped $LiNbO_3$(Tm:$LiNbO_3$)

8.3.4 Simulated performance of the repeater chain

To assess the performance of the quantum repeater chain, we conduct an in-depth simulation to determine the secret key rate achievable when applied to quantum key distribution (QKD). Through a Monte-Carlo simulation, we track the successful entanglement generation, transfer, and swapping events throughout the repeater chain, allowing for accurate modeling of finite memory time effects on the quality of the entanglement. For each data point, we did 100 independent simulations. In each simulation, we simulate the time, T_i, it takes to successfully establish end-to-end entanglement 1000 times. From this, we estimate the average rate of entanglement distribution as $r_i = 1000/T_i$ for the ith simulation. This is then further averaged over the 100 independent simulations such that our final estimate of the average entanglement distribution rate is $R_{\text{suc}} = \sum_{i=1}^{100} r_i/100$. Detailed calculations of the secret key rates are given in reference [104].

As mentioned in section 8.3.2, we assume that the Rb emitter has a repetition rate of

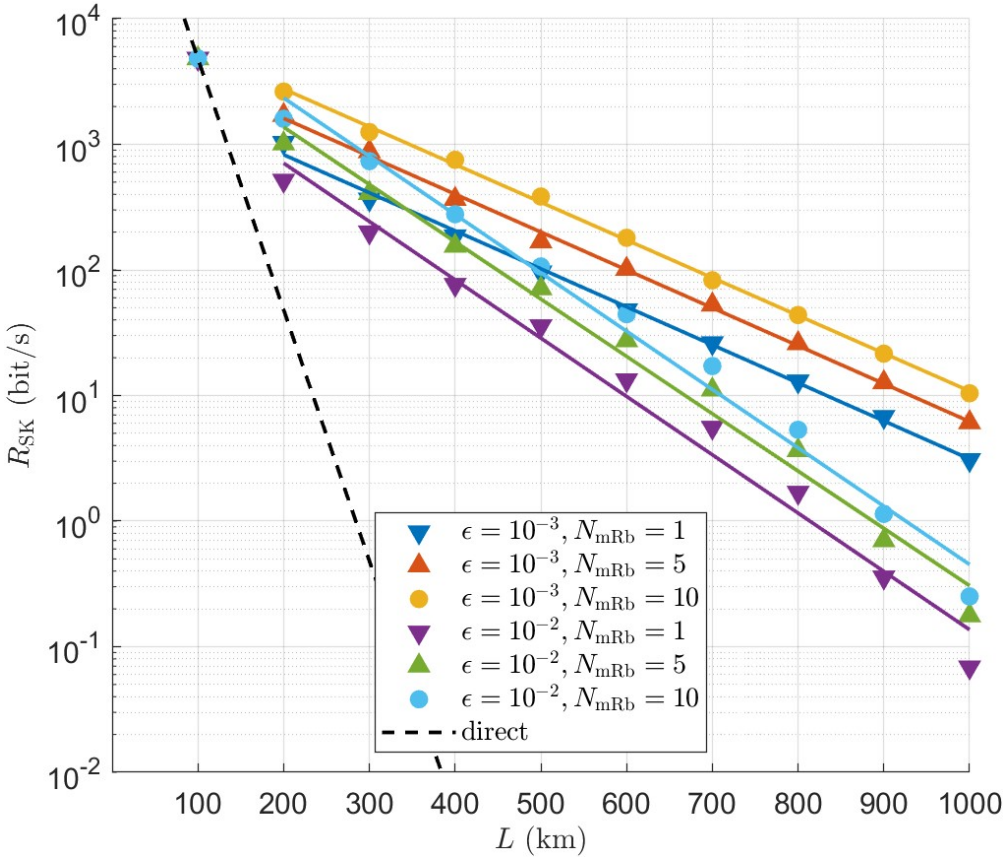

Figure 8.6: Average secrete key rate (R_{SK}) as a function of distance (L) for different entanglement swap error probability (ϵ), and number of auxiliary Rb memory atoms (N_{mRb}). Note that the total number of Rb memory atoms in each repeater station is $2N_{\mathrm{mRb}}$. The dashed black line presents the secret key rate with no repeaters but only a direct link between the two end notes. The solid lines are linear fits excluding the data points for L=100 km.

$\nu_{\mathrm{eRb}} = 1$ MHz, producing entanglement pairs of fidelity 0.98. The fiber attenuation rate for the telecom photon is 0.2 dB/km, and the speed of light in the fiber is $\mathrm{c} = 2 \times 10^5$ km/s. In addition, the single photon detection efficiency is set to be 0.99. The retrieving rate of the Tm-memory as a function of storage time t is $R_{\mathrm{rtr}} = \exp(-4t/2.6\mathrm{ms})$. We calculate the total efficiency of the Tm-memory as $R_{\mathrm{rtr}}\eta^2$, where η is the coupling efficiency from/to fiber. For our simulations, we have assumed $\eta = 0.95$. In addition, we assume that the transfer of the outcoupled photons to Rb atoms has an efficiency of 0.95, which includes optical circuit loss and imperfect photon detection efficiency. The coherence time of the hyperfine levels of the individually trapped Rb atoms is set to 1s. The local entanglement swap has an operation time of 200 ns and a success rate of 0.92, which is a combination of 0.97 efficiency of emitting a photon from one of the Rb-atoms (assuming a cooperativity of 30) and a total efficiency of 0.95 for entangling with the other atom following the entanglement transfer process. To examine the repeater performance under different entanglement swapping error rates, we simulated two cases with the error probability being $\epsilon = 10^{-2}$ and $\epsilon = 10^{-3}$. Thus, with probability $1 - \epsilon$, the entanglement swap operation is perfect while with probability ϵ, the swapped state is completely mixed.

In addition, instead of the case with only one Rb photon transducer for entanglement transfer at each end of each segment as shown in Fig. 8.4, we also simulate cases where multiple (N_{mRb}) Rb photon transducers are used. This provides a second level of multiplexing for the entanglement swapping.

Fig. 8.6 shows the simulated average secret key rates R_{SK} as a function of the total distance L for various N_{mRb} and errors ϵ due to imperfect entanglement swapping. We

optimize the number of repeaters in the chain N_{rep} and the cutoff time t_{cut} to achieve the highest secret key rate per elementary segment, i.e., $R_{\text{SK}}/N_{\text{seg}}$ with $N_{\text{seg}} = N_{\text{rep}} + 1$. We find that for a Rb spin coherence time of 1 s, a cutoff time of $t_{\text{cut}} = 10$ ms is approximately optimum in all simulations. The optimum number of repeater stations (Nrep) used for each data point in Fig. 8.6 can be found in reference [104].

Our simulation shows that secret key rates on the order of 10 bit/s and 1 bit/s can be achieved over 1000 km for entanglement swapping error rates $\epsilon = 10^{-3}$ and $\epsilon = 10^{-2}$, respectively. We have also assumed that the Tm-memories have sufficient multiplexing capacity to ensure the continued operation of the repeater. This means that the number of memory modes needs to be $N_{\text{mode}} = \nu_{\text{eRb}} \frac{L}{N_{\text{seg}} c}$. Based on the total distances and the optimum number of repeaters, N_{mode} ranges from 167 to 625 in the cases we simulated. The entanglement distribution rate could be further increased by increasing the number of Rb-atoms both in the repeater nodes and if more Rb-atoms were used in the entanglement generation step to increase the repetition rate of the entangled photon pairs.

8.4 Discussion and outlook on the hybrid repeater architecture

In summary, we have proposed a hybrid quantum repeater employing single-spin photon transducers and ensemble-based photonic memories to achieve high-rate entanglement distribution over large distances. The hybrid architecture directs the massive multiplexing necessary for battling transmission loss in the optical fibers to the ensemble-based memories, while efficient and near-ideal photon pair generation and entanglement swapping are enabled by the single-spin photon transducers. Furthermore, we provided a specific example

utilizing Rb atoms coupled to nanophotonic cavities as single-spin photon transducers and Tm-doped crystal as ensemble-based memories for massive multiplexing.

The overall framework presented here is relevant to other combinations of hardware besides the specific example analyzed in this work. Efficient single-spin photon transducers can be realized with diamond defect centers [315] and quantum dot systems [316], which can be matched with other ensemble-based memories based on AFC [304], Raman [317] or EIT [302] storage using impurity-doped crystals [314, 318] or atoms, either laser-cooled or at room temperature. We note that different hardware combinations may require frequency conversion to be compatible, which can be achieved through standard techniques based on non-linear waveguides [315, 319–321]. We have focused on the combination of the Rb entangled photon source with Tm-doped crystal memories due to their significant multiplexing potential. However, another interesting extension of this work would be to consider the combination of the entangled photon source with cold Rb atomic ensembles [322] in our repeater framework.

While combining different hardware is arguably more complex than a single hardware repeater, the overall requirements for reaching high-rate entanglement distribution may be substantially relaxed as demonstrated in this work. We thus believe that further investigations of hybrid repeater architectures where ensemble-based memories are combined with single quantum emitters are a promising direction for future work. In particular, employing more complex operations such as entanglement purification techniques [121] to boost the fidelity could be envisioned through the quantum logic enabled by the single-spin photon transducers.

CHAPTER 9

OUTLOOK

In this thesis, we demonstrate a platform that combines the capability of a scalable atom array platform with that of a scalable cavity array platform. We show that we retains some of the fundamental capabilities of atom arrays, such as scalability, rearrangement, single-shot readout using EMCCD camera, while enabling a photonic chip within microns away from the array. While the atom array operation is agnostic to the kind of photonic devices on the chip, we present the chip with hundreds of nanophotonic cavities on it. We show that we can take atoms from the array and move them on top of the photonic cavities, where GHz-level atom-photon interaction strengths are expected. Moreover, we show that we can image atoms, while they are trapped on top of the photonic devices, enabling new control capabilities. We demonstrate these capabilities in a compact stainless steel vacuum chamber with a minute-long lifetime for atoms in the array. With the incorporation of Rydberg interactions, this can potentially combine deep Rydberg-based quantum circuits and quantum networking on the same platform.

We further introduce schemes to make use of excited state atomic transitions to generate atom-photon entanglement. We show that high-fidelity telecom photons entangled with the atoms can be generated using this scheme for multiple atomic species that do not have ground state telecom transitions. We then introduce our new photonic chip with resonant cavity arrays that can be used to realize this scheme. We show up to fourteen cavities in our field of view that can be brought to atomic resonance with our tuning capability, and how

this can be leveraged to generate single photon sources.

Finally, we introduce two schemes where atoms in cavities can be leveraged to create large multiplexed quantum networks. We show that atom arrays coupled to cavities can be used to distribute entanglement across more than a thousand kilometers. Further, we also introduce an atom coupled to two nanophotonic cavities can be used as a deterministic photon pair source. We then demonstrate how a hybrid quantum systems combining this deterministic photon pair source with rare-earth memories can be used to create novel quantum network protocols that outperform individual system capabilities.

The work presented in this thesis combines many desired properties of a quantum network node in a single platform. With massive multiplexing and telecom compatibility, the platform shows promise for building scalable quantum networks. With the integration of Rydberg gates, the system can also enable entanglement purifications, deterministic Bell state measurements, and generation of 2D cluster states. Given most of the photonic chip is empty, it can also be used to host integrated circuits, allowing on-chip detection and frequency conversion capabilities. Similarly, alternative methods of coupling light to the nanophotonics, including grating couplers or tapered optical fibers via the chip surface, could be explored for possible applications where the ejected mode cannot overlap the free space array. The platform is also capable of combining different quantum simulation capabilities supported by 1D and 2D waveguides [150, 208, 323–327]. Overhanging nanobeams can be extended to loading tracks fabricated on the chip surface to provide atomic access to more complicated nanophotonic devices and circuits that cannot overhang the chip edge [328]. Waveguides for quantum simulation and cavities for atom-photon entanglement can be incorporated into the

same chip for distributed quantum simulation.

To fully utilize the potential of the photonic chip, the capability to actively stabilize multiple cavities in parallel has to be integrated with the system. Arrays of heating beams can be generated, similar to the tweezer array, to independently tune the cavities. With the combination of an array of detectors, each of the cavities can be independently locked to the atomic resonance. Another potential avenue to explore is the ability to deterministically park the devices on resonance. One way this can be achieved is by controlling the dispenser current to redshift all the devices and using LIAD on each of the cavities independently using focused lasers. A similar capability has been demonstrated in solid state systems using combined red shift using gas tuning and individual blue shift using heaters [329]. Developing similar capability using LIAD and the dispenser can significantly reduce the overhead of future experiments involving resonant atom cavity interactions.

One of the bigger challenges that has yet to be addressed in the system is the Rydberg integration. The presence of charges accumulated on the photonic devices can potentially contribute to fast variations on the Rydberg energy levels contributing to dephasing [168]. While the presence of a grounded substrate can potentially reduce the effect of these stray charges in our system, the conductivity of silicon nitride is low and can still contribute to charge noise. One potential way to overcome this is by moving further away from the chip for Rydberg gates. With a typical objective field of view of $\sim$400 μm, atoms can be taken to distances where Rydberg gates can be successfully integrated [168]. Even a modest speed of 0.2 μm/μs allows atoms to be moved 200 μm in a millisecond for Rydberg interactions. The addition of continuous reloading of atoms, and moving atoms away from the chip for Rydberg

gates, can potentially pave the way for a continuous (with a periodicity) yet deterministic multiplexed entangled photon source.

To conclude, this thesis introduces a novel hybrid platform merging the strengths of atom arrays with integrated photonics, including cavity arrays and waveguides. Some of the key functionalities are experimentally demonstrated, and a clear roadmap for subsequent advancements is outlined. This hybrid architecture presents compelling pathways toward scalable quantum computers and networks, while also enabling new paradigms in quantum simulation. While hurdles such as Rydberg integration require further work, several promising mitigation techniques have been identified. This research and the proposed future directions underscore the architecture's potential as a truly versatile quantum computing and networking engine, and I am excited by the prospect of its future development and translation into tangible technologies.

BIBLIOGRAPHY

1. DiVincenzo, D. P. The physical implementation of quantum computation. *Fortschritte der Physik: Progress of Physics* **48,** 771–783 (2000).

2. Nakamura, Y., Chen, C. D. & Tsai, J. S. Charge-Quantum Coherence Effects in Small Tunnel Junctions. *Phys. Rev. Lett.* **79,** 2328 (1997).

3. Nakamura, Y., Pashkin, Y. A., Yamamoto, T. & Tsai, J. S. Coherent Control of Macroscopic Quantum States in a Single-Cooper-Pair Box. *Phys. Rev. Lett.* **88,** 047901 (2002).

4. Vion, D. *et al.* Manipulating the Quantum State of an Electrical Circuit. *Science* **296,** 886 (2002).

5. Han, S., Yu, Y., Chu, X., Chu, S. & Wang, Z. Demonstration of Two-Bit Coherent Operation in a Josephson Charge Quantum Bit. *Science* **293,** 1457 (2001).

6. Yu, Y., Han, S., Chu, X., Chu, S. & Wang, Z. Coherent Temporal Oscillations of Macroscopic Quantum States in a Josephson Junction. *Science* **296,** 889 (2002).

7. Martinis, J. M., Nam, S., Aumentado, J. & Urbina, C. Rabi Oscillations in a Large Josephson-Junction Qubit. *Phys. Rev. Lett.* **89,** 117901 (2002).

8. Chiorescu, I., Nakamura, Y., Harmans, C. J. P. M. & Mooij, J. E. Coherent Quantum Dynamics of a Superconducting Flux Qubit. *Science* **299,** 1869 (2003).

9. Berkley, A. J. *et al.* Entangled Macroscopic Quantum States in Two Superconducting Qubits. *Science* **300,** 1548 (2003).

10. Pashkin, Y. A. *et al.* Quantum Coherent Oscillations in a Cooper-Pair Box. *Nature* **421,** 823 (2003).

11. Petta, J. R. *et al.* Coherent manipulation of coupled electron spins in semiconductor quantum dots. *Science* **309,** 2180–2184 (2005).

12. Charnock, F. T. & Kennedy, T. Combined optical and microwave approach for performing quantum spin operations on the nitrogen-vacancy center in diamond. *Physical Review B* **64,** 041201 (2001).

13. Jelezko, F., Gaebel, T, Popa, I, Gruber, A & Wrachtrup, J. Observation of coherent oscillations in a single electron spin. *Physical review letters* **92,** 076401 (2004).

14. Hanson, R, Gywat, O & Awschalom, D. Room-temperature manipulation and decoherence of a single spin in diamond. *Physical Review B—Condensed Matter and Materials Physics* **74,** 161203 (2006).

15. Cirac, J. I. & Zoller, P. Quantum computations with cold trapped ions. *Physical review letters* **74,** 4091 (1995).

16. Monroe, C., Meekhof, D. M., King, B. E., Itano, W. M. & Wineland, D. J. Demonstration of a Fundamental Quantum Logic Gate. *Phys. Rev. Lett.* **75,** 4714 (1995).

17. Turchette, Q. A. *et al.* Deterministic Entanglement of Two Trapped Ions. *Phys. Rev. Lett.* **81,** 3631 (1998).

18. Sackett, C. A. *et al.* Experimental Entanglement of Four Particles. *Nature* **404,** 256 (2000).

19. Brown, K. R. *et al.* Single-qubit-gate Error below 10^{-4} in a Trapped Ion. *Phys. Rev. A* **84,** 030303 (2011).

20. Benhelm, J., Kirchmair, G., Roos, C. F. & Blatt, R. Towards Fault-tolerant Quantum Computing with Trapped Ions. *Nature Physics* **4,** 463 (2008).

21. Myerson, A. H. *et al.* High-fidelity Readout of Trapped-ion Qubits. *Phys. Rev. Lett.* **100,** 200502 (2008).

22. Brennen, G. K., Caves, C. M., Jessen, P. S. & Deutsch, I. H. Quantum logic gates in optical lattices. *Physical Review Letters* **82,** 1060 (1999).

23. Briegel, H.-J., Calarco, T., Jaksch, D., Cirac, J. I. & Zoller, P. Quantum computing with neutral atoms. *Journal of modern optics* **47,** 415–451 (2000).

24. Jaksch, D. *et al.* Fast quantum gates for neutral atoms. *Physical Review Letters* **85,** 2208 (2000).

25. Isenhower, L *et al.* Demonstration of a neutral atom controlled-NOT quantum gate. *Physical review letters* **104,** 010503 (2010).

26. Zhang, X., Isenhower, L, Gill, A., Walker, T. & Saffman, M. Deterministic entanglement of two neutral atoms via Rydberg blockade. *Physical Review A—Atomic, Molecular, and Optical Physics* **82,** 030306 (2010).

27. Grimm, R., Weidemüller, M. & Ovchinnikov, Y. B. in *Advances in atomic, molecular, and optical physics* 95–170 (Elsevier, 2000).

28. Barredo, D., De Léséleuc, S., Lienhard, V., Lahaye, T. & Browaeys, A. An atom-by-atom assembler of defect-free arbitrary two-dimensional atomic arrays. *Science* **354,** 1021–1023 (2016).

29. Barredo, D., Lienhard, V., De Leseleuc, S., Lahaye, T. & Browaeys, A. Synthetic three-dimensional atomic structures assembled atom by atom. *Nature* **561,** 79–82 (2018).

30. Miroshnychenko, Y. *et al.* An atom-sorting machine. *Nature* **442,** 151–151 (2006).

31. Endres, M. *et al.* Atom-by-atom assembly of defect-free one-dimensional cold atom arrays. *Science* **354,** 1024–1027. https://www.science.org/doi/abs/10.1126/science.aah3752 (2016).

32. Bluvstein, D. *et al.* Logical quantum processor based on reconfigurable atom arrays. *Nature* **626,** 58–65 (2024).

33. Graham, T. M. *et al.* Multi-qubit entanglement and algorithms on a neutral-atom quantum computer. *Nature* **604,** 457–462. ISSN: 1476-4687. https://www.nature.com/articles/s41586-022-04603-6 (7906 Apr. 2022).

34. Semeghini, G. *et al.* Probing topological spin liquids on a programmable quantum simulator. *Science* **374,** 1242–1247 (2021).

35. Qiao, M. *et al.* Realization of a doped quantum antiferromagnet with dipolar tunnelings in a Rydberg tweezer array. *arXiv preprint arXiv:2501.08233* (2025).

36. Cao, A. *et al.* Multi-qubit gates and Schrödinger cat states in an optical clock. *Nature* **634,** 315–320 (2024).

37. Shaw, A. L. *et al.* Multi-ensemble metrology by programming local rotations with atom movements. *Nature Physics* **20,** 195–201 (2024).

38. Li, L. *et al.* Parallelized telecom quantum networking with a ytterbium-171 atom array. *arXiv preprint arXiv:2502.17406* (2025).

39. Hartung, L., Seubert, M., Welte, S., Distante, E. & Rempe, G. A quantum-network register assembled with optical tweezers in an optical cavity. *Science* **385,** 179–183 (2024).

40. Manetsch, H. J. *et al.* A tweezer array with 6100 highly coherent atomic qubits. *arXiv preprint arXiv:2403.12021* (2024).

41. Bluvstein, D. *et al.* A quantum processor based on coherent transport of entangled atom arrays. *Nature* **604,** 451–456 (2022).

42. Jenkins, A., Lis, J. W., Senoo, A., McGrew, W. F. & Kaufman, A. M. Ytterbium nuclear-spin qubits in an optical tweezer array. *Physical Review X* **12,** 021027 (2022).

43. Ma, S. *et al.* Universal gate operations on nuclear spin qubits in an optical tweezer array of Yb 171 atoms. *Physical Review X* **12,** 021028 (2022).

44. Jenkins, A., Lis, J. W., Senoo, A., McGrew, W. F. & Kaufman, A. M. Ytterbium Nuclear-Spin Qubits in an Optical Tweezer Array (vol 12, 021027, 2022). *PHYSICAL REVIEW X* **13** (2023).

45. Huie, W. *et al.* Repetitive readout and real-time control of nuclear spin qubits in 171 Yb atoms. *PRX Quantum* **4,** 030337 (2023).

46. Finkelstein, R. *et al.* Universal quantum operations and ancilla-based read-out for tweezer clocks. *Nature* **634,** 321–327 (2024).

47. Levine, H. *et al.* Dispersive optical systems for scalable Raman driving of hyperfine qubits. *Physical Review A* **105,** 032618 (2022).

48. Saffman, M. Quantum computing with atomic qubits and Rydberg interactions: progress and challenges. *Journal of Physics B: Atomic, Molecular and Optical Physics* **49,** 202001 (2016).

49. Levine, H. *et al.* Parallel Implementation of High-Fidelity Multiqubit Gates with Neutral Atoms. *Phys. Rev. Lett.* **123,** 170503. `https://link.aps.org/doi/10.1103/PhysRevLett.123.170503` (17 2019).

50. Evered, S. J. *et al.* High-fidelity parallel entangling gates on a neutral-atom quantum computer. *Nature* **622,** 268–272. ISSN: 1476-4687. `https://doi.org/10.1038/s41586-023-06481-y` (7982 Oct. 2023).

51. Tsai, R. B.-S., Sun, X., Shaw, A. L., Finkelstein, R. & Endres, M. Benchmarking and fidelity response theory of high-fidelity rydberg entangling gates. *PRX Quantum* **6,** 010331 (2025).

52. Chew, Y. *et al.* Ultrafast energy exchange between two single Rydberg atoms on a nanosecond timescale. *Nature Photonics* **16,** 724–729 (2022).

53. Anand, S. *et al.* A dual-species Rydberg array. *Nature Physics* **20,** 1744–1750 (2024).

54. Radnaev, A. *et al.* A universal neutral-atom quantum computer with individual optical addressing and non-destructive readout. *arXiv preprint arXiv:2408.08288* (2024).

55. Singh, K. *et al.* Mid-circuit correction of correlated phase errors using an array of spectator qubits. *Science* **380,** 1265–1269. ISSN: 10959203. https://www.science.org/doi/10.1126/science.ade5337 (6651 June 2023).

56. Lis, J. W. *et al.* Mid-circuit operations using the omg-architecture in neutral atom arrays. *arXiv:2305.19266v2.* http://arxiv.org/abs/2305.19266 (May 2023).

57. Graham, T. M. *et al.* Mid-circuit measurements on a neutral atom quantum processor. *arXiv:2303.10051v3.* http://arxiv.org/abs/2303.10051 (Mar. 2023).

58. Deist, E. *et al.* Mid-Circuit Cavity Measurement in a Neutral Atom Array. *Physical Review Letters* **129,** 203602. ISSN: 10797114. https://journals.aps.org/prl/abstract/10.1103/PhysRevLett.129.203602 (20 Nov. 2022).

59. Fowler, A. G., Mariantoni, M., Martinis, J. M. & Cleland, A. N. Surface codes: Towards practical large-scale quantum computation. *Physical Review A—Atomic, Molecular, and Optical Physics* **86,** 032324 (2012).

60. Xu, Q. *et al.* Constant-overhead fault-tolerant quantum computation with reconfigurable atom arrays. *Nature Physics* **20,** 1084–1090 (2024).

61. Cirac, J. I., Ekert, A., Huelga, S. F. & Macchiavello, C. Distributed quantum computation over noisy channels. *Physical Review A* **59,** 4249 (1999).

62. Jiang, L., Taylor, J. M., Sørensen, A. S. & Lukin, M. D. Distributed quantum computation based on small quantum registers. *Physical Review A—Atomic, Molecular, and Optical Physics* **76,** 062323 (2007).

63. Helmer, F. *et al.* Cavity grid for scalable quantum computation with superconducting circuits. *Europhysics Letters* **85,** 50007 (2009).

64. Monroe, C. *et al.* Large-scale modular quantum-computer architecture with atomic memory and photonic interconnects. *Physical Review A* **89,** 022317. ISSN: 10502947. https://journals.aps.org/pra/abstract/10.1103/PhysRevA.89.022317 (2 Feb. 2014).

65. Clementi, M. *et al.* Classical multiparty computation using quantum resources. *Physical Review A* **96,** 062317 (2017).

66. Childs, A. M. Secure assisted quantum computation. *arXiv preprint quant-ph/0111046* (2001).

67. Crépeau, C., Gottesman, D. & Smith, A. *Secure multi-party quantum computation* in *Proceedings of the thiry-fourth annual ACM symposium on Theory of computing* (2002), 643–652.

68. Arrighi, P. & Salvail, L. BLIND QUANTUM COMPUTATION. *International Journal of Quantum Information* **4,** 883–898. ISSN: 02197499 (5 Nov. 2006).

69. Broadbent, A., Fitzsimons, J. & Kashefi, E. Universal blind quantum computation. *50th annual IEEE symposium on foundations of computer science.* http://arxiv.org/abs/0807.4154http://dx.doi.org/10.1109/FOCS.2009.36 (July 2008).

70. Buhrman, H., Cleve, R., Watrous, J. & De Wolf, R. Quantum fingerprinting. *Physical review letters* **87,** 167902 (2001).

71. Bennett, C. H. & Brassard, G. Quantum cryptography: Public key distribution and coin tossing. *Theoretical computer science* **560,** 7–11 (2014).

72. Ekert, A. K. Quantum cryptography based on Bell's theorem. *Physical review letters* **67,** 661 (1991).

73. Bennett, C. H., Brassard, G. & Mermin, N. D. Quantum cryptography without Bell's theorem. *Physical review letters* **68,** 557 (1992).

74. Shor, P. W. & Preskill, J. Simple proof of security of the BB84 quantum key distribution protocol. *Physical review letters* **85,** 441 (2000).

75. Gottesman, D. Uncloneable encryption. *arXiv preprint quant-ph/0210062* (2002).

76. Hahn, F. *et al.* Anonymous conference key agreement in quantum networks. *arXiv preprint arXiv:2007.07995* (2020).

77. Fitzi, M., Gisin, N. & Maurer, U. Quantum solution to the Byzantine agreement problem. *Physical Review Letters* **87,** 217901 (2001).

78. Ben-Or, M. & Hassidim, A. *Fast quantum byzantine agreement* in *Proceedings of the thirty-seventh annual ACM symposium on Theory of computing* (2005), 481–485.

79. Taherkhani, M. A., Navi, K. & Van Meter, R. Resource-aware system architecture model for implementation of quantum aided Byzantine agreement on quantum repeater networks. *Quantum science and technology* **3,** 014011 (2017).

80. Pappa, A., Chailloux, A., Wehner, S., Diamanti, E. & Kerenidis, I. Multipartite entanglement verification resistant against dishonest parties. *Physical review letters* **108,** 260502 (2012).

81. Centrone, F., Diamanti, E. & Kerenidis, I. Quantum protocol for electronic voting without election authorities. *Physical Review Applied* **18,** 014005 (2022).

82. Gottesman, D., Jennewein, T. & Croke, S. Longer-baseline telescopes using quantum repeaters. *Physical Review Letters* **109,** 070503. ISSN: 00319007. https://journals.aps.org/prl/abstract/10.1103/PhysRevLett.109.070503 (7 Aug. 2012).

83. Kómár, P. *et al.* A quantum network of clocks. *Nature Physics* **10,** 582–587. ISSN: 1745-2481. https://www.nature.com/articles/nphys3000 (8 June 2014).

84. Borregaard, J. & Pikovski, I. Testing quantum theory on curved space-time with quantum networks. *arXiv preprint arXiv:2406.19533* (2024).

85. Covey, J. P., Pikovski, I. & Borregaard, J. Probing curved spacetime with a distributed atomic processor clock. *arXiv preprint arXiv:2502.12954* (2025).

86. Eisert, J., Wilkens, M. & Lewenstein, M. Quantum games and quantum strategies. *Physical Review Letters* **83,** 3077 (1999).

87. Brassard, G., Broadbent, A. & Tapp, A. Quantum pseudo-telepathy. *Foundations of Physics* **35,** 1877–1907 (2005).

88. Gavinsky, D., Kempe, J. & de Wolf, R. Exponential separation of quantum and classical one-way communication complexity for a boolean function. *arXiv preprint quant-ph/0607174* (2006).

89. Ding, D. & Jiang, L. Coordinating Decisions via Quantum Telepathy. *arXiv preprint arXiv:2407.21723* (2024).

90. Liao, S.-K. *et al.* Satellite-to-ground quantum key distribution. *Nature* **549,** 43–47 (2017).

91. Li, Y. *et al.* Space–ground QKD network based on a compact payload and medium-inclination orbit. *Optica* **9,** 933–938 (2022).

92. Briegel, H.-J., Dür, W., Cirac, J. I. & Zoller, P. Quantum Repeaters: The Role of Imperfect Local Operations in Quantum Communication. *Physical Review Letters* **81,** 5932–5935 (26 1998).

93. Muralidharan, S. *et al.* Optimal architectures for long distance quantum communication. *Scientific reports* **6,** 20463 (2016).

94. Pompili, M. *et al.* Realization of a multinode quantum network of remote solid-state qubits. *Science* **372,** 259–264 (2021).

95. Hermans, S. *et al.* Qubit teleportation between non-neighbouring nodes in a quantum network. *Nature* **605,** 663–668 (2022).

96. Yu, Y. *et al.* Entanglement of two quantum memories via fibres over dozens of kilometres. *Nature* **578,** 240–245 (2020).

97. Knaut, C. M. *et al.* Entanglement of nanophotonic quantum memory nodes in a telecom network. *Nature* **629,** 573–578 (2024).

98. Stolk, A. J. *et al.* Metropolitan-scale heralded entanglement of solid-state qubits. *Science advances* **10,** eadp6442 (2024).

99. Rakonjac, J. V. *et al.* Entanglement between a telecom photon and an on-demand multimode solid-state quantum memory. *Physical review letters* **127,** 210502 (2021).

100. Stas, P.-J. *et al.* Robust multi-qubit quantum network node with integrated error detection. *Science* **378,** 557–560 (2022).

101. Zhang, S. *et al.* Fast delivery of heralded atom-photon quantum correlation over 12 km fiber through multiplexing enhancement. *Nature Communications* **15,** 10306 (2024).

102. Ruskuc, A *et al.* Multiplexed entanglement of multi-emitter quantum network nodes. *Nature,* 1–6 (2025).

103. Chang, X.-Y. *et al.* Hybrid entanglement and error correction in a scalable quantum network node. *arXiv preprint arXiv:2408.07752* (2024).

104. Gu, F. *et al.* Hybrid Quantum Repeaters with Ensemble-based Quantum Memories and Single-spin Photon Transducers. *arXiv:2401.12395* (2024).

105. Maring, N. *et al.* Photonic quantum state transfer between a cold atomic gas and a crystal. *Nature* **551,** 485–488 (2017).

106. Craddock, A. *et al.* Quantum interference between photons from an atomic ensemble and a remote atomic ion. *Physical review letters* **123,** 213601 (2019).

107. Lin, Y., Leibrandt, D. R., Leibfried, D. & Chou, C.-w. Quantum entanglement between an atom and a molecule. *Nature* **581,** 273–277 (2020).

108. Meyer, H. *et al.* Direct photonic coupling of a semiconductor quantum dot and a trapped ion. *Physical review letters* **114,** 123001 (2015).

109. Cussenot, P *et al.* Uniting Quantum Processing Nodes of Cavity-coupled Ions with Rare-earth Quantum Repeaters Using Single-photon Pulse Shaping Based on Atomic Frequency Comb. *arXiv preprint arXiv:2501.18704* (2025).

110. Chai, Y. *et al. Hybrid atom'rare-earth ion quantum interfaces and network nodes* in *APS March Meeting Abstracts* **2023** (2023), D67–001.

111. Kumar, A. *et al.* Quantum-enabled millimetre wave to optical transduction using neutral atoms. *Nature* **615,** 614–619 (2023).

112. Main, D *et al.* Distributed quantum computing across an optical network link. *Nature,* 1–6 (2025).

113. Drmota, P. *et al.* Verifiable blind quantum computing with trapped ions and single photons. *Physical Review Letters* **132,** 150604 (2024).

114. Wei, Y.-C. *et al.* Universal distributed blind quantum computing with solid-state qubits. *arXiv preprint arXiv:2412.03020* (2024).

115. Drmota, P *et al.* Experimental Quantum Advantage in the Odd-Cycle Game. *arXiv preprint arXiv:2406.08412* (2024).

116. Malia, B. K., Wu, Y., Martínez-Rincón, J. & Kasevich, M. A. Distributed quantum sensing with mode-entangled spin-squeezed atomic states. *Nature* **612,** 661–665 (2022).

117. Nichol, B. C. *et al.* An elementary quantum network of entangled optical atomic clocks. *Nature* **609,** 689–694 (2022).

118. Sinclair, N. *et al.* Spectral multiplexing for scalable quantum photonics using an atomic frequency comb quantum memory and feed-forward control. *Physical review letters* **113,** 053603 (2014).

119. Ulanowski, A., Merkel, B. & Reiserer, A. Spectral multiplexing of telecom emitters with stable transition frequency. *Science advances* **8,** eabo4538 (2022).

120. Pu, Y. *et al.* Experimental realization of a multiplexed quantum memory with 225 individually accessible memory cells. *Nature communications* **8,** 15359 (2017).

121. Kalb, N. *et al.* Entanglement distillation between solid-state quantum network nodes. *Science* **356,** 928 (2017).

122. Canteri, M *et al.* A photon-interfaced ten qubit quantum network node. *arXiv preprint arXiv:2406.09480* (2024).

123. Dréau, A., Tchebotareva, A., Mahdaoui, A. E., Bonato, C. & Hanson, R. Quantum frequency conversion of single photons from a nitrogen-vacancy center in diamond to telecommunication wavelengths. *Physical review applied* **9,** 064031 (2018).

124. Maring, N., Lago-Rivera, D., Lenhard, A., Heinze, G. & de Riedmatten, H. Quantum frequency conversion of memory-compatible single photons from 606 nm to the telecom C-band. *Optica* **5,** 507–513 (2018).

125. Van Leent, T. *et al.* Long-distance distribution of atom-photon entanglement at telecom wavelength. *Physical review letters* **124,** 010510 (2020).

126. Dusanowski, Ł. *et al.* Optical charge injection and coherent control of a quantum-dot spin-qubit emitting at telecom wavelengths. *Nature communications* **13,** 748 (2022).

127. Laccotripes, P *et al.* Spin-photon entanglement with direct photon emission in the telecom C-band. *Nature Communications* **15,** 9740 (2024).

128. Uysal, M. T. *et al.* Spin-photon entanglement of a single Er{3+} ion in the telecom band. *arXiv preprint arXiv:2406.06515* (2024).

129. Huang, Y., Salces-Carcoba, F., Adhikari, R. X., Safavi-Naeini, A. H. & Jiang, L. Vacuum beam guide for large scale quantum networks. *Physical Review Letters* **133,** 020801 (2024).

130. Kimble, H. J. Strong interactions of single atoms and photons in cavity QED. *Physica Scripta* **1998,** 127 (1998).

131. Moehring, D. L. *et al.* Entanglement of single-atom quantum bits at a distance. *Nature* **449,** 68–71 (2007).

132. Ritter, S. *et al.* An elementary quantum network of single atoms in optical cavities. *Nature* **484,** 195–200 (2012).

133. Bernien, H. *et al.* Heralded entanglement between solid-state qubits separated by three metres. *Nature* **497,** 86–90 (2013).

134. Lynn, T. W. *Measurement and control of individual quanta in cavity QED* (California Institute of Technology, 2003).

135. Dordevic, T. *A nanophotonic quantum interface for atoms in optical tweezers* PhD thesis (Harvard University, 2022).

136. Haroche, S. & Raimond, J.-M. *Exploring the quantum: atoms, cavities, and photons* (Oxford university press, 2006).

137. Rempe, G. One atom in an optical cavity: Spatial resolution beyond the standard diffraction limit. *Applied Physics B* **60,** 233–237 (1995).

138. Chiarella, G., Frank, T., Farrera, P. & Rempe, G. Two-cavity-mediated photon-pair emission<? pag\break?> by one atom. *Optica Quantum* **2,** 346–350 (2024).

139. Grinkemeyer, B. *et al.* Error-detected quantum operations with neutral atoms mediated by an optical cavity. *Science* **387,** 1301–1305 (2025).

140. Scully, M. O. & Zubairy, M. S. *Quantum optics* (Cambridge university press, 1997).

141. Spillane, S., Kippenberg, T. & Vahala, K. Ultralow-threshold Raman laser using a spherical dielectric microcavity. *Nature* **415,** 621–623 (2002).

142. Zhong, T. *et al.* Nanophotonic rare-earth quantum memory with optically controlled retrieval. *Science* **357,** 1392–1395 (2017).

143. Thompson, R., Rempe, G. & Kimble, H. Observation of normal-mode splitting for an atom in an optical cavity. *Physical review letters* **68,** 1132 (1992).

144. Walls, D. & Milburn, G. J. in *Quantum optics* (Springer, 2008).

145. Hu, C., Young, A, O'brien, J., Munro, W. & Rarity, J. Giant optical Faraday rotation induced by a single-electron spin in a quantum dot: applications to entangling remote spins via a single photon. *Physical Review B—Condensed Matter and Materials Physics* **78,** 085307 (2008).

146. Tiecke, T. *et al.* Nanophotonic quantum phase switch with a single atom. *Nature* **508,** 241–244 (2014).

147. Welte, S., Hacker, B., Daiss, S., Ritter, S. & Rempe, G. Cavity carving of atomic bell states. *Physical review letters* **118,** 210503 (2017).

148. Reiserer, A., Kalb, N., Rempe, G. & Ritter, S. A quantum gate between a flying optical photon and a single trapped atom. *Nature* **508,** 237–240 (2014).

149. Kim, J., Yang, D., Oh, S.-h. & An, K. Coherent single-atom superradiance. *Science* **359,** 662–666 (2018).

150. Yan, Z. *et al.* Super-radiant and Sub-radiant Cavity Scattering by Atom Arrays. *arXiv:2307.13321v1.* `http://arxiv.org/abs/2307.13321` (July 2023).

151. Wang, Z. *et al.* A cavity QED system with defect-free single-atom array strongly coupled to an optical cavity. *arXiv preprint arXiv:2502.19833* (2025).

152. Hu, B. *et al.* Site-selective cavity readout and classical error correction of a 5-bit atomic register. *Physical Review Letters* **134,** 120801 (2025).

153. Hunger, D. *et al.* A fiber Fabry–Perot cavity with high finesse. *New Journal of Physics* **12,** 065038 (2010).

154. Niemietz, D. *Nondestructive detection of photonic qubits with single atoms in crossed fiber cavities* PhD thesis (Technische Universität München, 2021).

155. Brekenfeld, M., Niemietz, D., Christesen, J. D. & Rempe, G. A quantum network node with crossed optical fibre cavities. *Nature Physics* **16,** 647–651. ISSN: 1745-2481. `https://www.nature.com/articles/s41567-020-0855-3` (6 Apr. 2020).

156. Gallego, J. *et al.* Strong Purcell effect on a neutral atom trapped in an open fiber cavity. *Physical review letters* **121,** 173603 (2018).

157. Wang, J. *et al.* Ultrafast high-fidelity state readout of single neutral atom. *arXiv preprint arXiv:2412.12584* (2024).

158. Wang, J. *et al.* Purcell-Enhanced Generation of Photonic Bell States via the Inelastic Scattering off Single Atoms. *Physical Review Letters* **134,** 053401 (2025).

159. Vahala, K. J. Optical microcavities. *Nature* **424,** 839–846 (2003).

160. Aoki, T. *et al.* Observation of strong coupling between one atom and a monolithic microresonator. *Nature* **443,** 671–674 (2006).

161. Stern, N. P., Alton, D. J. & Kimble, H. J. Simulations of atomic trajectories near a dielectric surface. *New Journal of Physics* **13,** 085004 (2011).

162. Thompson, J. D. *et al.* Coupling a Single Trapped Atom to a Nanoscale Optical Cavity. *Science* **340,** 1202–1205 (6137 June 2013).

163. Goban, A. *et al.* Atom–light interactions in photonic crystals. *Nature Communications* **5,** 1–9. ISSN: 2041-1723. `https://www.nature.com/articles/ncomms4808` (1 May 2014).

164. Goban, A *et al.* Demonstration of a state-insensitive, compensated nanofiber trap. *Physical review letters* **109,** 033603 (2012).

165. Hood, J. D. *et al.* Atom–atom interactions around the band edge of a photonic crystal waveguide. *Proceedings of the National Academy of Sciences* **113,** 10507–10512 (2016).

166. Dareau, A., Meng, Y, Schneeweiss, P & Rauschenbeutel, A. Observation of ultrastrong spin-motion coupling for cold atoms in optical microtraps. *Physical Review Letters* **121,** 253603 (2018).

167. Samutpraphoot, P. *et al.* Strong Coupling of Two Individually Controlled Atoms via a Nanophotonic Cavity. *Physical Review Letters* **124,** 063602. ISSN: 10797114 (6 Feb. 2020).

168. . Entanglement transport and a nanophotonic interface for atoms in optical tweezers. *Science* **373,** 1511–1514. ISSN: 10959203 (6562 Sept. 2021).

169. Solano, P., Barberis-Blostein, P., Fatemi, F. K., Orozco, L. A. & Rolston, S. L. Superradiance reveals infinite-range dipole interactions through a nanofiber. *Nature communications* **8,** 1857. ISSN: 10959203 (6562 Sept. 2017).

170. Liedl, C. *et al.* Observation of superradiant bursts in a cascaded quantum system. *Physical Review X* **14,** 011020. ISSN: 10959203 (6562 Sept. 2024).

171. Suresh, D. A., Zhou, X., Hung, C.-L. & Robicheaux, F. Collective emission and selective-radiance in atomic clouds and arrays coupled to a microring resonator. *arXiv preprint arXiv:2503.21121* **373,** 1511–1514. ISSN: 10959203 (6562 Sept. 2025).

172. Chang, D. E., Cirac, J. I. & Kimble, H. J. Self-organization of atoms along a nanophotonic waveguide. *Physical review letters* **110,** 113606. ISSN: 10959203 (6562 Sept. 2013).

173. Eldredge, Z., Solano, P., Chang, D. & Gorshkov, A. V. Self-organization of atoms coupled to a chiral reservoir. *Physical Review A* **94,** 053855. ISSN: 10959203 (6562 Sept. 2016).

174. Manzoni, M. T., Mathey, L. & Chang, D. E. Designing exotic many-body states of atomic spin and motion in photonic crystals. *Nature communications* **8,** 14696. ISSN: 10959203 (6562 Sept. 2017).

175. Paulisch, V., Kimble, H., Cirac, J. I. & González-Tudela, A. Generation of single-and two-mode multiphoton states in waveguide QED. *Physical Review A* **97,** 053831. ISSN: 10959203 (6562 Sept. 2018).

176. Jones, R., Buonaiuto, G., Lang, B., Lesanovsky, I. & Olmos, B. Collectively enhanced chiral photon emission from an atomic array near a nanofiber. *Physical review letters* **124,** 093601. ISSN: 10959203 (6562 Sept. 2020).

177. Perczel, J., Borregaard, J., Chang, D. E., Yelin, S. F. & Lukin, M. D. Topological quantum optics using atomlike emitter arrays coupled to photonic crystals. *Physical Review Letters* **124,** 083603. ISSN: 10959203 (6562 Sept. 2020).

178. Navarro-Barón, E. P., Vinck-Posada, H. & González-Tudela, A. Photon-mediated interactions near a Dirac photonic crystal slab. *ACS Photonics* **8,** 3209–3217. ISSN: 10959203 (6562 Sept. 2021).

179. Holzinger, R. *et al.* Control of localized single-and many-body dark states in waveguide QED. *Physical Review Letters* **129,** 253601. ISSN: 10959203 (6562 Sept. 2022).

180. Cardenas-Lopez, S., Masson, S. J., Zager, Z. & Asenjo-Garcia, A. Many-body superradiance and dynamical mirror symmetry breaking in waveguide QED. *Physical Review Letters* **131,** 033605. ISSN: 10959203 (6562 Sept. 2023).

181. Tabares, C., Muñoz de Las Heras, A., Tagliacozzo, L., Porras, D. & González-Tudela, A. Variational quantum simulators based on waveguide QED. *Physical review letters* **131,** 073602. ISSN: 10959203 (6562 Sept. 2023).

182. González-Tudela, A., Reiserer, A., García-Ripoll, J. J. & García-Vidal, F. J. Light–matter interactions in quantum nanophotonic devices. *Nature Reviews Physics* **6,** 166–179. ISSN: 10959203 (6562 Sept. 2024).

183. Di Benedetto, E., Gonzalez-Tudela, A. & Ciccarello, F. Dipole-dipole interactions mediated by a photonic flat band. *Quantum* **9,** 1671. ISSN: 10959203 (6562 Sept. 2025).

184. Hinney, J. *et al.* Unraveling two-photon entanglement via the squeezing spectrum of light traveling through nanofiber-coupled atoms. *Physical Review Letters* **127,** 123602. ISSN: 10959203 (6562 Sept. 2021).

185. González-Tudela, A., Paulisch, V., Chang, D., Kimble, H. & Cirac, J. I. Deterministic generation of arbitrary photonic states assisted by dissipation. *Physical review letters* **115,** 163603. ISSN: 10959203 (6562 Sept. 2015).

186. Rubies-Bigorda, O., Masson, S. J., Yelin, S. F. & Asenjo-Garcia, A. Deterministic generation of photonic entangled states using decoherence-free subspaces. *arXiv preprint arXiv:2410.03325* **373,** 1511–1514. ISSN: 10959203 (6562 Sept. 2024).

187. Vetsch, E. *et al.* Optical interface created by laser-cooled atoms trapped in the evanescent field surrounding an optical nanofiber. *Physical Review Letters* **104,** 203603. ISSN: 00319007. `https://journals.aps.org/prl/abstract/10.1103/PhysRevLett.104.203603` (20 May 2010).

188. Sørensen, H. *et al.* Coherent backscattering of light off one-dimensional atomic strings. *Physical review letters* **117,** 133604. ISSN: 10959203 (6562 Sept. 2016).

189. Corzo, N. V. *et al.* Waveguide-coupled single collective excitation of atomic arrays. *Nature* **566,** 359–362. ISSN: 10959203 (6562 Sept. 2019).

190. Nayak, K. P., Wang, J. & Keloth, J. Real-time observation of single atoms trapped and interfaced to a nanofiber cavity. *Physical Review Letters* **123,** 213602. ISSN: 10959203 (6562 Sept. 2019).

191. Junge, C., O'shea, D., Volz, J. & Rauschenbeutel, A. Strong coupling between single atoms and nontransversal photons. *Physical review letters* **110,** 213604. ISSN: 10959203 (6562 Sept. 2013).

192. Will, E., Masters, L., Rauschenbeutel, A., Scheucher, M. & Volz, J. Coupling a single trapped atom to a whispering-gallery-mode microresonator. *Physical Review Letters* **126,** 233602. ISSN: 10959203 (6562 Sept. 2021).

193. Luan, X. *et al.* The Integration of Photonic Crystal Waveguides with Atom Arrays in Optical Tweezers. *Advanced Quantum Technologies* **3,** 2000008. ISSN: 10959203 (6562 Sept. 2020).

194. Burgers, A. P. *et al.* Clocked atom delivery to a photonic crystal waveguide. *Proceedings of the National Academy of Sciences* **116,** 456–465. ISSN: 10959203 (6562 Sept. 2019).

195. Xu, L. *et al.* Transporting cold atoms towards a GaN-on-sapphire chip via an optical conveyor belt. *arXiv preprint arXiv:2305.07900* **373,** 1511–1514. ISSN: 10959203 (6562 Sept. 2023).

196. Kim, M. E., Chang, T.-H., Fields, B. M., Chen, C.-A. & Hung, C.-L. Trapping single atoms on a nanophotonic circuit with configurable tweezer lattices. *Nature Communications* **10,** 1–8. ISSN: 2041-1723. https://www.nature.com/articles/s41467-019-09635-7 (1 Apr. 2019).

197. Zhou, X., Tamura, H., Chang, T.-H. & Hung, C.-L. Coupling single atoms to a nanophotonic whispering-gallery-mode resonator via optical guiding. *Physical Review Letters* **130,** 103601. ISSN: 10959203 (6562 Sept. 2023).

198. Meng, Y., Liedl, C., Pucher, S., Rauschenbeutel, A. & Schneeweiss, P. Imaging and Localizing Individual Atoms Interfaced with a Nanophotonic Waveguide. *Physical Review Letters* **125,** 053603. ISSN: 10797114 (5 July 2020).

199. Béguin, J.-B. *et al.* Advanced apparatus for the integration of nanophotonics and cold atoms. *Optica* **7,** 1–2. ISSN: 10959203 (6562 Sept. 2020).

200. Linke, N. M. *et al.* Background-free detection of trapped ions. *Applied Physics B* **107,** 1175–1180. ISSN: 1432-0649. https://doi.org/10.1007/s00340-011-4870-z (2021) (6562 June 2012).

201. McGilligan, J. P. *et al.* Laser cooling in a chip-scale platform. *Applied Physics Letters* **117,** 054001. ISSN: 0003-6951. https://doi.org/10.1063/5.0014658 (2023) (6562 Aug. 2020).

202. Ohadi, H., Himsworth, M., Xuereb, A. & Freegarde, T. Magneto-optical trapping and background-free imaging for atoms near nanostructured surfaces. *Optics Express* **17,**

23003–23009. ISSN: 1094-4087. https://www.osapublishing.org/oe/abstract.cfm?uri=oe-17-25-23003 (2021) (6562 Dec. 2009).

203. Yang, B., Liang, Q., He, J. & Wang, J. Background-free fluorescence detection of cold atoms in a two-color magneto-optical trap. *Optics Express* **20,** 11944–11952. ISSN: 1094-4087. https://www.osapublishing.org/oe/abstract.cfm?uri=oe-20-11-11944 (2021) (6562 May 2012).

204. Covey, J. P. *et al.* Telecom-band quantum optics with ytterbium atoms and silicon nanophotonics. *Physical Review Applied* **11,** 034044. ISSN: 10959203 (6562 Sept. 2019).

205. Menon, S. G., Singh, K., Borregaard, J. & Bernien, H. Nanophotonic quantum network node with neutral atoms and an integrated telecom interface. *New Journal of Physics* **22,** 73033. ISSN: 13672630 (7 July 2020).

206. Huie, W., Menon, S. G., Bernien, H. & Covey, J. P. Multiplexed telecommunication-band quantum networking with atom arrays in optical cavities. *Physical Review Research* **3,** 043154. ISSN: 26431564. https://journals.aps.org/prresearch/abstract/10.1103/PhysRevResearch.3.043154 (4 Dec. 2021).

207. Ramette, J., Sinclair, J., Breuckmann, N. P. & Vuletić, V. Fault-Tolerant Connection of Error-Corrected Qubits with Noisy Links. *arXiv:2302.01296v1* **373,** 1511–1514. ISSN: 10959203. http://arxiv.org/abs/2302.01296 (6562 Feb. 2023).

208. González-Tudela, A., Paulisch, V., Chang, D. E., Kimble, H. J. & Cirac, J. I. Deterministic Generation of Arbitrary Photonic States Assisted by Dissipation. *Physical*

Review Letters **115,** 163603. ISSN: 10797114. https://journals.aps.org/prl/abstract/10.1103/PhysRevLett.115.163603 (16 Oct. 2015).

209. Sørensen, A. & Mølmer, K. Quantum computation with ions in thermal motion. *Physical review letters* **82,** 1971. ISSN: 10959203 (6562 Sept. 1999).

210. Mølmer, K. & Sørensen, A. Multiparticle entanglement of hot trapped ions. *Physical Review Letters* **82,** 1835. ISSN: 10959203 (6562 Sept. 1999).

211. Sørensen, A. & Mølmer, K. Entanglement and quantum computation with ions in thermal motion. *Physical Review A* **62,** 022311. ISSN: 10959203 (6562 Sept. 2000).

212. Lukin, M. D. *et al.* Dipole blockade and quantum information processing in mesoscopic atomic ensembles. *Physical review letters* **87,** 037901. ISSN: 10959203 (6562 Sept. 2001).

213. Protsenko, I. E., Reymond, G., Schlosser, N. & Grangier, P. Operation of a quantum phase gate using neutral atoms in microscopic dipole traps. *Physical Review A* **65,** 052301. ISSN: 10959203 (6562 Sept. 2002).

214. Saffman, M & Walker, T. Analysis of a quantum logic device based on dipole-dipole interactions of optically trapped Rydberg atoms. *Physical Review A—Atomic, Molecular, and Optical Physics* **72,** 022347. ISSN: 10959203 (6562 Sept. 2005).

215. Urban, E *et al.* Observation of Rydberg blockade between two atoms. *Nature Physics* **5,** 110–114. ISSN: 10959203 (6562 Sept. 2009).

216. Müller, M., Liang, L., Lesanovsky, I. & Zoller, P. Trapped Rydberg ions: from spin chains to fast quantum gates. *New Journal of Physics* **10,** 093009. ISSN: 10959203 (6562 Sept. 2008).

217. Samutpraphoot, P. *A quantum network node based on a nanophotonic interface for atoms in optical tweezers* PhD thesis (Harvard University, Sept. 2021), 1511–1514.

218. Luan, X. *et al.* The Integration of Photonic Crystal Waveguides with Atom Arrays in Optical Tweezers. *Advanced Quantum Technologies* **3,** 2000008. ISSN: 10959203 (6562 Sept. 2020).

219. Singh, K., Anand, S., Pocklington, A., Kemp, J. T. & Bernien, H. Dual-element, two-dimensional atom array with continuous-mode operation. *Physical Review X* **12,** 011040. ISSN: 10959203 (6562 Sept. 2022).

220. Scholl, P. *et al.* Quantum simulation of 2D antiferromagnets with hundreds of Rydberg atoms. *Nature* **595,** 233–238. ISSN: 1476-4687. `https://www.nature.com/articles/s41586-021-03585-1` (7866 July 2021).

221. Joannopoulos, J. D., Johnson, S. G., Winn, J. N. & Meade, R. D. *Photonic Crystals: Molding the Flow of Light - Second Edition* 1511–1514. ISBN: 978-0691124568 (Princeton University Press, Princeton, NJ, Sept. 2008).

222. Chan, J. *Laser cooling of an optomechanical crystal resonator to its quantum ground state of motion* 1511–1514 (California Institute of Technology, Sept. 2012).

223. Quan, Q. & Loncar, M. Deterministic design of wavelength scale, ultra-high Q photonic crystal nanobeam cavities. *Optics express* **19,** 18529–18542. ISSN: 10959203 (6562 Sept. 2011).

224. Norte, R. A. *Nanofabrication for on-chip optical levitation, atom-trapping, and superconducting quantum circuits* 1511–1514 (California Institute of Technology, Sept. 2015).

225. Gröblacher, S., Hill, J. T., Safavi-Naeini, A. H., Chan, J. & Painter, O. Highly efficient coupling from an optical fiber to a nanoscale silicon optomechanical cavity. *Applied Physics Letters* **103,** 1511–1514. ISSN: 10959203 (6562 Sept. 2013).

226. Tiecke, T. *et al.* Efficient fiber-optical interface for nanophotonic devices. *Optica* **2,** 70–75. ISSN: 10959203 (6562 Sept. 2015).

227. Zeng, B. *et al.* Cryogenic packaging of nanophotonic devices with a low coupling loss< 1 dB. *Applied physics letters* **123,** 1511–1514. ISSN: 10959203 (6562 Sept. 2023).

228. Chang, T.-H., Zhou, X., Tamura, H. & Hung, C.-L. Realization of efficient 3D tapered waveguide-to-fiber couplers on a nanophotonic circuit. *Optics Express* **30,** 31643–31652. ISSN: 10959203 (6562 Sept. 2022).

229. Schiappelli, F *et al.* Efficient fiber-to-waveguide coupling by a lens on the end of the optical fiber fabricated by focused ion beam milling. *Microelectronic Engineering* **73,** 397–404. ISSN: 10959203 (6562 Sept. 2004).

230. Hutzler, N. R., Liu, L. R., Yu, Y. & Ni, K.-K. Eliminating light shifts for single atom trapping. *New Journal of Physics* **19,** 023007. ISSN: 10959203 (6562 Sept. 2017).

231. Hümmer, D., Schneeweiss, P., Rauschenbeutel, A. & Romero-Isart, O. Heating in nanophotonic traps for cold atoms. *Physical Review X* **9,** 041034. ISSN: 10959203 (6562 Sept. 2019).

232. Ocola, P. L. *et al.* Control and Entanglement of Individual Rydberg Atoms Near a Nanoscale Device. *arXiv:2210.12879v1* **373,** 1511–1514. ISSN: 10959203. `http://arxiv.org/abs/2210.12879` (6562 Oct. 2022).

233. Uphoff, M., Brekenfeld, M., Rempe, G. & Ritter, S. An integrated quantum repeater at telecom wavelength with single atoms in optical fiber cavities. *Applied Physics B* **122,** 1–15. ISSN: 10959203 (6562 Sept. 2016).

234. Radnaev, A. *et al.* A quantum memory with telecom-wavelength conversion. *Nature Physics* **6,** 894–899. ISSN: 10959203 (6562 Sept. 2010).

235. Willis, R., Becerra, F., Orozco, L. & Rolston, S. Photon statistics and polarization correlations at telecommunications wavelengths from a warm atomic ensemble. *Optics express* **19,** 14632–14641. ISSN: 10959203 (6562 Sept. 2011).

236. Legero, T., Wilk, T., Kuhn, A. & Rempe, G. Time-resolved two-photon quantum interference. *Applied Physics B* **77,** 797–802. ISSN: 10959203 (6562 Sept. 2003).

237. Lindner, N. H. & Rudolph, T. Proposal for pulsed on-demand sources of photonic cluster state strings. *Physical review letters* **103,** 113602. ISSN: 10959203 (6562 Sept. 2009).

238. Thomas, P., Ruscio, L., Morin, O. & Rempe, G. Efficient generation of entangled multiphoton graph states from a single atom. *Nature* **608,** 677–681. ISSN: 10959203 (6562 Sept. 2022).

239. Sørensen, A. S. & Mølmer, K. Measurement Induced Entanglement and Quantum Computation with Atoms in Optical Cavities. *Physical Review Letters* **91,** 097905. ISSN: 10959203 (9 Sept. 2003).

240. Duan, L.-M., Wang, B. & Kimble, H. J. Robust quantum gates on neutral atoms with cavity-assisted photon scattering. *Physical Review Applied* **72,** 032333. ISSN: 10959203 (3 Sept. 2005).

241. Borregaard, J., Kómár, P., Kessler, E. M., Sørensen, A. S. & Lukin, M. D. Heralded Quantum Gates with Integrated Error Detection in Optical Cavities. *Physical Review Letters* **114,** 110502. ISSN: 10959203 (11 Sept. 2015).

242. Bennett, C. H. *et al.* Purification of Noisy Entanglement and Faithful Teleportation via Noisy Channels. *Physical Review Letters* **76,** 722–725. ISSN: 10959203 (5 Sept. 1996).

243. Childress, L., Taylor, J. M., Sørensen, A. S. & Lukin, M. D. Fault-Tolerant Quantum Communication Based on Solid-State Photon Emitters. *Physical Review Letters* **96,** 070504. ISSN: 10959203 (7 Sept. 2006).

244. Borregaard, J., Kómár, P., Kessler, E. M., Lukin, M. D. & Sørensen, A. S. Long-distance entanglement distribution using individual atoms in optical cavities. *Physical Review Applied* **92,** 012307. ISSN: 10959203 (1 Sept. 2015).

245. Zhong, H.-S. *et al.* Quantum computational advantage using photons. *Science* **370,** 1460–1463. ISSN: 10959203 (6562 Sept. 2020).

246. Knill, E., Laflamme, R. & Milburn, G. J. A scheme for efficient quantum computation with linear optics. *nature* **409,** 46–52. ISSN: 10959203 (6562 Sept. 2001).

247. Lloyd, S. Enhanced sensitivity of photodetection via quantum illumination. *Science* **321,** 1463–1465. ISSN: 10959203 (6562 Sept. 2008).

248. Schwartz, O. *et al.* Superresolution microscopy with quantum emitters. *Nano letters* **13,** 5832–5836. ISSN: 10959203 (6562 Sept. 2013).

249. Vajner, D. A. *et al.* Single-Photon Advantage in Quantum Cryptography Beyond QKD. *arXiv preprint arXiv:2412.14993* **373,** 1511–1514. ISSN: 10959203 (6562 Sept. 2024).

250. Spillane, S., Kippenberg, T., Painter, O. & Vahala, K. Ideality in a fiber-taper-coupled microresonator system for application<? format?> to cavity quantum electrodynamics. *Physical review letters* **91,** 043902. ISSN: 10959203 (6562 Sept. 2003).

251. Barclay, P. E. *Fiber-coupled nanophotonic devices for nonlinear optics and cavity QED* 1511–1514 (California Institute of Technology, Sept. 2007).

252. Mosor, S *et al.* Scanning a photonic crystal slab nanocavity by condensation of xenon. *Applied Physics Letters* **87,** 1511–1514. ISSN: 10959203 (6562 Sept. 2005).

253. Sipahigil, A. *et al.* An integrated diamond nanophotonics platform for quantum-optical networks. *Science* **354,** 847–850. ISSN: 10959203 (6562 Sept. 2016).

254. Cooper, A. *et al.* Alkaline-Earth Atoms in Optical Tweezers. *Phys. Rev. X* **8,** 041055. ISSN: 10959203 (6562 Sept. 2018).

255. Norcia, M. A., Young, A. W. & Kaufman, A. M. Microscopic Control and Detection of Ultracold Strontium in Optical-Tweezer Arrays. *Phys. Rev. X* **8,** 041054. ISSN: 10959203 (6562 Sept. 2018).

256. Saskin, S., Wilson, J. T., Grinkemeyer, B. & Thompson, J. D. Narrow-Line Cooling and Imaging of Ytterbium Atoms in an Optical Tweezer Array. *Phys. Rev. Lett.* **122,** 143002. ISSN: 10959203 (6562 Sept. 2019).

257. Casabone, B. *et al.* Heralded Entanglement of Two Ions in an Optical Cavity. *Phys. Rev. Lett.* **111,** 100505. ISSN: 10959203 (6562 Sept. 2013).

258. Nguyen, C. H., Utama, A. N., Lewty, N. & Kurtsiefer, C. Operating a near-concentric cavity at the last stable resonance. *Phys. Rev. A* **98,** 063833. ISSN: 10959203 (6562 Sept. 2018).

259. Davis, E. J., Bentsen, G., Homeier, L., Li, T. & Schleier-Smith, M. H. Photon-Mediated Spin-Exchange Dynamics of Spin-1 Atoms. *Phys. Rev. Lett.* **122,** 010405. ISSN: 10959203 (6562 Sept. 2019).

260. Zeiher, J., Wolf, J., Isaacs, J. A., Kohler, J. & Stamper-Kurn, D. M. Tracking evaporative cooling of a mesoscopic atomic quantum gas in real time. *arXiv Prepr.* **2012.01280,** 1511–1514. ISSN: 10959203. eprint: 2012.01280 (6562 Sept. 2020).

261. Covey, J. P. *et al.* Telecom-Band Quantum Optics with Ytterbium Atoms and Silicon Nanophotonics. *Phys. Rev. Appl.* **11,** 034044. ISSN: 10959203 (6562 Sept. 2019).

262. Covey, J. P., Sipahigil, A. & Saffman, M. Microwave-to-optical conversion via four-wave mixing in a cold ytterbium ensemble. *Phys. Rev. A* **100,** 012307. ISSN: 10959203 (6562 Sept. 2019).

263. Norcia, M. A. *et al.* Seconds-scale coherence on an optical clock transition in a tweezer array. *Science* **366,** 93. ISSN: 10959203 (6562 Sept. 2019).

264. Madjarov, I. S. *et al.* An Atomic-Array Optical Clock with Single-Atom Readout. *Phys. Rev. X* **9,** 041052. ISSN: 10959203 (6562 Sept. 2019).

265. Madjarov, I. S. *et al.* High-fidelity entanglement and detection of alkaline-earth Rydberg atoms. *Nat. Phys.* **16,** 857. ISSN: 10959203 (6562 Sept. 2020).

266. Wilson, J. *et al.* Trapped arrays of alkaline earth Rydberg atoms in optical tweezers. *arXiv Prepr.* **1912.08754,** 1511–1514. ISSN: 10959203. eprint: 1912.08754 (6562 Sept. 2019).

267. Dür, W. & Briegel, H.-J. Entanglement Purification for Quantum Computation. *Phys. Rev. Lett.* **90,** 067901. ISSN: 10959203 (6562 Sept. 2003).

268. Bennett, C. H. *et al.* Purification of Noisy Entanglement and Faithful Teleportation via Noisy Channels. *Phys. Rev. Lett.* **76,** 722. ISSN: 10959203 (6562 Sept. 1996).

269. Polzik, E. S. & Ye, J. Entanglement and spin squeezing in a network of distant optical lattice clocks. *Phys. Rev. A* **93,** 021404. ISSN: 10959203 (6562 Sept. 2016).

270. Bernien, H. *et al.* Probing many-body dynamics on a 51-atom quantum simulator. *Nature* **551,** 579. ISSN: 10959203 (6562 Sept. 2017).

271. Choi, J. *et al.* Emergent Randomness and Benchmarking from Many-Body Quantum Chaos. *arXiv Prepr.* **2103.03535,** 1511–1514. ISSN: 10959203. eprint: 2103.03535 (6562 Sept. 2021).

272. Graham, T. M. *et al.* Rydberg-Mediated Entanglement in a Two-Dimensional Neutral Atom Qubit Array. *Phys. Rev. Lett.* **123,** 230501. ISSN: 10959203 (6562 Sept. 2019).

273. Teller, M. *et al.* Heating of a Trapped Ion Induced by Dielectric Materials. *Phys. Rev. Lett.* **126,** 230505. ISSN: 10959203 (6562 Sept. 2021).

274. Kawasaki, A. *et al.* Geometrically asymmetric optical cavity for strong atom-photon coupling. *Phys. Rev. A* **99,** 013437. ISSN: 10959203 (6562 Sept. 2019).

275. Ye, J., Kimble, H. J. & Katori, H. Quantum State Engineering and Precision Metrology Using State-Insensitive Light Traps. *Science* **320,** 1734. ISSN: 10959203 (6562 Sept. 2008).

276. Moses, S. A. *et al.* Creation of a low-entropy quantum gas of polar molecules in an optical lattice. *Science* **350,** 659. ISSN: 10959203 (6562 Sept. 2015).

277. Covey, J. P. *et al.* Doublon dynamics and polar molecule production in an optical lattice. *Nat. Commun.* **7,** 11279. ISSN: 10959203 (6562 Sept. 2016).

278. Gorshkov, A. V. *et al.* Alkaline-Earth-Metal Atoms as Few-Qubit Quantum Registers. *Phys. Rev. Lett.* **102,** 110503. ISSN: 10959203 (6562 Sept. 2009).

279. Young, A. W. *et al.* Half-minute-scale atomic coherence and high relative stability in a tweezer clock. *Nature* **588,** 408. ISSN: 10959203 (6562 Sept. 2020).

280. Pirandola, S., Laurenza, R., Ottaviani, C. & Banchi, L. Fundamental limits of repeaterless quantum communications. *Nat. Commun.* **8,** 15043. ISSN: 10959203 (6562 Sept. 2017).

281. Beugnon, J. *et al.* Two-dimensional transport and transfer of a single atomic qubit in optical tweezers. *Nat. Phys.* **3,** 696. ISSN: 10959203 (6562 Sept. 2007).

282. Lengwenus, A., Kruse, J., Schlosser, M., Tichelmann, S. & Birkl, G. Coherent Transport of Atomic Quantum States in a Scalable Shift Register. *Phys. Rev. Lett.* **105,** 170502. ISSN: 10959203 (6562 Sept. 2010).

283. Schymik, K.-N. *et al.* Enhanced atom-by-atom assembly of arbitrary tweezer arrays. *Phys. Rev. A* **102,** 063107. ISSN: 10959203 (6562 Sept. 2020).

284. McKeever, J., Boca, A., Boozer, A. D., Buck, J. R. & Kimble, H. J. Experimental realization of a one-atom laser in the regime of strong coupling. *Nature* **425,** 268. ISSN: 10959203 (6562 Sept. 2003).

285. Birnbaum, K. M. *et al.* Photon blockade in an optical cavity with one trapped atom. *Nature* **436,** 87. ISSN: 10959203 (6562 Sept. 2005).

286. Reiserer, A. & Rempe, G. Cavity-based quantum networks with single atoms and optical photons. *Rev. Mod. Phys.* **87,** 1379. ISSN: 10959203 (6562 Sept. 2015).

287. Browaeys, A. & Lahaye, T. Many-body physics with individually controlled Rydberg atoms. *Nat. Phys.* **16,** 132. ISSN: 10959203 (6562 Sept. 2020).

288. Ebadi, S. *et al.* Quantum phases of matter on a 256-atom programmable quantum simulator. *Nature* **595,** 227–232. ISSN: 10959203 (6562 Sept. 2021).

289. Saffman, M., Walker, T. G. & Mølmer, K. Quantum information with Rydberg atoms. *Reviews of modern physics* **82,** 2313–2363. ISSN: 10959203 (6562 Sept. 2010).

290. Boca, A. *et al.* Observation of the Vacuum Rabi Spectrum for One Trapped Atom. *Phys. Rev. Lett.* **93,** 233603. ISSN: 10959203 (6562 Sept. 2004).

291. Kalb, N., Reiserer, A., Ritter, S. & Rempe, G. Heralded Storage of a Photonic Quantum Bit in a Single Atom. *Phys. Rev. Lett.* **114,** 220501. ISSN: 10959203 (6562 Sept. 2015).

292. Pezzè, L., Smerzi, A., Oberthaler, M. K., Schmied, R. & Treutlein, P. Quantum metrology with nonclassical states of atomic ensembles. *Rev. Mod. Phys.* **90,** 035005. ISSN: 10959203 (6562 Sept. 2018).

293. Pedrozo-Peñafiel, E. *et al.* Entanglement on an optical atomic-clock transition. *Nature* **588,** 414. ISSN: 10959203 (6562 Sept. 2020).

294. Zhang, Y., McCutcheon, M. W., Burgess, I. B. & Loncar, M. Ultra-high-Q TE/TM dual-polarized photonic crystal nanocavities. *Opt. Lett.* **34,** 2694–2696. ISSN: 10959203. https://opg.optica.org/ol/abstract.cfm?URI=ol-34-17-2694 (6562 Sept. 2009).

295. Vučković, J., Rivoire, K. & Buckley, S. Multiply resonant photonic crystal nanocavities for nonlinear frequency conversion. *Optics Express, Vol. 19, Issue 22, pp. 22198-22207* **19,** 22198–22207. ISSN: 1094-4087. https://www.osapublishing.org/viewmedia.cfm?uri=oe-19-22-22198&seq=0&html=truehttps://www.osapublishing.org/abs

tract.cfm?uri=oe-19-22-22198https://www.osapublishing.org/oe/abstract.cfm?uri=oe-19-22-22198 (22 Oct. 2011).

296. Menon, S. G., Glachman, N., Pompili, M., Dibos, A. & Bernien, H. An integrated atom array-nanophotonic chip platform with background-free imaging. *arXiv:2311.02153* **373,** 1511–1514. ISSN: 10959203. https://arxiv.org/abs/2311.02153 (6562 Sept. 2023).

297. McCutcheon, M. W. & Lončar, M. Design of a silicon nitride photonic crystal nanocavity with a Quality factor of one million for coupling to a diamond nanocrystal. *Optics express* **16,** 19136–19145. ISSN: 10959203 (6562 Sept. 2008).

298. Ye, Z., Fülöp, A., Helgason, Ó. B., Andrekson, P. A. & Torres-Company, V. Low-loss high-Q silicon-rich silicon nitride microresonators for Kerr nonlinear optics. *Optics letters* **44,** 3326–3329. ISSN: 10959203 (6562 Sept. 2019).

299. Debnath, K. *et al.* Ultrahigh-Q photonic crystal cavities in silicon rich nitride. *Optics Express* **25,** 27334–27340. ISSN: 10959203 (6562 Sept. 2017).

300. Lvovsky, A. I., Sanders, B. C. & Tittel, W. Optical quantum memory. *Nature Photonics* **3,** 706–714. ISSN: 1749-4893. https://doi.org/10.1038/nphoton.2009.231 (6562 Sept. 2009).

301. Jing, B. & Bao, X.-H. Ensemble-Based Quantum Memory: Principle, Advance, and Application. *Photonic Quantum Technologies: Science and Applications* **2,** 433–462. ISSN: 10959203 (6562 Sept. 2023).

302. Ma, L., Slattery, O. & Tang, X. Optical quantum memory based on electromagnetically induced transparency. *Journal of Optics* **19,** 043001. ISSN: 10959203 (6562 Sept. 2017).

303. Bussières, F. *et al.* Prospective applications of optical quantum memories. *Journal of Modern Optics* **60,** 1519–1537. ISSN: 10959203. https://doi.org/10.1080/09500340.2013.856482 (6562 Sept. 2013).

304. Afzelius, M., Simon, C., de Riedmatten, H. & Gisin, N. Multimode quantum memory based on atomic frequency combs. *Phys. Rev. A* **79,** 052329. ISSN: 10959203. https://link.aps.org/doi/10.1103/PhysRevA.79.052329 (5 Sept. 2009).

305. Jobez, P. *et al.* Towards highly multimode optical quantum memory for quantum repeaters. *Phys. Rev. A* **93,** 032327. ISSN: 10959203. https://link.aps.org/doi/10.1103/PhysRevA.93.032327 (3 Sept. 2016).

306. Bashkansky, M., Fatemi, F. K. & Vurgaftman, I. Quantum memory in warm rubidium vapor with buffer gas. *Optics Letters* **37,** 142–144. ISSN: 10959203 (6562 Sept. 2012).

307. Vernaz-Gris, P., Huang, K., Cao, M., Sheremet, A. S. & Laurat, J. Highly-efficient quantum memory for polarization qubits in a spatially-multiplexed cold atomic ensemble. *Nature communications* **9,** 1–6. ISSN: 10959203 (6562 Sept. 2018).

308. Cho, Y.-W. *et al.* Highly efficient optical quantum memory with long coherence time in cold atoms. *Optica* **3,** 100–107. ISSN: 10959203 (6562 Sept. 2016).

309. Hosseini, M., Sparkes, B. M., Campbell, G., Lam, P. K. & Buchler, B. C. High efficiency coherent optical memory with warm rubidium vapour. *Nature communications* **2,** 1–5. ISSN: 10959203 (6562 Sept. 2011).

310. Guo, J. *et al.* High-performance Raman quantum memory with optimal control in room temperature atoms. *Nature communications* **10,** 1–6. ISSN: 10959203 (6562 Sept. 2019).

311. Tittel, W. *et al.* Photon-echo quantum memory in solid state systems. *Laser & Photonics Reviews* **4,** 244–267. ISSN: 10959203 (6562 Sept. 2010).

312. Thiel, C., Böttger, T. & Cone, R. Rare-earth-doped materials for applications in quantum information storage and signal processing. *Journal of luminescence* **131,** 353–361. ISSN: 10959203 (6562 Sept. 2011).

313. Zhong, T. & Goldner, P. Emerging rare-earth doped material platforms for quantum nanophotonics. *Nanophotonics* **8,** 2003–2015. ISSN: 10959203 (6562 Sept. 2019).

314. Liu, G. & Jacquier, B. *Spectroscopic properties of rare earths in optical materials* 1511–1514 (Springer Science & Business Media, Sept. 2006).

315. Knaut, C. M. *et al. Entanglement of Nanophotonic Quantum Memory Nodes in a Telecommunication Network* Sept. 2023. arXiv: 2310.01316 [quant-ph].

316. Huber, D., Reindl, M., Aberl, J., Rastelli, A. & Trotta, R. Semiconductor quantum dots as an ideal source of polarization-entangled photon pairs on-demand: a review. *Journal of Optics* **20,** 073002. ISSN: 10959203. https://dx.doi.org/10.1088/2040-8986/aac4c4 (6562 Sept. 2018).

317. Heller, L., Lowinski, J., Theophilo, K., Padrón-Brito, A. & de Riedmatten, H. Raman Storage of Quasideterministic Single Photons Generated by Rydberg Collective Excitations in a Low-Noise Quantum Memory. *Phys. Rev. Appl.* **18,** 024036. ISSN:

10959203. https://link.aps.org/doi/10.1103/PhysRevApplied.18.024036 (2 Sept. 2022).

318. Guo, M. *et al.* Rare-earth quantum memories: The experimental status quo. *Frontiers of Physics* **18,** 21303. ISSN: 10959203 (6562 Sept. 2023).

319. Tanzilli, S. *et al.* A photonic quantum information interface. *Nature* **437,** 116. ISSN: 10959203. https://pubmed.ncbi.nlm.nih.gov/16136138/ (6562 Sept. 2005).

320. Tchebotareva, A. *et al.* Entanglement between a Diamond Spin Qubit and a Photonic Time-Bin Qubit at Telecom Wavelength. *Phys. Rev. Lett.* **123,** 063601. ISSN: 10959203. https://link.aps.org/doi/10.1103/PhysRevLett.123.063601 (6 Sept. 2019).

321. Iuliano, M. *et al. Interfacing an NV-center in diamond and a rare-earth ion compatible photonic time-bin qubit* in *Optica Quantum 2.0 Conference and Exhibition* **373** (Optica Publishing Group, Sept. 2023), QW4A.7. https://opg.optica.org/abstract.cfm?URI=QUANTUM-2023-QW4A.7.

322. Jiang, N. *et al.* Experimental realization of 105-qubit random access quantum memory. *npj Quantum Information* **5,** 28. ISSN: 10959203. https://doi.org/10.1038/s41534-019-0144-0 (6562 Sept. 2019).

323. Douglas, J. S. *et al.* Quantum many-body models with cold atoms coupled to photonic crystals. *Nature Photonics* **9,** 326–331. ISSN: 17494893 (5 Sept. 2015).

324. Bello, M., Platero, G., Cirac, J. I. & González-Tudela, A. Unconventional quantum optics in topological waveguide QED. *Science Advances* **5,** 1511–1514. ISSN: 23752548. https://www.science.org/doi/10.1126/sciadv.aaw0297 (7 July 2019).

325. Mahmoodian, S., Calajó, G., Chang, D. E., Hammerer, K. & Sørensen, A. S. Dynamics of Many-Body Photon Bound States in Chiral Waveguide QED. *Physical Review X* **10,** 031011. ISSN: 21603308. https://journals.aps.org/prx/abstract/10.1103/PhysRevX.10.031011 (3 Sept. 2020).

326. Chang, D. E., Cirac, J. I. & Kimble, H. J. Self-organization of atoms along a nanophotonic waveguide. *Physical Review Letters* **110,** 113606. ISSN: 00319007. https://journals.aps.org/prl/abstract/10.1103/PhysRevLett.110.113606 (11 Mar. 2013).

327. Fayard, N., Henriet, L., Asenjo-Garcia, A. & Chang, D. Many-body localization in waveguide QED. *Physical Review Research* **3,** 033233. ISSN: 10959203. http://arxiv.org/abs/2101.01645http://dx.doi.org/10.1103/PhysRevResearch.3.033233 (6562 Jan. 2021).

328. Yu, S.-P., Muniz, J. A., Hung, C.-L. & Kimble, H. Two-dimensional photonic crystals for engineering atom–light interactions. *Proceedings of the National Academy of Sciences* **116,** 12743–12751. ISSN: 10959203 (6562 Sept. 2019).

329. Komza, L. *et al.* Multiplexed color centers in a silicon photonic cavity array. *arXiv preprint arXiv:2501.17339* **373,** 1511–1514. ISSN: 10959203 (6562 Sept. 2025).